Electronic and vibrational properties of carbon and CdSe nanostructures

vorgelegt von
Diplom-Physiker
Marcel Mohr
aus Mosbach/Baden

Von der Fakultät II - Mathematik und Naturwissenschaften
der Technischen Universität Berlin
zur Erlangung des akademischen Grades

Doktor der Naturwissenschaften
– Dr. rer.nat. –

genehmigte Dissertation

Promotionsausschuss:

Vorsitzender:	Prof. Dr. Michael Lehmann
Berichter:	Prof. Dr. Christian Thomsen
	Prof. Dr. Milan Damnjanović

Tag der wissenschaftlichen Aussprache: 23. Juli 2010

Berlin 2010
D 83

Zusammenfassung – German abstract

Mit *ab-initio* (lat: von Anfang an) oder *first-principles* werden Berechnungen bezeichet, die ohne empirische Parameter durchgeführt wurden. In dieser Arbeit untersuche ich mit *ab-initio* Methoden die Phononen und die elektronischen Eigenschaften von Nanostrukturen. Als untersuchte Nanostrukturen wurden zwei Arten ausgewählt, aus einer Atomsorte bestehende und aus einem binärem Halbleitermaterial aufgebaute Strukturen: Kohlenstoff- und CdSe basierte Strukturen. Kohlenstoff-basierenden Nanostrukturen existieren in einer Vielzahl an Formen. Hier fokussiere ich mich auf eine monoatomaren Lage Graphit, dem sogenannten Graphen, Kohlenstoffnanorröhren und Graphennanostreifen. Diese stehen modellhaft für ein- und zweidimensionale Systeme. CdSe-Nanostrukturen sind ebenfalls niederdimensionale Systeme und lassen sich in großen Mengen mit wohldefinierten Abmessungen erzeugen. Dies macht sie direkt für Anwendungen interesssant. Hierbei wurden hauptsächlich das vielversprechende System der CdSe Nanodrähte untersucht

Die Rechnungen wurden durch den Einsatz von Symmetrien optimiert und die Ressourcen konnten besser genutzt werden. Bei der Auswertung der Ergebnisse vereinfachten die Symmetrien die Analyse, z. B., bei der Klassifizierung in entartete und nicht-entartete Eigenzustände der Systeme. Begleitet wurden die Rechnungen durch inelastische Streuung mit sichtbarem Licht (der sog. Ramanstreuung) und mit Röntgenlicht (IXS, engl.: inelastic x-ray scattering), die eine Bestimmung der Frequenzen der Phononen erlauben.

Innerhalb der Arbeit wurde eine vollständige Messung der Phononendispersion entlang der Hochsymmetrierichtungen von Graphit durchgeführt. Die Ergebnisse der Messung wurden in ein 15-parametriges Kraftkonstantenmodell übertragen, das Wechselwirkungen bis zum 5. Nachbarn berücksichtigt, und eine gute Beschreibung der Dispersion erlaubt.

Spezielle Verspannungen in Graphen können eine Bandlücke erzeugen. Die Frage, ob dies mit uniaxialer Verspannung ebenso möglich ist, konnte verneint werden. Der Übergangspunkt von Valenz- und Leitungsband entfernt sich von den Hochsymmetriepunkten. Diese Beobachtung wurde erst durch genaue Betrachtung der Bandstruktur in der ganzen zweidimensionalen Brillouinzone ermöglicht.

Vorhersagen zur Verschiebung der Ramanmoden in verspanntem Graphen führten zu Diskrepanzen mit vorhandenen experimentellen Daten. Eine Erweiterung des Doppelresonanzmodells löste diese auf und konnte die beobachteten Ergebnisse erklären. Dies trug zum Verständnis der Entstehung der D- und $2D$-mode bei, die in allen sp^2 hybridisierten Kohlenstoffstrukturen

vorkommt.

Es wurde eine radiale Atmungsmode [engl: radial-breathing-mode (RBM)] in kristallinen Nanodrähten vorhergesagt, die eine Bestimmung des Durchmessers mittels spektroskopischer Methoden erlaubt. Aufgrund dieser Vorhersage konnte die RBM erstmals in Ramanexperimenten an CdSe Nanostäbchen nachgewiesen werden.

Der Einfluß einer ZnS-Hülle auf den CdSe-Kern von Nanodrähten wurde untersucht. Es wurde eine Abnahme der Bindungslängen im CdSe-Kern gefunden. Die Verspannungen, die durch die ZnS-Hülle erzeugt werden, führen zu einer Erhöhung der RBM-Frequenz. Dies wird bei einer doppellagigen Hülle verstärkt und ebenfalls im Experiment bestätigt.

Die gewachsene ZnS-Hülle erhöht die Quantenausbeute bei Photolumineszensmessungen um eine Größenordnung [1]. Dies wurde zuerst einer Verbesserung der kristallinen Struktur zugeschrieben. Eine räumliche Trennung der Loch- und Elektronenwellenfunktion in Kern und Hülle kann diese Erhöhung auch leicht erklären. Die viel größere Bandlücke von kristallinem ZnS gegenüber kristallinem CdSe machte diese Interpretation eher unwahrscheinlich. In meinen atomistischen Rechnungen von kleinen CdSe/ZnS Kern/Hülle Nanodrähten ist das Auftreten eines Typ-II Heteroübergangs jedoch klar zu sehen. Dieses Typ-II Verhalten wurde später auch für die sehr ähnlichen CdSe/ZnS Kern/Hülle Nanokristalle experimentell beobachtet [2].

Abstract

Ab-initio (lat: from the beginning) or first-principles denote a calculation that is performed without empirical parameters. In this work I apply *ab-initio* methods to investigate the electronic and vibrational properties of nanostructures. Two types of nanostructures were chosen, elementary structures and binary compounds: carbon and CdSe-based systems. Carbon-based structures exist in a variety of different forms. I focus on a single-atomic layer of graphite, the so-called graphene, carbon nanotubes and graphene nanoribbons. These systems exemplary represent one- and two-dimensional systems. CdSe-based nanostructres are low-dimensional structures as well, and can be synthesized in large scales with well defined dimensions. This makes them directly interesting for applications. Among them I focus on the promising CdSe-nanowires.

The calculations were optimized through the use of symmetries, where the available resources could be used more efficiently. Analysis of the results was simplified by symmetries as well, for example, the classification into he degenerated or non-degenerated eigenstates of the systen. The calculations were accompanied by inelastic scattering with visible light (Raman scattering) and X-rays (IXS, inelastic X-ray scattering), which allows a determination of phonon frequencies.

During the thesis a complete measurement of the phonon dispersion of graphite was performed along the high-symmetry directions. The results were fitted with a 15-parameter force-constant model, which involves interaction up to the fifth-nearest neighbor, and allows a good description of the dispersion.

Nonuniform strain can induce a band gap in graphene. The question, if this also applies to niaxial strain could be resolved. The crossing point of valence and conduction band moves away from the points of high-symmetry. This observation was only achieved by a detailed investigation of the electronic band structure in two dimensions.

Predictions of the strain-induced Raman shift in graphene lead to discrepancies with experimental data. An extension of the double-resonant model solved them and is able to explain the observed results. This gave insight into the origin of the D- and $2D$-mode, which is present in all sp^2-hybridized carbon nanostructures.

In crystalline nanowires we predicted a radial-breathing mode (RBM), which allows for a determination of the nanowire diameter with spectroscopic methods. The calculations lead to the first experimental observation of the RBM.

The effect of a ZnS shell on the CdSe core of nanowires was investigated. A decrease of the bond length of the CdSe core was found. The strain from the ZnS-shell leads to an increase in

RBM-frequency. This is enhanced by a double-layer shell and was verified experimentally.

The grown ZnS-shell around CdSe-rods improves the quantum yield in photoluminescence experiments by an order of magnitude [1]. This was believed to be due to an increase in crystalline quality. However a separation of the wavefunction of the hole and the electron into the core and the shell can explain this higher quantum yield very naturally. The much larger bandgap of bulk ZnS compared to that of CdSe made such considerations at first very unlikely. In my atomistic calculations of CdSe/ZnS core shell nanowires this transition into a type-II heterojunction is clearly visible. This type-II heterojunction behaviour was then observed experimentally for the very similar CdSe/ZnS core/shell nanocrystals [2].

List of publications

Parts of the thesis have already been published:

1. M. Mohr, M. Machón, J. Maultzsch, and C. Thomsen
   Double-resonant Raman processes in germanium : Group theory and *ab initio* calculations
   Phys. Rev. B **73**, 035 217 (2006)

2. M. Mohr, M. Machón, C. Thomsen, I. Milošević, and M. Damnjanović
   Mixing of the fully symmetric vibrational modes in carbon nanotubes
   Phys. Rev. B **75**, 195 401 (2007)

3. M. Mohr, J. Maultzsch, E. Dobardžić, S. Reich, I. Milošević, M. Damnjanović, A. Bosak, M. Krisch,and C. Thomsen
   Phonon dispersion of graphite by inelastic x-ray scattering: Determination of the mid-frequency range between K and M
   Phys. Rev. B **76**, 035 439 (2007)

4. M. Mohr, M. Machón, C. Thomsen, Milošević, and M. Damnjanović,
   Detail study of the Raman-active modes in carbon nanotubes,
   phys. stat. sol. (b) **244**, 4275 (2007)

5. A. Bosak, M. Krisch, M. Mohr, J. Maultzsch, and C. Thomsen
   Elasticity of single-crystalline graphite : Inelastic x-ray scattering study
   Phys. Rev. B **75**, 153 408 (2007)

6. H. Lange, M. Mohr, M. Artemyev, U. Woggon, and C. Thomsen
   Direct Observation of the Radial Breathing Mode in CdSe Nanorods
   Nano Lett. **8**, 4614 (2008)

7. M. Mohr and C. Thomsen
   Effects of a ZnS-shell on the structural and electronic properties of CdSe-nanorods
   physica status solidi (b) **245**, 2111 (2008)

8. R. Gillen, M. Mohr, J. Maultzsch, and C. Thomsen
   Lattice vibrations in graphene nanoribbons from density functional theory
   phys. stat. sol. (b) **246**, 2577 (2009)

9. M. Mohr and C. Thomsen
   Phonons in bulk CdSe and CdSe nanowires
   Nanotechnology **20**, 115 707 (2009)

10. I. Milošević, N. Kepčija, E. Dobardžić, M. Mohr, J. Maultzsch, C. Thomsen, and M. Damnjanoviić
    Symmetry-based analysis of the electron-phonon interaction in graphene
    phys. stat. sol. (b) **246**, 2606 (2009)

11. R. Gillen, M. Mohr, C. Thomsen, and J. Maultzsch
    Vibrational properties of graphene nanoribbons by first-principles calculations
    Phys. Rev. B **80**, 155 418 (2009)

12. M. Mohr, K. Papagelis, J. Maultzsch, and C. Thomsen
    Two-dimensional electronic and vibrational band structure of uniaxially strained graphene from ab initio calculations
    Phys. Rev. B **80**, 205 410 (2009)

13. I. Milošević, N. Kepčija, E. Dobardžić, M. Damnjanović, M. Mohr, J. Maultzsch, and C. Thomsen,
    Electron-phonon coupling in graphene, Int. J. Mod Phys B **24**, 655 (2010)

14. R. Gillen, M. Mohr, and J. Maultzsch,
    Symmetry properties of vibrational modes in graphene nanoribbons, Phys. Rev. B **81**, 205 426 (2010)

Accepted for publication

15. H. Lange, M. Mohr, M. Artemyev, U. Woggon, T. Niermann, and C. Thomsen,
    Optical phonons in colloidal CdSe nanorods,
    phys. stat. sol. (a), **DOI**: 10.1002/pssa.201026122 (2010)

16. I. Milošević, N. Kepčija, E. Dobardžić, M. Mohr, J. Maultzsch, C. Thomsen, and M. Damnjanović,
    Symmetry based analysis of the Kohn anomaly and electron-phonon interaction in graphene and carbon nanotubes
    in print, Phys. Rev. B, (2010).

Manuscripts under review

17. M. Mohr, J. Maultzsch, and C. Thomsen,
    Splitting of the Raman 2D band of graphene subjected to strain,
    subm. to Nano Lett. (2010)

18. R. Gillen, M. Mohr, and J. Maultzsch,
    Raman-active modes in graphene nanoribbons,
    subm. to phys. stat. sol. (b) (2010)

Contents

1. Introduction

Crystalline nanostructures are structures with at least one dimension in the nanometer range. The chemical and physical properties of nanomaterial can be considerably different from those of the atomic or solid material. From a physical point of view nanostructures are bridging the gap between isolated atoms and bulk solids. What differs the isolated atom from the solid is the rise of interatomic interaction, the overlap of the electron's wavefunctions. The wavefunctions in the nanostructure are spatially confined by the crystalline boundaries. If the size of the structure becomes similar to the de Broglie wavelength of the electron, one speaks of quantum confinement. One effect of this quantum confinement is the increase of the spacing between the energy levels of the electrons. Quantum confinement can lead to fundamentally new phenomena that depend on size and shape of the nanostructured material. One possibility to exploit this is to tailor the electronic band gap.

Confinement effects also influences the lattice vibrations. The reduction in size gives rise to boundary conditions. These boundary conditions can be defined by the edges, *e.g.* , in flat nanoribbons. In nanotubes, hollow cylinders of atom-thick layers, the boundary conditions are periodic along the circumference.

In bulk materials the ratio between atoms at the surface and atoms in the volume goes to zero. If the size dimensions are reduced, this ratio increases. For structures in the range of 1 nm the numbers of surface to volume atoms are more or less equal. Changing the environment of the surface may change the properties of the structure completely. This can be achieved by growing a shell of a different material around the nanostructure. The under-coordination of the surface atoms considerably influences the properties of the structure. Changes are also induced by the geometry. Surface atoms have less atomic neighbours than their bulk counterparts. The lowest-energetic geometric configuration in the bulk usually differs from that of the surface which results in a reconstruction of the surface atoms.

Nanostructures exist in various types and forms: molecular cluster, quantum dots, nanowires, nanorods, nanoribbons, nanotubes, and collections of nanostructures, arrays or superlattices. In this work I focus on two types of nanostructures: one type involves the different forms of an elemental (carbon) nanostructures, the other nanowires of a compound semiconductor (CdSe).

The allotropic forms of carbon exist in sp^2 (Graphite, carbon nanotubes), sp^3 (Diamond) or a mixture of both (Graphane, a hydrogen-covered layer of graphene). Carbon is an abundant ressource on earth and not poisonous in living organism. Besides carbon materials have ex-

traordinary properties. The strong covalent binding leads to a large hardness. Diamond is the hardest bulk material known. Its thermal conductivity is also highest known for any bulk material. The wide band gap of diamond is reduced to zero going from the tetrahedral sp^3-lattice to the sp^2-structure of graphene. Graphene is a flat monolayer of carbon atoms packed into a two-dimensional honeycomb lattice. Theoretically it is considered as building block for graphitic materials of all dimensionalities. It can be wrapped up into 0D fullerenes, rolled into 1D nanotubes or stacked into 3D graphite. A small strip of graphene, with a large aspect ratio, is called a graphene nanoribbon. Whereas graphene is semimetallic, carbon nanotubes and graphene nanoribbons can exhibit a band-gap. Its magnitude not only depends on the size, but also on the exact geometry of the structure. Still today it is not possible to grow these nanostructures well defined, *e.g.* , only semiconducting nanotubes of a specific diameter and well-defined band gap.

A different approach is the growth of inorganic colloidal nanostructures from particles of a few hundred atoms up to μm sized structures. They are synthesized in solution, which makes it possible to produce them cheaply in large amounts. Nanostructures from binary compounds with a bulk wurtzite structure usually grow along the c-axis. Exploiting the growth kinetic along the c-axis allows the synthesis of nanorods with well defined diameters and aspect ratios. One of the first material used for such structures was the direct semiconductor CdSe. Nanorods from this material still possess a direct band-gap that covers the visible spectrum of light, depending on the rod's diameter.

The small sizes of these nanostructures make an investigation difficult. Many properties of these structures are still unknown. The sizes of the nanocrystals requires specialized experimental techniques for a characterization. In this work *ab-initio* calculations, accompanied by Raman spectroscopy, are applied to characterize the structural, electronic, and vibrational properties of these nanostructures. Making use of symmetries usually simplifies the solution of a physical problem or at first allows for a solution. For atoms and molecules point group symmetries can be applied. For infinite three-dimensional crystals space groups can be used . Space group symmetry operations combine point group symmetries with translational symmetries. The only allowed rotations in space groups are rotations around $2\pi/n$, where $n = 2, 3, 4, 6$. In contrast, in one-dimensional nanostructures arbitrary rotations are allowed, as they lack the translational symmetry in those two dimensions, perpendicular to their axis. For them the so-called line groups can be used that combine point group symmetries with translations along one axis. Inelastic scattering with X-rays from a synchrotron source is used to complete the phonon dispersion of graphite, and to clarify issues regarding shape and ordering of the branches. The changes in the band structure of uniaxially strained graphene are investigated. No gap is opened, but the position of the valence band minimum is moving. Strain reduces the symmetry of graphene and gave insight into the origin of the double-resonant Raman $2D$-mode. Nanoribbons can be classified into families, each of which shows different Raman modes. The size-dependence

of phonons in CdSe nanowires is investigated. A strongly size-dependent Raman-active mode in CdSe nanowires, the radial breathing mode (RBM), is predicted and its existence verified. In core-shell structures the shell introduces strain in the core-region. The amount of strain is estimated from *ab-initio* calculations. The shell leads to a higher quantum-yield in photoluminescence experiments. The reason lies in type-II heterojunction, whereas in bulk it would be one of type-I.

2. Methods

2.1. Density functional theory

The fundamental idea of density functional theory is that the properties of a system of many interacting particles can be viewed as a functional of their ground state density $n_0(\mathbf{r})$. This density $n_0(\mathbf{r})$ is a scalar function that , in principle, determines all information of the many-body wavefunctions for the ground state and all excited states. This theory was established in the years 1964 and 1965 by Hohenberg, Kohn and Sham [3, 4].*

2.1.1. Schrödinger equation

The theory of electronic structure in solid-state physics is based on the non-relativistic many-particle Schrödinger equation for the many electron wavefunction Ψ

$$\left[\frac{\hbar^2}{2m}\sum_i \nabla_i^2 - \sum_i V_{\text{ext}}(r_i) + \frac{1}{2}\sum_{i\neq i'}\frac{e^2}{|r_i - r_{i'}|}\right]\Psi = E\Psi, \tag{2.1}$$

where r_i, m, e are the position, mass and charge of the i-th electron and $\hbar$ the Planck constant. If the external potential is caused only by the atomic cores it becomes

$$V_{\text{ext}}(r_i) = V_{\text{ion}}(r_i) = \sum_j \frac{Z_j e^2}{|r_i - R_j|}, \tag{2.2}$$

where R_j and Z_j are the position and atomic number of the j-th atom. Inherent in equation (2.2) is the Born-Oppenheimer approximation: the Hamiltonian does not depend on the velocity of the nuclei, in other words the positions of the nuclei are fixed.

2.1.2. Basic principles of density functional theory

The formulation of the density functional theory applies to any system, which can be described by the Hamiltonian above. The basic concepts are expressed in the Hohenberg-Kohn (HK) theorems [3]:

*Walter Kohn was rewarded the Nobel prize in chemistry in 1998 for this work.

- **Theorem I: The density as basic variable** For any system of interacting particles in an external potential $V_{\text{ext}}(\mathbf{r})$ the potential $V_{\text{ext}}(\mathbf{r})$ is determined uniquely (apart from a trivial additive constant) by the ground state density $n_0(\mathbf{r})$.

- **Theorem II: The variation principle** For any particular external potential $V_{\text{ext}}(\mathbf{r})$ a unique energy functional $E[n]$ can be defined that has a minimum at the correct ground state density $n_0(\mathbf{r})$.

Although it is in principle sufficient to know the density, there is no easy way to extract physical information from this knowledge. For example, the kinetic energy cannot be extracted directly from the density, one has to revert the density into a set of N wavefunctions, where N is number of electrons. This leads to the Kohn-Sham approach where the kinetic energy is expressed *via* the one-particle Green's function $G(\mathbf{r}, \mathbf{r}', E)$. The idea behind the Kohn-Sham approach is to replace the ground state density of a system of interacting particles with that of an auxiliary system of non-interacting particles. The Kohn-Sham equations are [4, 5]

$$\left[\frac{\hbar^2}{2m}\nabla^2 + V_{\text{ion}}(\mathbf{r}) + V_H(\mathbf{r}) + V_{\text{xc}}(\mathbf{r})\right]\Psi_i = \epsilon_i \Psi_i \tag{2.3}$$

where Ψ_i is the electron wavefunction of electron i, ϵ_i the Kohn-Sham eigenvalue, V_H the Hartree potential. V_{xc} is an exchange-correlation potential defined by a functional derivative

$$V_{\text{xc}}(r) = \frac{\delta E_{\text{xc}}[n(r)]}{\delta n(r)} \tag{2.4}$$

Up to now there is no exact definition of $V_{\text{xc}}(r)$, only approximations. The most widely used are the local-density approximation (LDA) and the generalized-gradient approximation (GGA):

- The LDA is constructed by assuming the exchange-correlation energy per electron at point $\mathbf{r}$ in the electron gas, $\epsilon_{\text{xc}}(\mathbf{r})$, is the same as that of a homogeneous electron gas with the electron density at point $\mathbf{r}$. Thus

$$E_{\text{xc}}[n(r)] = \int \epsilon_{\text{xc}}(r) n(r) dV. \tag{2.5}$$

  There exist different explicit parameterizations, *e.g.* , see Ref. [4] or Ref. [6]. In this approximation the exchange and the correlation have a very local character.

- A slightly more sophisticated ansatz is the GGA. They are local too, but also take into account the gradient of the density at the position $\mathbf{r}$

$$E_{\text{xc}}[n(r)] = \int f[n(r), \nabla n(r)] dV. \tag{2.6}$$

There are different parameterizations for defining $f[n(r), \nabla n(r)]$. Widely implemented in current computer codes are the ones by Perdew and Wang (PW) [7] or Perdew, Burke and Ernzerhof (PBE) [8].

Due to the inclusion of the gradient, the GGA can better deal with inhomogeneities in electronic systems. In contrast to the LDA, which shows an overbinding, atomic bonds are expanded and softened in the GGA.

For more localized or strongly interacting electrons there are a number of improved functionals: LDA+U adds an orbital-dependent interaction and shows good results especially for transition metals. Hybrid functionals, which are a combination of Hartree-Fock and density functionals, are very accurate functionals regarding energies and very popular among chemists. One of them, the prominent B3LYP functional, is a three parameter functional with coefficients empirically adjusted to fit atomic and molecular data. In contrast to that, the LDA and GGA have no empirical parameters.

2.1.3. Basis sets

The electronic wavefunctions have not been described explicitly up to now. There are different possibilities to represent Ψ_i: A widely used set of basis functions are plane waves. Others are Gaussians, numerical atom-centered orbitals or wavelets.

Plane waves In an infinite solid where the electronic wavefunction is delocalized electrons are best described as a sum of plane waves of the form

$$\phi_j(r) = \frac{1}{\sqrt{\Omega}} \exp^{i(\mathbf{q_j}\cdot\mathbf{r})} \qquad \frac{\hbar^2}{2m}\mathbf{q_j^2} \leq E_{\mathrm{cut}}, \tag{2.7}$$

where Ω denotes the unit cell volume. The definition above has periodic boundary conditions

$$\phi(x+l) = \phi(x) \qquad q_j = \frac{2\pi}{l} j, \tag{2.8}$$

where l is the unit cell length.

Localized basis orbitals An example for a localized basis are the strictly confined atomic orbitals used in SIESTA. This confinement makes the basis orbitals zero beyond a certain radius. Within this radius, these orbitals are a product of a radial function and a spherical harmonic: For an atom i centered at R_i an atomic orbital becomes

$$\Phi_{\mathrm{ilmn}}(r) = \Phi_{\mathrm{iln}}(r_i) Y_{\mathrm{lm}}(\hat{r}_{\mathrm{i}}), \tag{2.9}$$

where $r_i = r - R_i$ and the indices l, m denote the angular momentum. In general there will be several orbitals (index n) with the same angular momentum, which then is called a multiple-ζ basis.

Bond formation induces a deformation and thus polarization. Therefore polarization orbitals are included in the basis set. They are calculated using a small electric field and first-order perturbation theory [9]. The resulting polarization orbital $\Phi_{l+1,m}(r) = N\phi_{l+1}(r)Y_{l+1,m}(\hat{r})$ are added to the basis set. Such a double-ζ plus polarization basis set is then called DZP and was used throughout this work when doing calculations with SIESTA.

Tradeoff The question which basis set to use is difficult to answer. Both have their advantages: the completeness of plane waves can easily be checked using more plane waves (*i. e.*, increasing the cutoff energy E_{cut}). They naturally satisfy orthonormality relations. One large disadvantage is their uniform spatial resolution. When describing systems with large unit cells and only a few atoms, like molecules or nanowires, a lot of vacuum is filled with plane waves. Atomic orbitals then are preferable, where matrix elements between non-overlapping basis functions are not stored during the calculation.

2.1.4. Pseudopotentials

The strength and character of the chemical bonds is dominated by the valence electrons. The strongly localized core electrons do only contribute little. In principle it is possible to expand the tightly bound core electrons. However, they are rapidly oscillating and a high number of plane waves is needed to describe them correctly. There are a number of all-electron codes, which can be interesting when looking at magnetic properties of materials. SIESTA uses localized orbitals on a real-space grid, which would have to be very dense for describing core electrons. To get rid of the core electrons the concept of pseudopotentials is introduced. The pseudopotential approximation removes the core electrons and the strong ionic potential by a weaker pseudopotential up to a certain cutoff radius r_{c}. Outside r_{c} the all-electron-potential and pseudopotential are equivalent. The corresponding valence wavefunctions look different compared to the all-electron case, they are smooth in the core region (see Fig. 5.3 on page 77 for an Cd all-electron and pseudo wave function). The all-electron valence wave functions strongly oscillate near the core to maintain orthogonality with the core electron wavefunctions. Outside a specific radius, the wavefunction are equal, thus the scattering properties of the pseudopotential and all-electron potential are the same.

2.1.5. Phonons

A system of N coupled oscillators has $3N$ normal modes. The atoms in a solid can be understood as such a system and all normal modes as lattice vibrations. A quantized lattice vibration then is referred to as a phonon. Phonons contribute to heat transfer in a solid. Furthermore they affect the conductivity which is limited by electrons being scattered by phonons. Currently, DFT calculations of phonon frequencies are in agreement with experimental frequencies within $\approx 5\,\%$. This is remarkable, as there are no adjustable parameters during the calculation. The

same holds for the calculation of other ground-state properties such as static dielectric constants, effective charges, stress-strain relations, electron-phonon interactions that were determined in this thesis. This states the success of current theoretical models for these kinds of ground-state properties.

Different methods exist for the calculation of phonon frequencies, one possibility is the so-called frozen phonon method, another solving the dynamical matrix. These two will be discussed in the following. A third way is used in molecular dynamics *via* Fourier transform of the vibrations.

Frozen phonon approach

With DFT total energies of a system can be calculated. The *value* of the total energy, in general, has no physical reason: This is due to the several approximations that are made beforehand, most severely the pseudopotential approximation. The kinetic energy of the core electrons is completely missing. Absolute *differences* in total energy are physically relevant and can be used to extract magnetic ground state configuration, surface passivation-s, surface reconstructions, phonon frequencies etc.

Making use of these energy differences phonon frequencies can be calculated in the following way: Imagine a wave through a crystal with a fixed wave vector $\mathbf{q}$ that propagates through the crystal. Now consider to make a snapshot of the vibration with a non-vanishing amplitude. This snapshot of the 'frozen' structure has a lower symmetry and a higher total energy than the relaxed system. If $E_{\mathrm{tot}}(0)$ and $E_{\mathrm{tot}}(u)$ are the total energy of the relaxed and the distorted structure, respectively the frequency ω of the 'frozen phonon' is defined by [10]

$$\frac{1}{2}\omega^2 \sum_b m_b |\mathbf{u}(b)|^2 = E_{\mathrm{tot}}^{\mathrm{harm}}(u) - E_{\mathrm{tot}}(0). \tag{2.10}$$

$E_{\mathrm{tot}}^{\mathrm{harm}}$ is the harmonic part of the total energy, u is the displacement amplitude and $\mathbf{u}(b)$ is the displacement vector of the bth atom with mass m_b. Practically, the energy $E_{\mathrm{tot}}^{\mathrm{harm}}(u)$ is evaluated for several displacements u and a quadratic function is fitted to the resulting data.

One of the disadvantages of this method is that the eigenvectors of the phonon displacement have to be known *a priori*. For phonons other than in the zone-center supercells have to be created that are commensurate with the considered point in the Brillouin zone (see Fig. 3.17 and section 3.3).

Nevertheless, information on the vibration can be gained with the frozen phonon approach that would be undetectable by the following force-constant method, mainly because it uses the harmonic approximation. The anharmonicity of the E_{2g}-mode in graphene and nanotubes has been studied with the frozen phonon approach in sections 3.3 and 4.4. The anharmonicity of the E_{2g}-mode in MgB_2 is believed to play a role in superconductivity and has been studied with

this method in Ref. 11

Dynamical matrix

Making use of the harmonic approximation, that is, describing the system as a set of harmonic oscillators, it is possible to calculate the vibrational spectrum of molecules and crystals. Using the harmonic approximation is equivalent to expanding the ionic Hamiltonian only up to the second order. This implies that the vibrations have an infinite lifetime. The change in the ion Hamiltonian induced by a displacement u_{kl} (of ion k in unit cell l) can be described as [12]

$$H'(u_{kl}) = \frac{1}{2} M_k \ddot{u}_{kl}^2 + \frac{1}{2} \sum_{k'l'} u_{kl} \cdot \Phi(kl, k'l') \cdot u_{k'l'}. \tag{2.11}$$

The matrix $\Phi(kl, k'l')$ contains the force constants: The force on the ion (kl) induced by displacement of the ion $(k'l')$ is described by $-\Phi(kl, k'l') \cdot u_{kl}$ (compare with Hooke's law where the force is $F = -k \cdot x$). The force constant matrix possesses the same translational symmetry as the crystal, so using a Bloch waves ansatz

$$u_{kl}(q, \omega) = u_{k0} \cdot \exp i(q \cdot R - \omega t) \tag{2.12}$$

in Eq. (2.11) yields [12]

$$M_k \omega^2 u_{k0} = \sum_{k',l} \Phi(kl, k'0) \exp(-iq \cdot R_l) u_{k'0}. \tag{2.13}$$

Introducing the abbreviation

$$D_{kk'}(q) = \sum_l \frac{\Phi(lk, 0k')}{\sqrt{M_k M_{k'}}} \exp(-iq \cdot R_l) \tag{2.14}$$

this transforms into

$$\sum_{k'} \Big[D_{kk'}(q) - \omega^2 \delta_{kk'} \Big] u_{k'0} = 0. \tag{2.15}$$

$D_{kk'}(q)$ is called the dynamical matrix. By solving the secular equation in Eq. (2.15) the vibrational frequencies and eigenvectors can be found. This is usually done by diagonalization.

Polar crystals need special care: In polar crystals, some phonon modes induce a polarization which is governed by long-range coulomb forces. Fortunately the resulting force constants can be calculated separately and are added to the harmonic force constants. These sums of dipoles are slowly converging and extend over many unit cells. In section 5.2, where the phonon dispersion of CdSe is calculated we will go into more detail.

Symmetries are of great use for reducing the number of explicitly calculated force constants.

In general $(3N)^2$ force constants have to be determined. Making use of symmetry relations this number can be greatly reduced: The phonons in CdSe nanowires presented in section 5.3 were calculated using line group symmetries. The largest wire had a calculation time of 1 month, without exploiting the six-fold symmetry it would have been half a year. In nanotubes, which are single-orbit system, only 9 force constants have to be determined.

Force constants

Finite differences The force constants can be obtained by displacing one atom and calculating the induced forces on the other atoms ($k \approx \Delta F/\Delta u$). This is called finite differences [13]. Due to the translational symmetry, it is not simply possible to displace one atom, as this atom is displaced in every unit cell. In order not to introduce spurious results one has to use supercells and displace an atom in this supercell. As a rule of thumb, this displacement and the size of the supercell is chosen in such a way that the forces on the atoms at the edges on the supercell are small or negligible (This should be in the order of the force criterion used during the relaxation of the atoms). Using a too small unit cell results in deviations mainly at the zone center, see ,*e.g.* , Ref. 14 for Germanium.

Response functions Another possibility is to use second-order energy derivatives

$$\Phi(kl, k'l') = \frac{\partial^2 E_{\text{tot}}}{\partial u_{kl} \partial u_{k'l'}} \tag{2.16}$$

(In a simple picture this corresponds to $k = \partial F/\partial u$). This is often referred to as linear response and has been developed in the framework of density functional perturbation theory (DFPT) [15]. In general, response functions are described by a formula like

$$\text{property} = \frac{\partial(\text{variable})}{\partial(\text{strength})}. \tag{2.17}$$

Following this scheme several key quantities can be derived, *e.g.*, polarizability, elastic constants, piezoelastic constants, interatomic force constants

$$\text{interatomic force constant} = \frac{\partial F_i^s}{\partial u_j^t} \tag{2.18}$$

or Born effective charges

$$\text{born effective charge} = \frac{\partial d_i^s}{\partial u_j^t}. \tag{2.19}$$

The main advantage of this method is that the atoms are not displaced during the calculation, and thus it is possible to obtain the full vibrational spectrum from the unit cell only. It is

currently implemented in the DFT codes QUANTUM-ESPRESSO[†] and ABINIT[‡].

2.2. Raman scattering

If light encounters media it can be transmitted, absorbed or scattered. Elastically scattered light is called Rayleigh effect. Inelastic scattering of light by phonons is called Raman scattering, named after C.V.Raman [16, 17]. [§]

Raman scattering provides a powerful, non-destructive method to investigate the electronic and vibrational properties of a material. It gives information on the type and strength of chemical bonds, chemical stoichiometry, strain, etc. . Taking into account the geometry of the Raman setup and the polarization of the incoming and scattered light, symmetries of the Raman-active phonons can be deduced. Furthermore Raman scattering allows a look at quantum-mechanical processes, *e.g.* , the decay of phonons, can be determined with Raman scattering. In resonant Raman experiments, well defined excited states are involved, so their optical properties can be studied.

2.2.1. First order Raman scattering

A scheme for non-resonant Raman scattering is shown in Fig. 2.1(a). Horizontal solid (dashed) lines indicate real (virtual) electronic states in the valence and conduction band respectively. Solid arrows denote electronic transitions induced by photons. Dashed arrows denote phonon assisted transitions, with a phonon energy of $\hbar\omega$. Grey arrows indicate non-resonant transitions whereas black arrows indicate resonant transitions. An electron is excited by a photon with energy E_l ①, is then scattered by a phonon with energy $\hbar\omega$ ② and finally recombines by emitting a photon with energy $E_l - \hbar\omega$ ③. The process is called non-resonant if both intermediate states are virtual. If the incoming energy E_l matches a real electronic transition [Fig. 2.1(b)] the process is called single-resonant. If both intermediate states are real [Fig. 2.1(c)] higher resonance occurs. The electronic bands then exhibit three levels with energy differences E_l, $\hbar\omega$, and $E_l - \hbar\omega$. The last, very restrictive, condition has been fulfilled experimentally by tuning the band gap by applying uniaxial stress [18], a magnetic field that produces spin splitting [19] or using an electric field [20].

The conservation of quasi-impulse must be maintained during the process. The wave vector of visible light is very small compared to the extension of the Brillouin zone. Thus in this laser energy range only phonons from the Γ-point can contribute to the Raman processes described. I the next section I will extend the discussion to higher-order processes that allow phonons with $q \neq 0$.

[†] www.quantum-espresso.org
[‡] wwww.abinit.org
[§] In 1930 C. V. Raman was awarded the Nobel prize in physics for experimentally verifying Raman scattering.

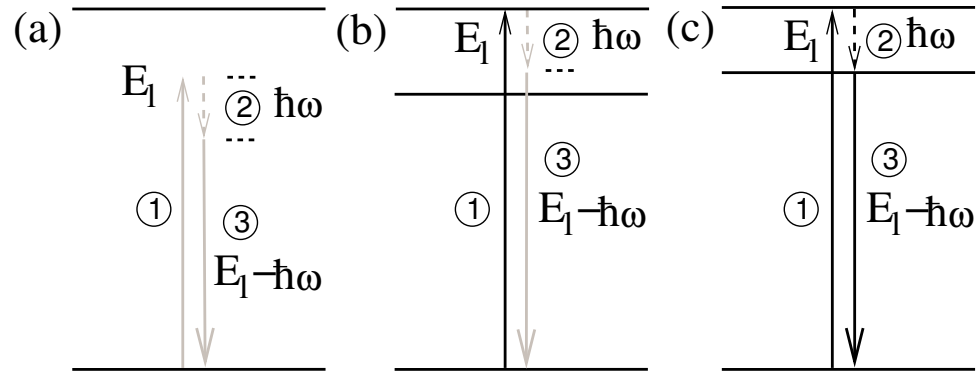

Figure 2.1.: (a) Non-resonant Raman scattering, (b) single-resonant Raman scattering, and (c) double-resonant Raman scattering. Horizontal solid (dashed) lines indicate real (virtual) electronic states in the valence and conduction band. Solid arrows denote electronic transitions induced by photons. Dashed arrows denote phonon assisted transitions with phonon energies of $\hbar\omega$. Grey arrows indicate virtual transitions whereas black arrows indicate real transitions.

2.2.2. Double-resonant Raman scattering

To illustrate a double-resonant Raman process that can explain the excitation-energy dependence of the modes, I consider the scattering in an idealized electronic band scheme. In Fig. 2.2(a) an incoming photon with laser energy E_l resonantly excites an electron-hole pair ($i \rightarrow a$). The excited electron can be scattered by phonons with arbitrary wave vector q. The scattering probability will be especially high if the phonon scatters the electron from the real electronic state a into another real electronic state b [$(a \rightarrow b)$ in Fig. 2.2(b)]. From there the electron is scattered back elastically to a virtual state c ($b \rightarrow c$), where the electron-hole pair finally recombines ($c \rightarrow f$), emitting the photon energy $E_l - \hbar\omega(q)$(Stokes scattering). In Fig. 2.2(c) the same process is shown with a larger incident laser energy $E_l' > E_l$. A phonon with different wave vector q' and, assuming the phonon dispersion of Fig. 2.2(d), with smaller energy $\hbar\omega'$ is selected by the double-resonant process. This leads to a downshift of a double-resonant peak in the Raman spectra with increasing incident energy.

In Fig. 2.2(b) the incoming light is in resonance with the electronic states (incoming channel). Alternatively, the scattered light can be in resonance with the electronic states (outgoing channel). Other possible processes are in different chronological order, anti-Stokes scattering, or hole scattering.

The cross section $K_{2f,10}$ of a Raman process can be calculated by [21, 22]

$$K_{2f,10} = \sum_{a,b,c} \frac{M_{cf} M_{bc} M_{ab} M_{ia}}{(E_l - E_{ai} - i\hbar\gamma)(E_l - \hbar\omega - E_{bi} - i\hbar\gamma)(E_l - \hbar\omega - E_{ci} - i\hbar\gamma)}, \tag{2.20}$$

where E_{ai} is the energy difference between the electronic states i and a [correspondingly for the other electronic states as denoted in Fig. 2.2(b)]. E_l and $E_l - \hbar\omega$ are the energies of the

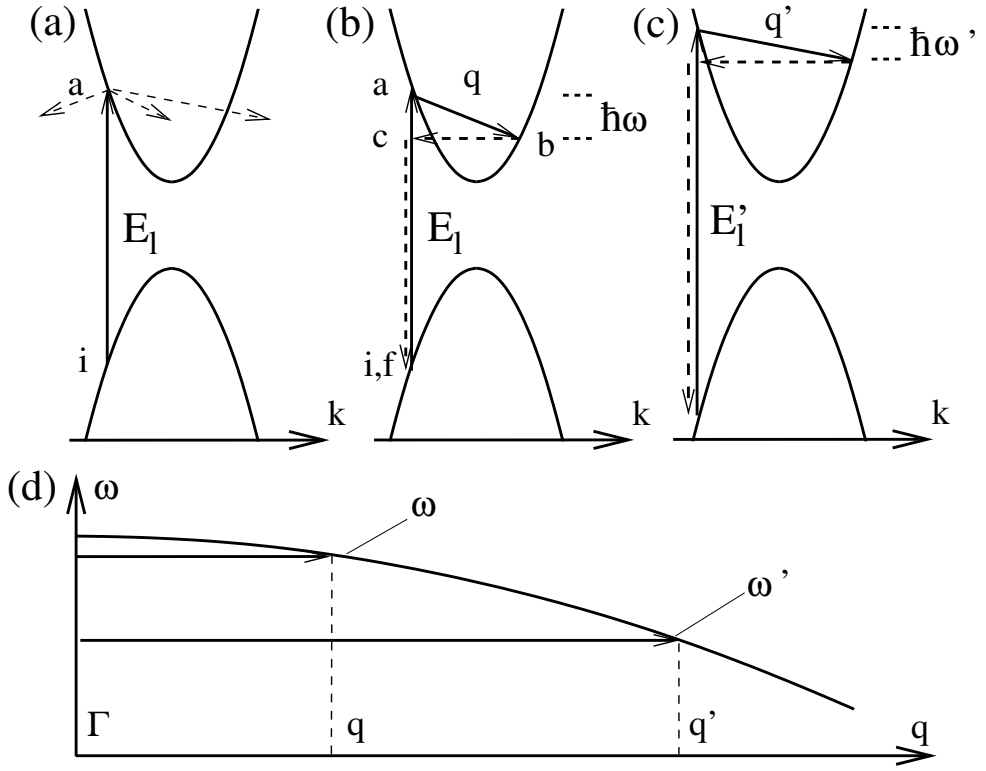

Figure 2.2.: Double-resonant Raman scattering for symmetric parabolic bands with a band gap and a parabolic phonon dispersion (For double-resonant Raman scattering with linear bands see Fig. 3.27). (a) Resonant excitation of an electron-hole pair followed by non-resonant scattering of the electron. (b) Double-resonant Raman scattering process. An electron is excited by a photon with energy E_l ($i \to a$) and scattered by a phonon of frequency ω and momentum q ($a \to b$). It is scattered back elastically ($b \to c$) and finally recombines ($c \to f$). (c) For a different incoming photon energy E_l' the double-resonant condition selects a different phonon (ω', q'). (d) Idealized vibrational dispersion curve showing the two phonons with momentum q and q'.

incoming and outgoing photon, respectively. M_{xy} is the matrix element for the scattering over the intermediate states x and y and γ is the broadening parameter of the electronic transitions.

The double-resonance is particularly strong as two of the expressions in the denominators of Eq. (2.20) vanish. Double-resonances are known to occur in Graphene, nanotubes and Germanium. [14, 23]

3. Graphene

Graphite is known from everyday use, *e.g.* , from pencils, in electro motors or as dry lubricant. The most abundant configuration at ambient conditions possesses a hexagonal crystal structure. In this structure one atom-layer thick sp^2-hybridized carbon sheets are stacked in $ABAB$ configuration. A single layer of graphite is called graphene. Graphene gained considerable interest, after carbon nanotubes were discovered in 1991 [24]. Carbon nanotubes can be regarded as one or more rolled-up graphene sheets. Many physical properties of carbon nanotubes are closely related to those of graphene which led to an increased theoretical interest in graphene [23, 25]. The recently developed preparation of graphene sheets [26, 27] has led to a huge interest in the fundamental physical properties of graphene itself during the last years. Graphene has been shown to possess unique material properties: In graphene the quantum Hall effect could be observed at room temperature [27, 28]. The extraordinary band structure at the Fermi level makes the description of the electrons as massless Dirac fermions possible [28]. In this way they mimic relativistic particles with zero rest mass and with an effective 'speed of light' $c' \approx 10 \cdot 10^6\,\mathrm{m/s}$ [29]. These remarkable features are promising for applications. Ballistic transport of electrons has been achieved over a few hundred lattice sites on sub-μm-distances which can be exploited for electronic devices [30]. The spin transport over similar length scales allows for applications like spin-injection and spin-valves [31]. The high electron mobility is remarkable, too: $\mu \approx 20000\ \mathrm{cm^2/Vs}$ compared to Si: $\mu \approx 1500\ \mathrm{cm^2/Vs}$ [32]. Also at 300 K the electron mobility still is impurity limited and only little by temperature [30]. This was measured for graphene on a substrate. Defect-free free-hanging graphene has been reported to show mobilities of up to $\mu \approx 1000000\,\mathrm{cm^2/Vs}$

Besides these remarkable phenomena, there are still unknown fundamental properties of graphene, *e.g.* , its phonon dispersion has not been completely resolved by experiment. In this chapter we present the full in-plane phonon dispersion of graphite obtained from inelastic x-ray scattering. Allowing a broad audience to make use of this data we fit a fifth-nearest neighbour force-constants model to the experimental data. Electron-phonon interaction strongly softens phonon frequencies in graphene (and in metallic carbon nanotubes). The effect of electron-phonon coupling will be analyzed for the high-symmetry points Γ, K, and M with density functional theory (DFT). DFT will also be used to investigate effects of strain on graphene regarding the electronic and vibrational spectrum and the Raman-active modes. In the last part of this chapter I show recent calculations on small stripes of graphene, the so-called graphene

nanoribbons (GNR). GNR not only show a confinement in dimension but also the exact geometry lead to distinctive properties such as band gaps or shifted Raman frequencies.

3.1. Introduction

The unit cell of graphene, which contains two atoms, is shown in Fig. 3.1. The resulting crystal structure is hexagonal with a carbon-carbon distance of $a_{cc}=1/\sqrt{3} \cdot a_0 = 1.422\,\text{Å}$.

Graphite consists of graphene sheets arranged in an $ABAB$-stacking. Its unit cell contains four atoms. The two additional atoms are slightly displaced such in a way that one atom is still on top of an atom in the layer below. The other atom is in the center of the hexagon in the plane below. The positions and coordinates are given in Fig. 3.1 and the caption.

The corresponding Brillouin zone is shown in Fig. 3.2. The irreducible part of the Brillouin zone is shaded in grey. Points of high-symmetries are the K and the M-point. Lines of high-symmetry are T and Σ, connecting the Γ-point with the K and M-points, respectively. The distinction into K and K' does not come from symmetry, but from tight-binding results. For electrons being on a K-site it is energetically more favorable to hop onto a different K-site than to a nearer K'-site.

Graphite is a highly anisotropic material: the nearest-neighbor distance between two atoms in the plane is $a/\sqrt{3} \approx 1.42\,\text{Å}$, while the inter-layer distance is $c/2 \approx 3.35\,\text{Å}$. This has several consequences: The weak interlayer interaction makes sure that the properties of graphene and graphite are very similar. On the other hand the crystal structure of graphite is remained only over a a few hundred microns. Larger samples are a collection of micro-crystallites oriented in random ways.

The extraordinary strong absorption allows to see a single atomic layer of graphene with an optical microscope. Such an image of a graphene flake suspended on a 300 nm SiO_2 buffer layer, which was recorded with the conventional optical microscope at our Raman setup, is shown in Fig. 3.4. The sample itself was prepared using the so-called scotch-tape method [26], where scotch tape is first pressed on graphite flakes, peeled off, and then pressed on the substrate. Due to the weak inter-layer forces single and multilayer graphene sheets are thus suspended on the substrate.

Another possibility to obtain information on graphene is Raman spectroscopy. As discussed in Sec. 2.2.1 first order Raman scattering only gives information on the phonons in the zone center. The peculiar band structure of graphene allows for the detection of other phonons by higher ordering scattering processes. In Fig. 3.5 we plot a typical Raman spectrum of a graphene flake. All labeled modes but the E_{2g}-mode show an excitation-energy dependent shift. This is an indication of higher-order processes (see section 2.2.2). The criterion whether or not a flake is single layered is the full-width at half-maximum (FWHM) of the $2D$-mode [33]: if it is smaller than $30\,\text{cm}^{-1}$ one has a single layer.

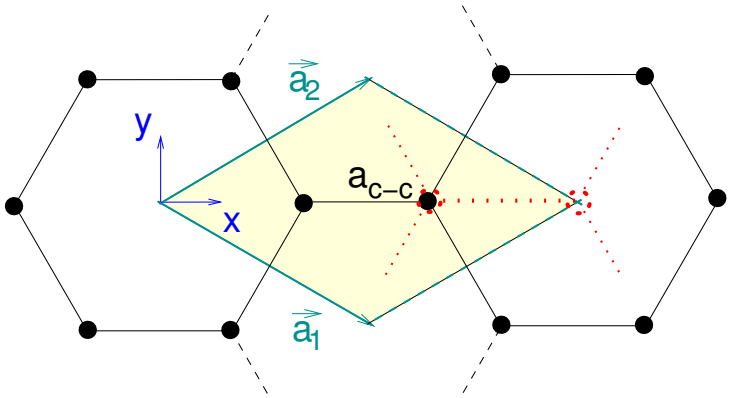

Figure 3.1.: The unit cell of graphene. The lattice vectors are $\vec{a_1} = a_0 \cdot (\sqrt{3}/2, -1/2, 0)^T$ and $\vec{a_2} = a_0 \cdot (\sqrt{3}/2, 1/2, 0)^T$ (The third lattice vector in direction $(0, 0, 1)^T$ has to be chosen large enough to avoid interaction and is only needed in three-dimensional calculations). The lattice constant is a_0=2.463 Å. Carbon atoms are at the positions $(1/3, 1/3, 0)$ and $(2/3, 2/3, 0)$ (in lattice vectors). The carbon-carbon atomic distance is $a_{cc}=1/\sqrt{3} \cdot a_0 = 1.422$ Å.
The unit cell of graphite contains two more atoms that lie in a parallel plane, with an *ABAB*-stacking. The positions of these additional two atoms are $(2/3, 2/3, 0.5)$ and $(1, 1, 0.5)$. In the figure this lattice is depicted in red points. The third lattice vector is then $\vec{a_3} = (0, 0, c)^T$, where c is twice the interlayer distance.

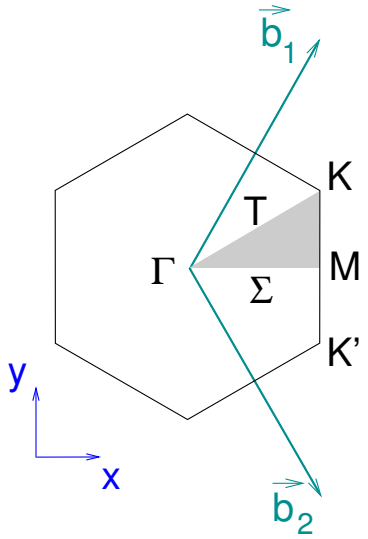

Figure 3.2: The Brillouin zone of graphene corresponding to the unit cell from Fig. 3.1. The irreducible part of the Brillouin zone is shaded in grey.

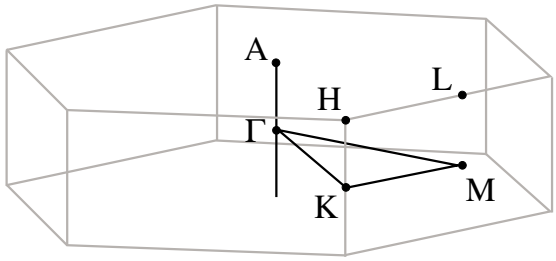

Figure 3.3.: Brillouin zone of graphite. The two-dimensional Brillouin zone of graphene consists of the hexagon that lies in the plane with the points Γ, K and M. The distances between the high-symmetry points are $\Gamma - K = 4\pi/3a$, $\Gamma - M = 2\pi/\sqrt{3}a$, and $K - M = 2\pi/3a$.

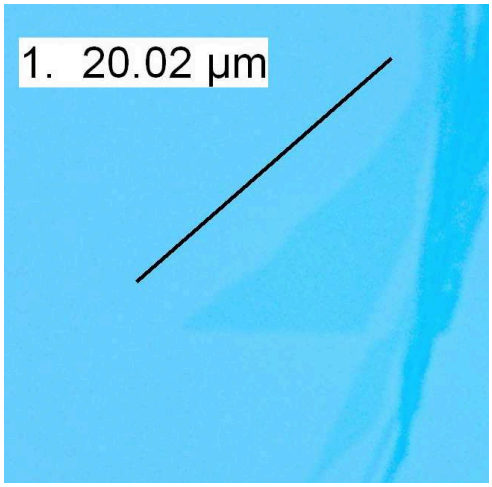

Figure 3.4: Image of a graphene flake viewed with an optical microscope. On the right hand side of the flake are thicker graphene layers. This sample was deposited on a silicon substrate with a 300 nm SiO_2 buffer layer. This layer strongly increases the visibility with an optical microscope.

3.2. Inelastic X-ray scattering

The fundamental characteristics of a crystalline material comprise its phonon spectrum, from which one can derive several other physical properties such as sound velocity, thermal conductivity, or heat capacity. Furthermore, phonons play an important role in excited-state dynamics and electrical transport properties. Optical or electronic excitations can decay into vibrational excitations or can be scattered by phonons into different states. For example, in carbon nanotubes the high-bias electrical transport is assumed to be limited by scattering of the carriers by optical phonons near the graphite K point [34, 35].

The phonon dispersion of graphite has not been completely resolved by experiment, mostly due to the lack of large enough samples of crystalline quality. It has been partly measured by inelastic neutron scattering (INS), electron-energy loss spectroscopy (EELS), and inelastic x-ray scattering (IXS) [36–40]. Most experiments so far have determined the dispersion along the $\Gamma - K$ and the $\Gamma - M$ directions in the graphite Brillouin zone (see Fig. 3.2 for the basal plane and Fig. 3.3 for the 3D Brillouin zone). The measurement of the optical branches along the $K - M$ direction by IXS pointed to the existence of a Kohn anomaly for the highest phonon branch at the K point [40,41]. Although this result resolved previous discrepancies between lattice dynam-

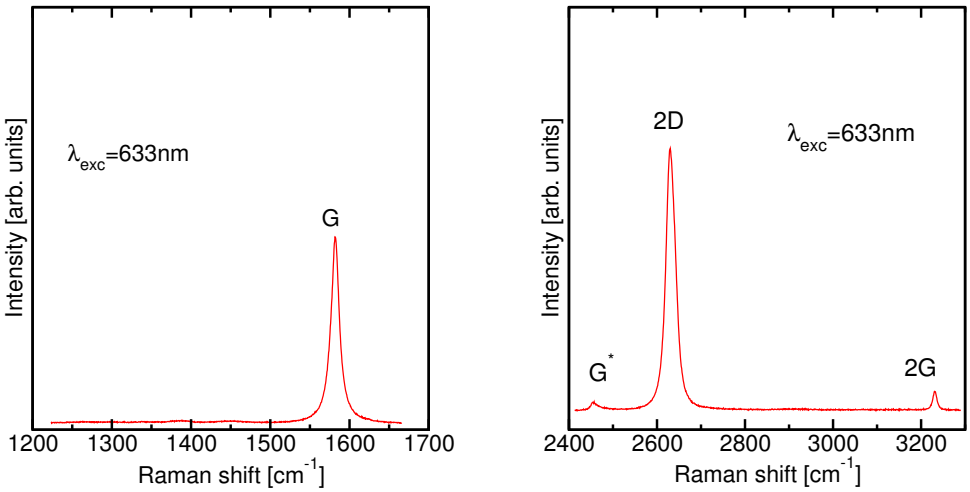

Figure 3.5.: Raman spectrum of a single layer of graphene: The spectrum shows several peaks. The G-band which is present in all sp^2 forms of carbon (also called E_{2g}-mode). The $2D$-mode which usually has stronger intensity than the E_{2g}-mode, and the two modes G^* and $2G$ at energies of $2450\,\mathrm{cm}^{-1}$ and $3200\,\mathrm{cm}^{-1}$, respectively. All modes shown in the right spectrum are excitation-energy dependent. Graphite exhibits an additional peak around $1350\,\mathrm{cm}^{-1}$, the D-mode. In contrast, there is almost no D-mode in a perfect layer of graphene. This defect-induced mode becomes stronger near the edges of a graphene flake or if there are defects in the layer.

ics models, there are still open questions regarding the shape of lower-lying phonon branches. In particular, differences appear between force-constants and density-functional theory (DFT) calculations, where experimental data are still unavailable. This concerns, e.g., the crossing between the acoustic and optical bands near the M-point or the energy of the transverse acoustic mode at the K point [42, 43]. For carbon nanotubes, the experimental determination of the phonon dispersion throughout the entire Brillouin zone would require monocrystalline samples of a minimum size, which have been unavailable so far. Therefore, the closest approximation to the experimental phonon dispersion of carbon nanotubes is currently the phonon dispersion of graphite.

In the following we briefly explain the principles of the IXS experiment. Then the phonon dispersion of graphite from inelastic x-ray scattering along the high-symmetry directions in the basal plane is presented. In particular, the phonon branches between the K and M point and the acoustic branches in all high-symmetry directions are obtained, giving both the optical and acoustic phonons from a single experimental technique. This data will be fitted by a set of force constants, including up to fifth-nearest neighbours of carbon atoms. These fitted force constants can be used to extract the phonon dispersion along arbitrary directions or to deduce the corresponding force constants for carbon nanotubes. This fit provides in-plane and out-of-plane force constants.

3.2.1. Introduction to IXS

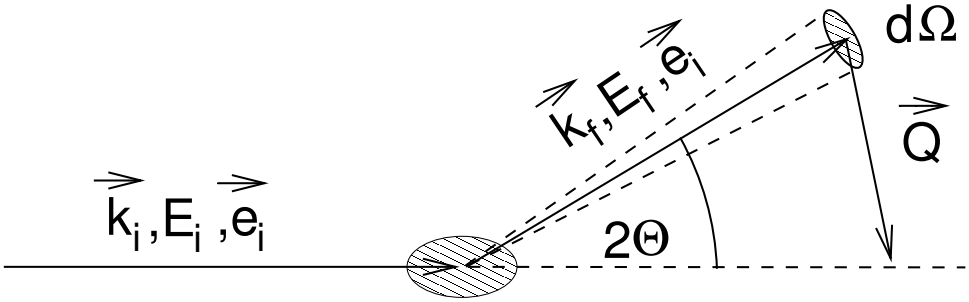

Figure 3.6.: Scattering geometry in momentum space of an energy loss experiment with impulse transfer. The incident beam is scattered into the solid-angle element $d\Omega$ by the angle 2Θ. The impulse transfer is $\mathbf{Q} = \mathbf{k_i} - \mathbf{k_f}$.

A general scattering experiment is schematically drawn in Fig. 3.6. The incident beam with wavevector $\mathbf{k_i}$, energy E_i and polarization $\mathbf{e_i}$ is scattered by the angle 2Θ into the solid-angle unit $d\Omega$. The scattered beam is characterized by the new wavevector $\mathbf{k_f}$, energy E_f and polarization $\mathbf{e_f}$. It contains contributions from elastically scattered photons as well as inelastically scattered ones that now have a different energy. For this reason the scattering process reveals information about energy and momentum transfer

$$E = \hbar\omega = E_i - E_f \tag{3.1}$$

$$\hbar\mathbf{Q} = \hbar(\mathbf{k_i} - \mathbf{k_f}) \tag{3.2}$$

As long as the energy transfer E is small (in the case of IXS $E \ll E_i$) the momentum transfer $\hbar Q$ is connected with the scattering angle Θ *via*

$$\hbar Q = 2\hbar k_i \sin\Theta. \tag{3.3}$$

In the experiment the white synchrotron beam is scattered by a monochromator crystal and then has a defined energy E_i and wavevector $\mathbf{k}_i$. A change in the energy transfer can be either achieved by a change in the scattering geometry or by a change of the lattice parameter difference between the monochromater and analyzer crystal. Such energy scans are called a constant-**Q**-scans. This is only feasible if the energy resolution is good enough. At the beam line ID28 at the European Synchrotron Radiation Facility (ESRF) in Grenoble the highest energy resolution of 1.0 meV is achieved with the Bragg reflection of a Si (13 13 13)-surface at a beam energy of 25.7 keV. This corresponds to an energy resolution of 1.0 meV/25.7 keV=$0.39{\cdot}10^{-8}$. More details can be found in the excellent reviews [44] and [45].

The setup of the beam line ID 28 is shown in Fig. 3.7. The energy of the incident radiation of 17794 eV was selected by the (999) Bragg reflection of a silicon crystal. We used a Si (999) crystal

which has a 20 times higher photon flux than the Si (13 13 13) crystal. The scattered photons were analyzed by five analyzers [also Si (999)]. The x-ray beam was focused to $250 \times 60\,\mu\text{m}^2$, selecting a single microcrystal in a naturally grown graphite flake. The typical size of a single grain was about 800 μm in lateral direction and 100μm along the c-axis. With x-ray diffraction we obtained the lattice parameters $a = 2.463\,\text{Å}$ and $c = 6.712\,\text{Å}$ as determined by so-called "rocking scans". This is in excellent agreement with previous neutron diffraction data ($a = 2.464\,\text{Å}$, $c = 6.711\,\text{Å}$) [46].

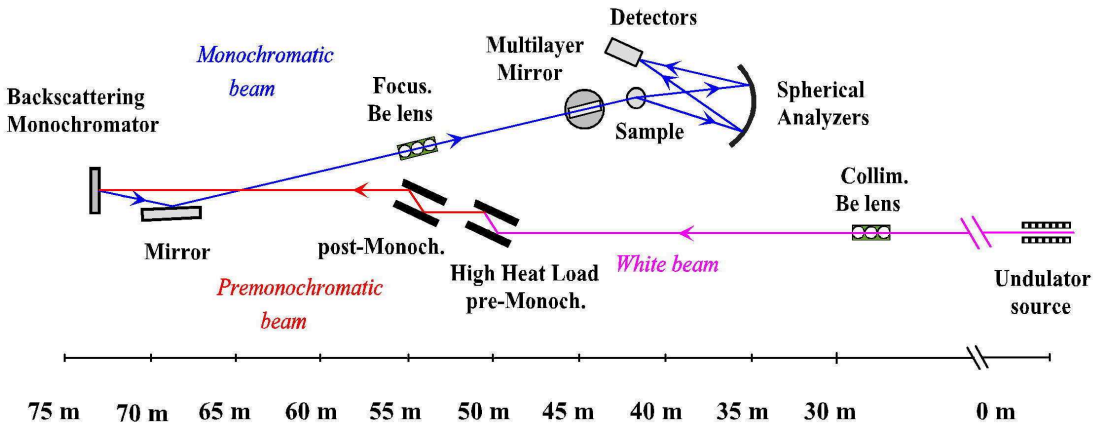

Figure 3.7.: Experimental setup. From http://www.esrf.eu

The inelastic scattering spectra were recorded by varying the temperature of the monochromator crystal. This leads to a temperature difference between the monochromator and the analyzer silicon crystal and with that to a different lattice parameter. An exemplary spectrum is shown in Fig. 3.8.

To minimize the effects of temperature drifts that could result in an energy offset, we recorded systematic Stokes–anti-Stokes scans between the measurements. In our setup the c-axis of graphite and the scattering plane encompasses an angle of 90°, 30°, and 0°, depending on the phonon branch under consideration. The scattering geometry was chosen according to the selection rules, see Ref. 47, and their excellent website http://www.cryst.ehu.es.

3.2.2. IXS results

The unit cell of graphene contains two atoms, resulting in six phonon branches. The unit cell of graphite consists of four atoms, which leads to twelve phonon branches. The space group of graphite is $P6_3/mmc$ (international notation). At the Γ point it possesses the factor group 6/mmm (D_{6h} in Schönfliess notation). The optical zone-center modes of graphene are decomposed into $\Gamma = B_{2g} + E_{2g}$. In graphite, the optical zone center modes are decomposed

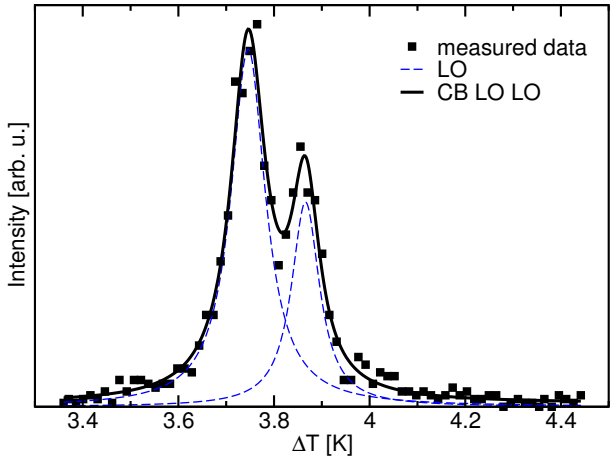

Figure 3.8: Inelastic scattering spectra of graphite at the M-point. The x-axis corresponds to the temperature difference between the monochromator and analyzer crystal in units of Kelvin. The black line is a fit to the experimental data. The underlying Lorentz functions are displayed in broken blue lines. This spectrum was recorded in 73 minutes.

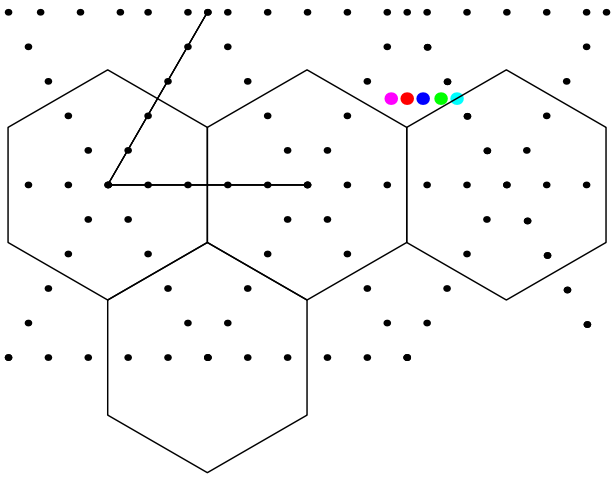

Figure 3.9: Position of the 5 detectors in the reciprocal space of graphene (colored dots). Although barely visible here, the detectors lie on a curve. Here analyzer 2 (red) is at the position $q = (1.25, 0.5)^T$. In addition, analyzer 5 (cyan) is very close to the K-point $(1.499, 0.4951)^T$.

into $\Gamma = A_{2u} + 2B_{2g} + E_{1u} + 2E_{2g}$ [48–50]. The A_{2u} and E_{1u} modes are IR active, the E_{2g} modes Raman active. The B_{2g} modes are optically inactive, but can be measured via INS or IXS. The three acoustic modes are decomposed into $\Gamma = A_{2u} + E_{1u}$.

The bonds between two carbon atoms in the plane are much stronger than the weak van-der-Waals interactions between the layers. The carbon-carbon distance is $a_{cc}/\sqrt{3} \approx 1.42\,\text{Å}$, while the inter-layer distance is $c/2 \approx 3.35\,\text{Å}$. Therefore one expects that the phonon modes of graphite correspond approximately to that of graphene but split into in-phase and out-of-phase vibrations of two neighboring graphene planes. Most of the phonon branches in graphite are nearly doubly degenerate [41, 51]. Only close to the Γ point, the acoustic modes of graphene split in graphite into acoustic modes (in-phase vibration of the graphene sheets, 0 meV) and optical modes [out-of-phase vibration of the graphene sheets; in-plane: E_{2g} at 5.2 meV (42 cm^{-1}); out-of-plane: B_{2g} at 15.7 meV (127 cm^{-1})]. For the optical modes of graphite, the difference between the in-phase and the out-of-phase vibrations is very small: at the Γ point the IR active E_{1u} mode is found at 196.9 meV (1588 cm^{-1}), close to the Raman active E_{2g} mode at 196.0 meV (1581 cm^{-1}). The same holds for the A_{2u} mode at 107.5 meV (867 cm^{-1}) [48, 52] and the B_{2g} mode at 107.6 meV (868 cm^{-1}). Therefore, in the following theoretical discussion, we will consider the phonons of a single graphene sheet.

The six branches are divided into the out-of-plane acoustic mode ZA, the in-plane acoustic mode TA (sometimes called SH=shear), the longitudinal acoustic mode LA, the out-of-plane optical mode ZO, the in-plane optical mode TO (SH*), and the longitudinal optical mode LO. Four branches belong to modes where the atoms move in-plane within the graphene layer (TA, LA, TO, LO); two branches belong to transverse modes, where the atoms move out-of-plane (ZA, ZO).

In Fig. 3.10 we show our experimental data of the graphite phonon dispersion in the plane. The lines show the fifth-nearest neighbor force-constants fit described in Sect. 3.2.3. The optical phonon frequencies near the Γ point agree well with previous experiments. We find the E_{2g} LO mode at 196.0 meV (1581 cm^{-1}), and the B_{2g} mode at 107.6 meV (868 cm^{-1}). Regarding the overall shape of the phonon branches, our experiments confirm previous *ab-initio* DFT calculations, letting aside the special situation for the highest branch at the K point [40, 41, 51, 53, 54]. This results from a Kohn anomaly, a strong electron correlation that can hardly be detected by DFT, with single-particle approximations. Recent calculations that include GW-corrections are able to reproduce the frequencies at K [55].

The highest optical frequency is not at the Γ-point. Instead, the phonon frequency first increases with growing wavevector and then decreases again. This effect, which is called over-bending, has been observed in diamond as well [56] but also in other hexagonal crystals (CdSe, see Sect. 5.2). In graphite, it is amplified by a Kohn anomaly at the Γ-point, i.e., the frequency is lowered due to interaction of the phonon with the electronic system [40, 41]. Another Kohn anomaly in graphite can be found for the TO-derived phonon branch at the K-point (fully sym-

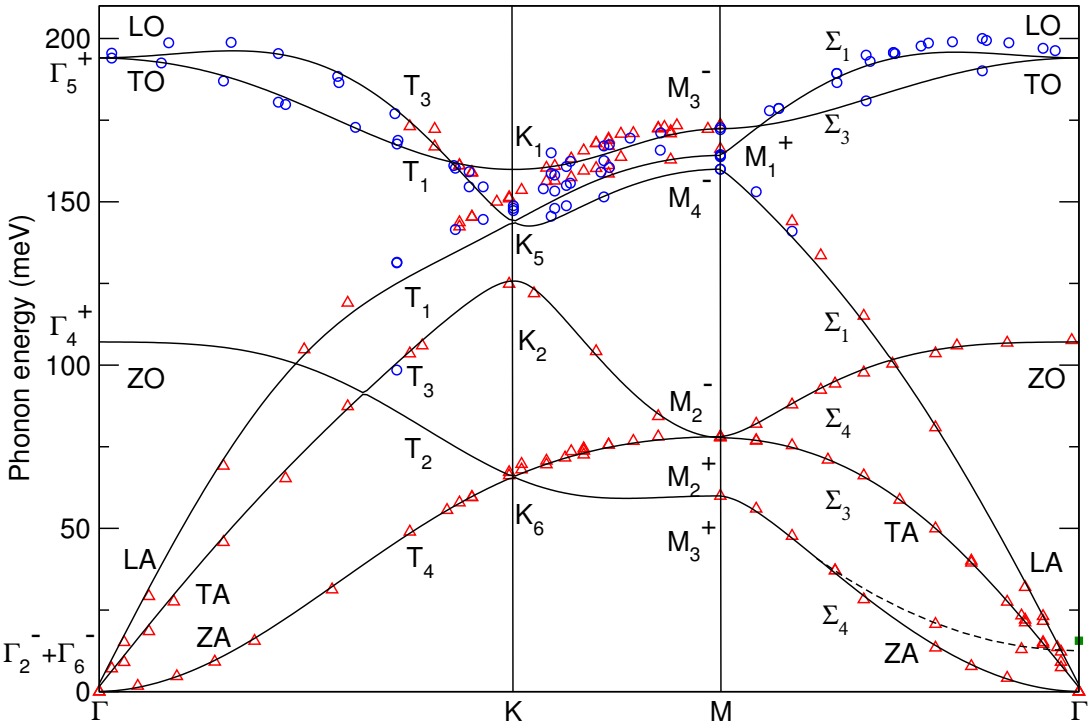

Figure 3.10.: Phonon dispersion of graphite from inelastic x-ray scattering (symbols). Triangles are present data, circles are data already published in Ref. 40. The full square at the Γ point is INS data from Ref.36. Solid lines are the force-constants calculations from the 5th-nearest neighbor fit discussed in Sect. 3.2.3; the dashed line is a quadratic extrapolation of the data. The lines are denoted by their symmetry representation in space group notation. The relation between space group and molecular notation can be found in Table 3.1.

metric A_1' (K_1) mode). We were not able to detect the A_1' phonon directly at the K point. The strong electron-phonon interaction has been predicted to reduce the phonon lifetime which results in a line broadening. Probably the large line width makes it very difficult to detect the A_1' phonon at the K point experimentally. The lack of beam time left this question opened. However, recent experiments have scanned the vicinity of the K-point and have measured the fully symmetric A_1' (K_1) mode [55].

Considering the differences between previous theoretical models, we find the following results (see also Sect. 3.2.3): Between the Γ and M points, the ZO and TA modes do not cross within our experimental error of 3 meV. This is in contrast to previous empirical force-constants models and EELS data of Ref. 37. The question, which branch is higher directly at the M point cannot be uniquely distinguished from our data. However, in DFT phonon calculations the crossing is found between K and M but close to M (about 1/10 of the distance between K and M, see Ref. 54). The overall agreement with DFT calculations supports the crossing between K and M. (see Fig. 3.11)

The TA branch along $\Gamma - M$ shows a smaller increase compared to the electron energy loss

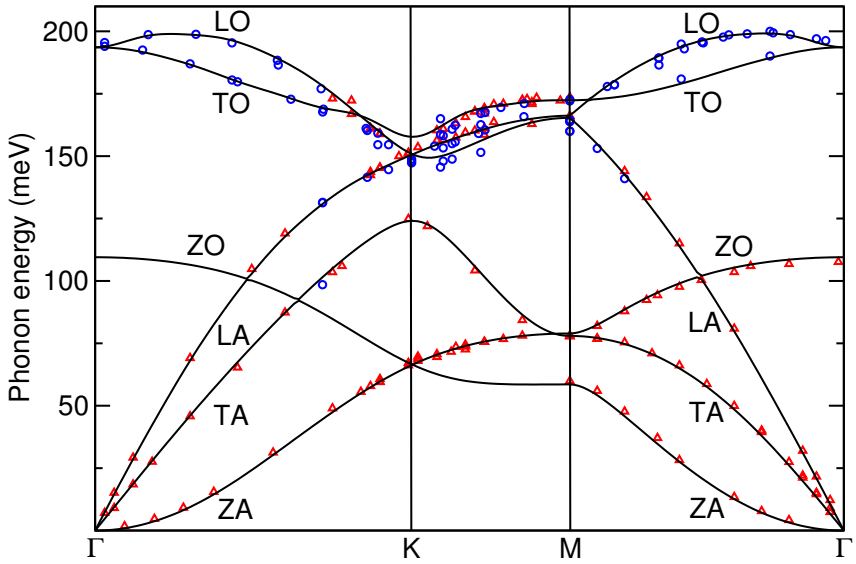

Figure 3.11.: Phonon dispersion of graphite. Symbols are experimental data from IXS, lines are from DFT calculation. Details are given in Sec. 3.4. Same symbols as in Fig. 3.10 were used.

spectroscopy (EELS) data in Ref. 37. In a recent EELS experiment on epitaxially grown thin graphene sheets, [39] however, this branch could not be detected , as the shear modes in graphene are forbidden in EELS. The crystalline quality of Ref. 37 seems to be lower, softening the selection rules. This may explain why previous empirical models, relying on this data, predicted a larger slope of the TA branch and consequently a crossing of the ZO and TA modes between the Γ and M points.

We measured for the first time the ZA and TA mode between the K and M points. Our results confirm predictions made by *ab-initio* calculations very well, and are also well reproduced by our force-constant fit. The trend of both branches crossing near the M point can be recognized.

The two optical phonons at the M point derived from the LO and LA branches are very close in frequency ($< 4\,\mathrm{meV}$), and we were not able to distinguish them clearly by symmetry. It appears, however, in accordance with DFT calculations and the force constants fit in Sect. 3.2.3 that the higher frequency has M_1^+ symmetry and the lower one M_4^-. As a consequence, the LO- and LA-derived branches cannot cross between the K and M point.

In Fig. 3.12 we show the low frequency phonon range along the $\Gamma - A$ direction, i.e., perpendicular to the in-plane directions (see Fig. 3.3). For comparison, we also present the INS data on highly oriented pyrolytic graphite from Ref. 36. They are in excellent agreement. The high-frequency phonon range is expected to show almost no dispersion along the $\Gamma - A$ direction [51].

Due to experimental reasons we were not able to record data points from the ZO branch along the $\Gamma - K - M$ direction. This branch has been measured in recent EELS experiments of Ref. 39. In general, the data of Ref. 39 agrees well with ours, but at the K-point the ZO and ZA branches in Ref. 39 show a relatively large splitting of $\approx$10 meV. They cannot stem from the degenerate

K_6-phonon, but could possibly represent the out-of-phase modes of the graphite planes. On the other hand, in DFT calculations of graphite [51] this splitting seems much smaller than indicated by the EELS data.

Regarding the phonon modes specific for graphite with more than one layer, we find the low-energy out-of-phase modes near the Γ point. These are indicated by the dashed line in Fig. 3.10. We measured two out-of-phase ZO′ phonons in the $\Gamma - M$ direction, with energies 13.6 meV and 23.3 meV at 0.16 of the $\Gamma - M$ distance and at 0.4 $\Gamma - M$, respectively. A quadratic extrapolation leads to a value of 12.5 meV at the Γ point, in agreement with 15.7 meV from neutron scattering data [36].

The optical-phonon frequencies at the high-symmetry points from our experiment are summarized in Figs. 3.14, 3.15, and 3.16 together with the displacement patterns obtained by the force-constants calculations presented in Sect. 3.2.3. The acoustic phonon branches near the Γ point provide information on the elasticity and sound velocities of graphite which we reported in [57].

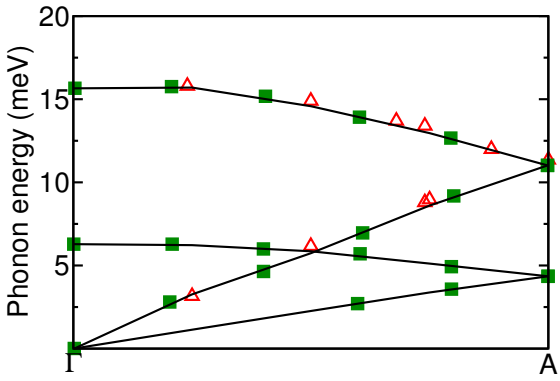

Figure 3.12.: Phonon dispersion of graphite along the $\Gamma - A$ direction. Open triangles are present IXS data, full squares are neutron scattering data from Ref. 36. The lines are a guide to the eye.

3.2.3. Determination of the full phonon dispersion from experiment

Phonon dispersion relations are often predicted from *ab-initio* DFT or from empirical force-constants (FC) calculations. Empirical force-constants models in graphite have so far included up to 4th-nearest neighbors, in order to reproduce the overbending of the optical branch near the Γ point [42, 58]. In the case of graphite, besides the details regarding the frequency values, both methods show differences in the shape of phonon branches, e.g., the position of the crossing of the ZO and TA modes near the M point. While in FC calculations a crossing of the ZO and TA branches between the Γ and M points is predicted (for example in Ref. 58), it is found in *ab-initio* results to take place between K and M. This probably stems from a fit to the only available TA mode from EELS experiments (Ref. 37).Further differences between force-constants

and *ab-initio* DFT calculations are found regarding the LA and LO branches near the M point: In DFT results, the LO-derived phonon branch is higher than the LA phonon at the M-point, and, as a result, the two branches do not cross between M and K, in contrast to most predictions by empirical force constants.

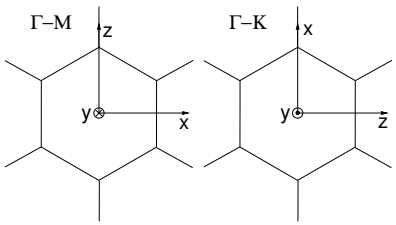

Figure 3.13.: Coordinate system for the point group C_{2v} of $\Gamma - M$ and $\Gamma - K$ drawn in real space. z points in the direction of the principal rotational axis.

Table 3.1.: Symmetry relations between space group and molecular notation for the space group $P6_3/mmc$ and the point group D_{6h}. The corresponding coordinate system for C_{2v} is shown in Fig. 3.13.

Γ	D_{6h}	K	D_{3h}	M	D_{2h}	T, Σ	C_{2v}
Γ_2^-	A_{2u}	K_1	A_1'	M_1^+	A_{1g}	T_1, Σ_1	A_1
Γ_4^+	B_{2g}	K_2	A_2'	M_2^+	B_{1g}	T_2, Σ_2	A_2
Γ_6^-	E_{1u}	K_5	E'	M_2^-	B_{1u}	T_3, Σ_3	B_1
Γ_5^+	E_{2g}	K_6	E''	M_3^+	B_{2g}	T_4, Σ_4	B_2
				M_3^-	B_{2u}		
				M_4^-	B_{3u}		

Fitting procedure

To obtain the optimal fit of the set of force constants to the experimental data, we applied a variable neighbor search (VNS) method of global optimization [59], using the simplex method [60] for the local optimization subroutine. Basically, this is the least squares procedure minimizing the average deviation $\Delta(\mathbf{f}) = \frac{1}{N^{\mathrm{exp}}}\sqrt{\sum_i |\omega_i^{\mathrm{exp}} - \omega_i(\mathbf{f})|^2}$ between the $N^{\mathrm{exp}} = 96$ experimental values, ω_i^{exp}, and the corresponding calculated frequencies, $\omega_i(\mathbf{f})$, obtained by calculation with the trial values of the force constants $\mathbf{f} = (f_1, \ldots, f_F)$. Due to symmetry, for each level of the 3 or 6 neighbor atoms the same triple of force constants can be used. We used stretching, out-of-plane and in-plane force constants f_i for each relevant pair of atoms [58, 61]. Here, the direction of stretching corresponds to the line that connects the center atom with the atom of appropriate level. The in-plane and out-of-plane directions are perpendicalur to this line and lie in the graphene layer or perpendicular to it, respectively. After transforming the stretching and in-plane force constants to a global basis, one obtains the dynamical matrix. The level of the relevant neighbors has been gradually increased until a satisfactory agreement ($\Delta <$

0.23meV, with the greatest difference of $|\omega_i^{\mathrm{exp}} - \omega_i(\mathbf{f})| \approx 8\,\mathrm{meV}$ for the LA branch in the $\Gamma - K$ region, nearby the K-point) has been eventually achieved with included neighbors of up to the fifth level. The fifth level contains 24 neighbors of each atom, as there are 3, 6, 3, 6, and 6 symmetrically positioned first to fifth neighbors, respectively, resulting in fifteen independent variational parameters f_i.

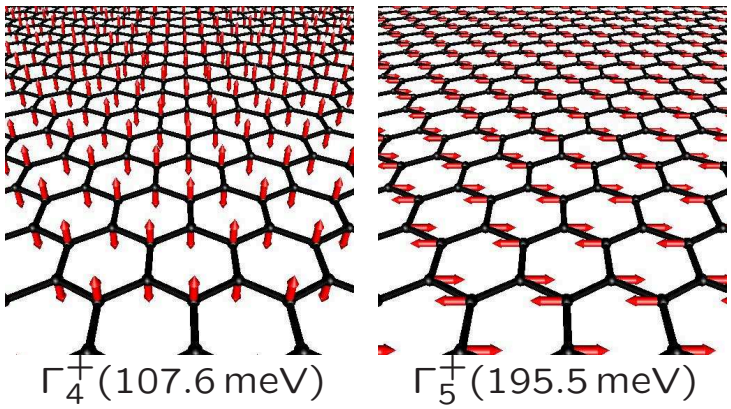

Figure 3.14.: Optical eigenmodes of graphene at the Γ point from the force-constants calculation. The experimental frequency values are given in brackets; they are taken from the data recorded closest to the Γ point.

Force-constants results

The optimized values of the force constants parameters are presented in Table 3.2. In Fig. 3.10 we show the phonon dispersion obtained from these force constants in comparison to the experimental data. The largest deviations between the calculation and the experiment occur for the optical phonon branches near the K point. This is due to the strong interaction of the near-K-point phonons with electrons near the Fermi level, which is not included in a force-constants model. Including more than 4th-nearest neighbors of atoms, however, gives a fairly good description of the local minimum of the TO-derived branch at the K point.

Moreover, although FC calculations including only fourth-nearest neighbors provide a considerably good average fit to the experimental data, they lead to permuted frequencies of the LO and LA-derived phonons at the M point (M_1^+ and M_4^-), and to a crossing of the LA and LO branches within the $K-M$ region ($K_5-M_1^+$ and $K_5-M_4^-$) [43]. Therefore, at least fifth-nearest neighbors are required for a good empirical description of the graphite phonon dispersion.

The eigenvectors of all optical phonons from our force-constants calculation at the high-symmetry points Γ, K, and M are drawn in Figs. 3.14, 3.15, and 3.16, respectively. They are in agreement with calculations from a molecular-based approach of Ref. 62. For the degenerate modes, we show only one choice per energy; the remaining eigenvectors can be obtained by the symmetry-group projectors.

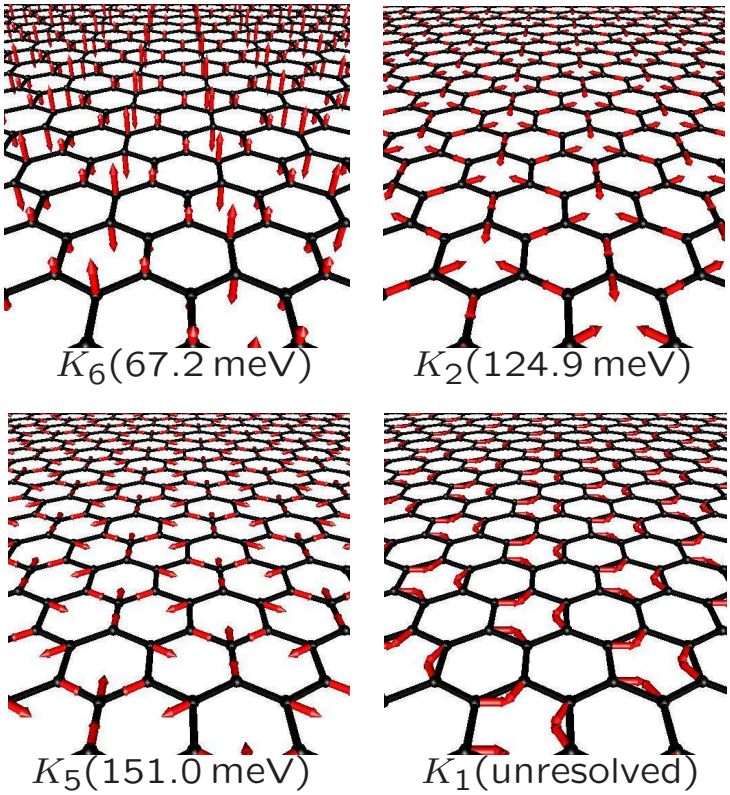

Figure 3.15.: Eigenmodes of graphene at the K point. For the degenerate modes, only one choice per energy is given. Phonon energies given in brackets are the IXS experimental values. For the symmetry notation see Table 3.1.

Table 3.2.: Force constants parameters for graphene, obtained from a fit to the experimental data, in eV/Å^2.

Neighbor level	Stretching	Out of plane	In plane
1	25.880	6.183	8.420
2	4.037	-0.492	-3.044
3	-3.016	0.516	3.948
4	0.564	-0.521	0.129
5	1.035	0.110	0.166

Often he molecular notation for the symmetry groups is used in the literature. Therefore, Table 3.1 shows the relation between the spacegroup notation of P6$_3$/mmc and the molecular notation at the high-symmetry points Γ, K, and M, and the lines $\Gamma - K - M$ (T) and $\Gamma - M$ (Σ). The eigenvectors will help to choose the sample orientation in future IXS experiments. The scattering cross section is zero if the direction of the atomic displacements and the momentum transfer in the scattering process enclose an angle of 90°.

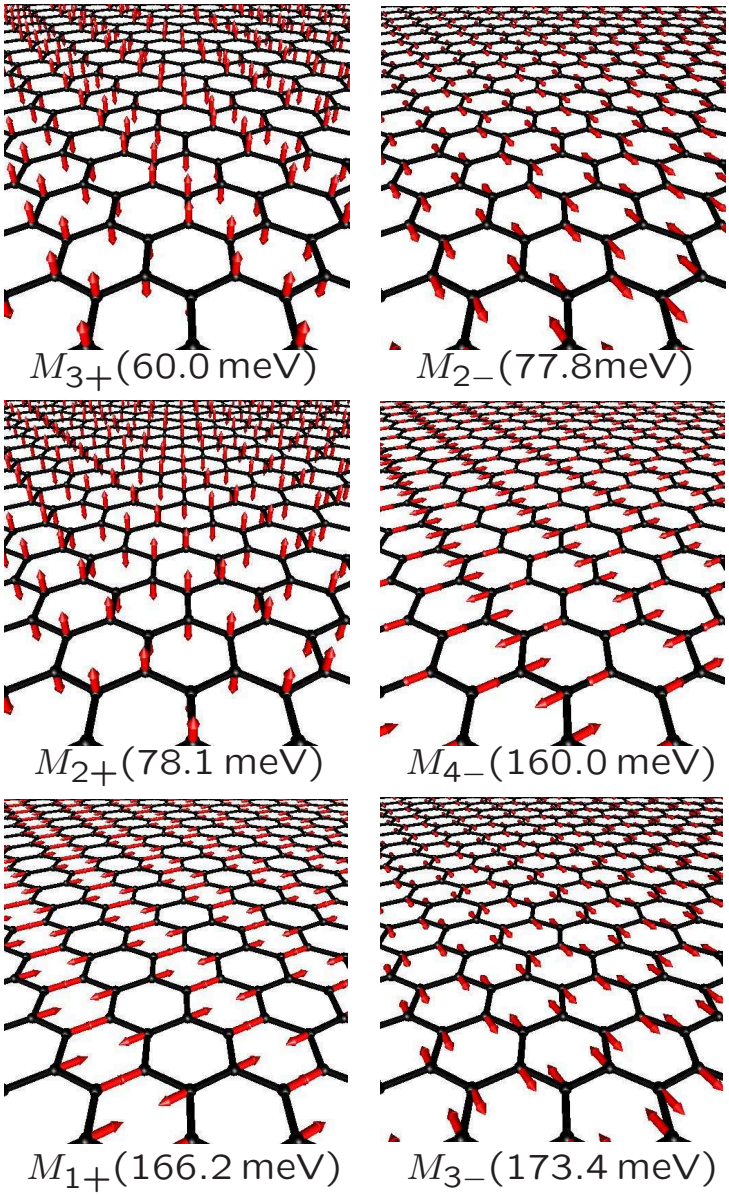

Figure 3.16: Eigenmodes of graphene at the M point (from lower to higher frequencies). Phonon energies given in brackets are the IXS experimental values. For the symmetry notation see Table 3.1.

3.3. Electron-phonon interaction

Electron phonon interaction gives the main contribution to the phonon interaction with the electronic system. Due to the specific point-like Fermi surface graphite is particulary interesting. In graphene (also in metallic carbon nanotubes) the electron-phonon interaction strongly softens phonon frequencies. This gives rise to Kohn anomalies which occur for phonons having a wavevector $\mathbf{q}$ such that there are two electronic states $\mathbf{k_1}$ and $\mathbf{k_2} = \mathbf{k_1} + \mathbf{q}$ near the Fermi surface. The lattice vibrations then are partly screened by conduction electrons. In metals a Kohn anomaly is manifested as fast changes in the phonon dispersion relation that occurs at certain points in the Brillouin zone, produced by the abrupt change in the screening of lattice vibrations by conduction electrons [63]. In graphene, the electronic gap vanishes only at the two equivalent K points which are connected by the vector K. Thus, Kohn anomalies can occur for $\mathbf{q} = \Gamma$ or $\mathbf{q} = K$.

We perform a symmetry based analysis of the electron-phonon interaction in graphene (see also [64]). An electronic state that transforms like the irreducible representation $D^{(\mu)}$ can only couple to those phonons of which the irreducible representation is contained in the symmetrized square of $D^{(\mu)}$. It turns out that only a few vibrational modes, *i. e.*, Γ_5^+, K_1 and K_5 can couple to the electronic system. For these and all other optical modes at the Γ, K and M-points we know the displacement pattern (see Figs. 3.14, 3.15 and 3.16). These displacements $\mathbf{u}$ are added to the position of the relaxed coordinates in the range of [-0.03 Å, 0.03 Å]. This is like the frozen-phonon technique described in section 2.1.5 and allows for the calculation of phonon frequencies from the total energy. We also analyze other energy contributions, the ionic repulsion energy, the electronic energy, and the Fermi level in order to find indications of the Kohn anomaly. All energy contributions are calculated from density functional ground state calculations.

3.3.1. Details of the calculation

Most density functional theory calculations need periodic boundary conditions. In other words the simulation is done with an infinite 3D crystal. For graphene we use the unit cell shown in Fig. 3.1. The lattice vectors are $\vec{a_1} = a_0 \cdot (\sqrt{3}/2, -1/2, 0)^T$ and $\vec{a_2} = a_0 \cdot (\sqrt{3}/2, 1/2, 0)^T$. Graphene has a lattice constant of a_0=2.463 Å. Carbon atoms are at the positions $(1/3, 1/3, 0)$ and $(2/3, 2/3, 0)$ (in lattice vectors). The carbon-carbon atomic distance is $a_{cc}=1/\sqrt{3} \cdot a_0 = 1.422$ Å. The third lattice vector $\vec{a_3}$ points into the direction $\vec{a_1} \times \vec{a_2}$. The length of $\vec{a_3}$ is set to a value of 10 Å, almost three times larger than the inter-layer distance in graphene. This provides a value large enough to prevent overlap between the layers.* For the same reason there is no need for a k-point sampling perpendicular to layers, as there are no Bloch waves along these direction. In the plane 30×30 k-points were used.

*If a smaller value has to be chosen, one can check effects of overlap in the band structure perpendicular to the layers. Ideally, the bands should be totally flat in the direction perpendicular to the layer.

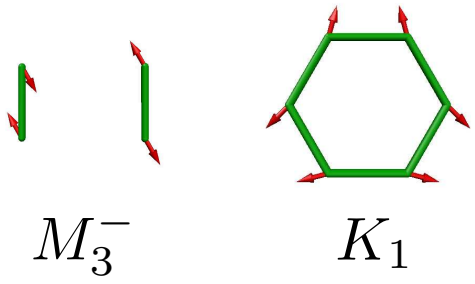

Figure 3.17: Displacement patterns and unit cell used for the two highest-energy phonon modes at the M and K-point, respectively.

3.3.2. Results

In Fig. 3.18(a) we plot the Fermi-level shift as function of displacement $\mathbf{u}$.

The modes that have a Kohn anomaly, Γ_5^+ and K_1, show the strongest shift. The mode M_3^-, which cannot couple to the electronic system shows almost zero shift. The mode K_5, which can couple to the electronic system shows a shift, but smaller in magnitude than the two Kohn modes.

Next we analyze the electronic energy: it is defined as the integral of all occupied states over the entire Brillouin zone relative to the Fermi level. Technically we summed over all eigenstates at each k-point, in this case a 30×30-mesh. One has to take care of the weight of the k-point $w(k)$. The weight $w(k)$ is proportional to the number of equivalent k-points. Here we shifted the k-grid in order to obtain an equal weight for each k-point. The electronic energy was divided by the number of atoms in the unit cell and shifted to zero at zero displacement. The results can be seen in Fig. 3.18(b). Those modes that show no Kohn anomaly show a perfect quadratic behaviour. The modes connected to the Kohn anomaly show jitter. This non-monotonic behaviour is an indication of a Kohn anomaly.

Comparing the energy contribution from the ion-ion repulsion in Fig. 3.19 (a) we find a perfect quadratic behaviour for all modes. It is interesting to note that the decrease of ion-ion repulsion is balanced by the strong increase in electronic energy for K_5. But adding both energy contributions still leads to a downward openened parabola, indicating that the stability of this mode does not stem from the electronic contribution alone. Plotting the total energy in Fig. 3.19(b) we find all modes stable. From the curvature of this function the phonon frequency can be calculated (see section 2.1.5). The resulting frequencies are in good agreement with those from the force-constants calculation from Fig. 3.10.

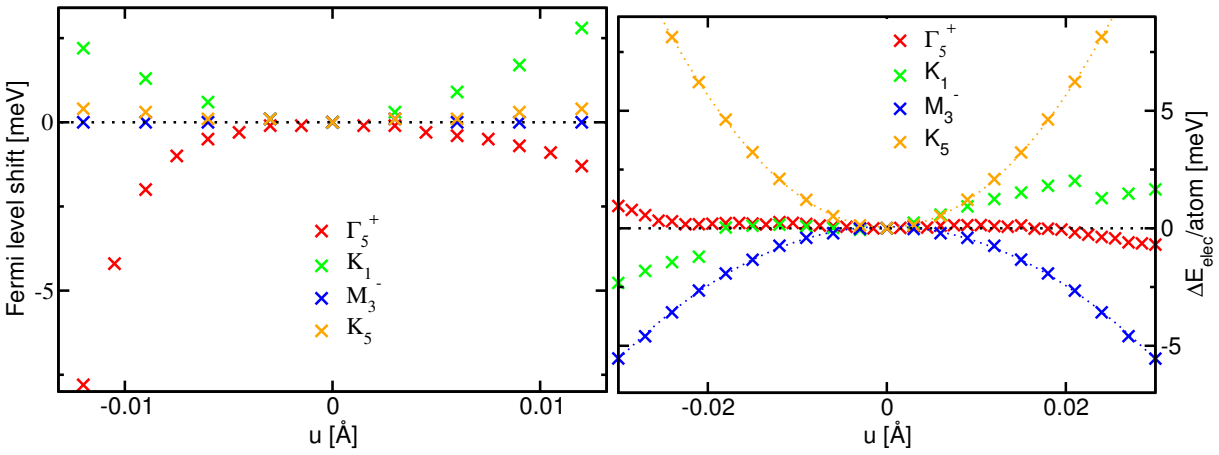

(a) Fermi level **(b)** Change in electronic energy

Figure 3.18.: (a) Fermi level and (b) electronic energy as a function of the displacement u for various optical phonons at high-symmetry points in graphene. The Fermi level is affected strongest for the Kohn modes Γ_5^+ and K_1. In contrast, the electronic energy only shows little changes for the Kohn modes, but some irregularities.

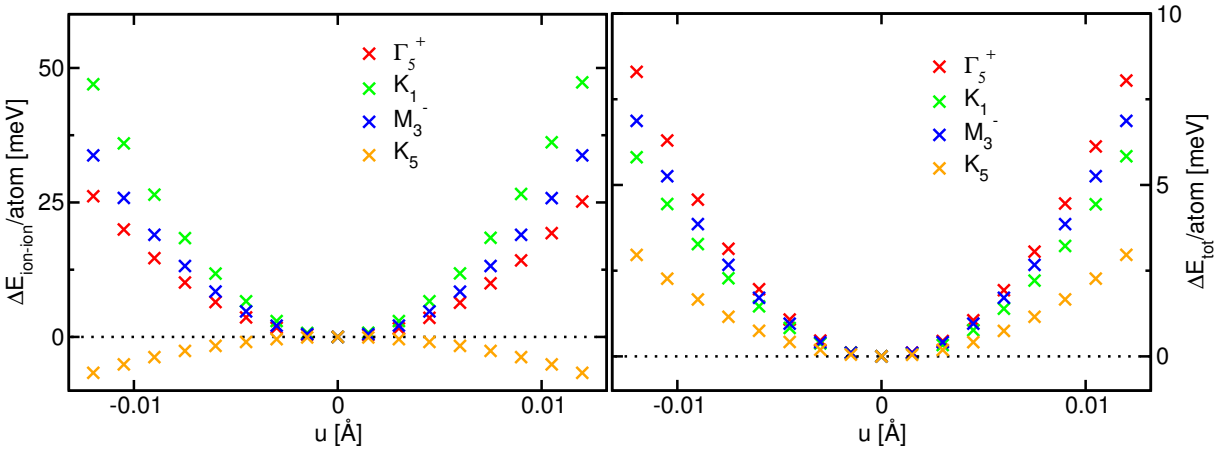

(a) Ion-ion repulsion energy **(b)** Total energy

Figure 3.19.: (a) Ion-ion repulsion energy and (b) total energy as a function of the displacement u for various optical phonons at high-symmetry points in graphene. From the curvature in (b) the phonon's frequency can be calculated.

3.4. Graphene under strain

The extra-ordinary electronic properties of graphene make it a candidate to serve as building block for micro-electronics. For this, the graphene sheets have to be grown on an insulating material, such as SiO_2, which have in general a different lattice constant. This introduces strain, so the changes in the electronic properties under the effect of strain are of fundamental importance. On the other hand, strain opens possibilities to manipulate the electronic system, often referred to as band-gap engineering.

The mechanical behaviour of graphene is governed by the interatomic bonds. Under the influence of tension or compression the strength of the bonds is altered, which is reflected in a variation of the phonon frequency. In this way, measuring these frequencies gives a good estimate of the magnitude of the strain. Measuring the topography of phonon frequencies can give information on local strain distributions.

Uniaxial strain reduces the hexagonal symmetry of the hexagonal lattice. Symmetry-breakings usually lead to new and interesting physics, *e.g.* , splitting of degenerate energy levels in a magnetic field.

In this section the electronic and vibrational band structure of strained graphene is analyzed from a theoretical point of view. I investigate the effect of small uniaxial strains along arbitrary directions.

Convergence study

In Fig. 3.20 we plot the calculated phonon dispersion[†] obtained with different sets of parameters. The strongest discrepancies are found for the TO-derived branch near the K-point. In order to describe the TO-branch around the K-point correctly the dynamical matrix at the K-point should explicitly be included. This is achieved by calculating the dynamical matrices on a $n \times n \times 1$ Monkhorst-Pack grid, where n is divisible by 3 [40,68]. If this is not considered, errors are introduced: for the two examples (10×10 and 11×11) deviations of up to 75 cm^{-1} are found near the K-point. As tradeoff between computing time and accuracy I took the value of

[†]Calculations were performed with the code Quantum-Espresso [65]. We used a plane-wave basis set, RRKJ pseudopotentials [66] and the generalized gradient approximation in the Perdew, Burke and Ernzerhof parameterization for the exchange-correlation functional [8]. A Methfessel-Paxton broadening with a width of 0.02 Ry was used [67]. We carefully checked the convergence in the energy differences between different configurations and the phonon frequencies with respect to the wave function cutoff, the charge density cutoff, the k-point sampling of the Brillouin zone, the number of q-points for calculating the dynamical matrix and the interlayer vacuum spacing for graphene (see Fig. 3.20). Energy differences are converged within 5 meV/atom or better, and phonon frequencies from the whole Brillouin zone within 5 cm^{-1}. The valence electrons were expanded in a plane wave basis with an energy cutoff of 60 Ry. A $42 \times 42 \times 1$ sampling grid was used for the integration over the Brillouin zone. The dynamical matrices were calculated on a $12 \times 12 \times 1$ q-grid using the implemented linear-response theory. Force constants were obtained via a Fourier transformation and interpolated to obtain phonons at arbitrary points in the Brillouin zone. All frequencies were multiplied by a constant factor to match the experimental Raman frequency of graphene.

a 12×12 q-grid. What can nicely be seen is that for the 30×30 k-point mesh, the description at the Γ-point is slightly too soft.

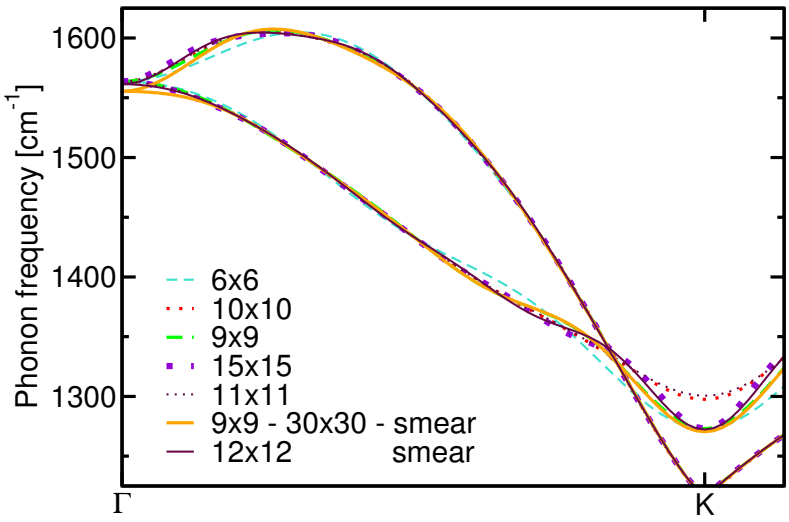

Figure 3.20.: Convergence study of the computational parameters w.r.t. the phonon dispersion. The first row in the label states the q-grid, the second the number of k-points used, if not specified a 42×42 k-grid is used. Label 'smear' states that a broadening was used. Calculating the dynamical matrix on a 10×10 or 11×11 q-grid gives large deviations at the K-point, here a number divisble by three is needed for a good description. If only a 30×30 k-grid is used, the frequencies at the Γ-point are too low. The 12×12 q-grid with smearing was chosen as a reasonable compromise between time and accuracy.

Implementation of strain

The general 3-dimensional Hooke's law connects the stress tensor $\boldsymbol{\sigma}$ and the strain tensor $\boldsymbol{\epsilon}$ via the stiffness tensor $\boldsymbol{c}$: $\sigma_{ij} = c_{ijkl} \cdot \epsilon_{kl}$. As we are only interested in planar strain, the tensile strain along the x-axis can be expressed *via* the two-dimensional strain tensor $\boldsymbol{\epsilon} = ((\epsilon, 0), (0, -\epsilon\nu))$, where ν is the Poisson's ratio. Since we want to apply arbitrary strain directions the strain tensor has to be rotated $\boldsymbol{\epsilon}' = \boldsymbol{R}^{-1}\boldsymbol{\epsilon}\boldsymbol{R}$, where $\boldsymbol{R}$ is the rotational matrix. Here the x-axis corresponds to the zigzag direction of graphene. After applying a finite amount of strain we relax the coordinates of the basis atoms until forces are below 0.001 Ry/a.u. and minimize the total energy with respect to the Poisson's ratio ν. For small strain values we obtain a Poisson's ratio ν=0.164, in excellent agreement with experimental tension measurements on pyrolytic graphite that yield a value of ν=0.163 [69]. Strain reduces the symmetry of the hexagonal system. For strain in arbitrary directions the point group is reduced from D_{6h} to C_{2h}, only the C_2 rotation (rotation by 180°) and the inversion are retained (and the trivial mirror plane). For strain along the 0°or 30°directions additionally mirror planes remain, resulting in D_{2d}-symmetry. A sketch of the hexagonal lattice and the corresponding strain in real space can be seen in Fig. 3.21(a).

Due to the hexagonal symmetry only strain in the range between ϑ=0°and 30°are physically interesting.

In Fig. 3.21 (b) and (c) the resulting Brillouin zones for strain in the directions 0°and 20° are shown. For clarity we have used an exaggerated strain of $\epsilon = 0.3$. Like in unstrained graphene, the six corner points of the Brillouin zone correspond to the K-points. In the unstrained lattice these K-points can be expressed *via* the reciprocal lattice vectors $\mathbf{b}_i$, e.g., $K_1 = 1/3\boldsymbol{b_1} + 2/3\boldsymbol{b_2}$. The same definition is not valid anymore for the strained lattice. Now the K-points have to be obtained by constructing the perpendicular bisectors to all neighboring lattice points and determine their intersection point. In other words the Wigner-Seitz cell of the reciprocal lattice has to be constructed.

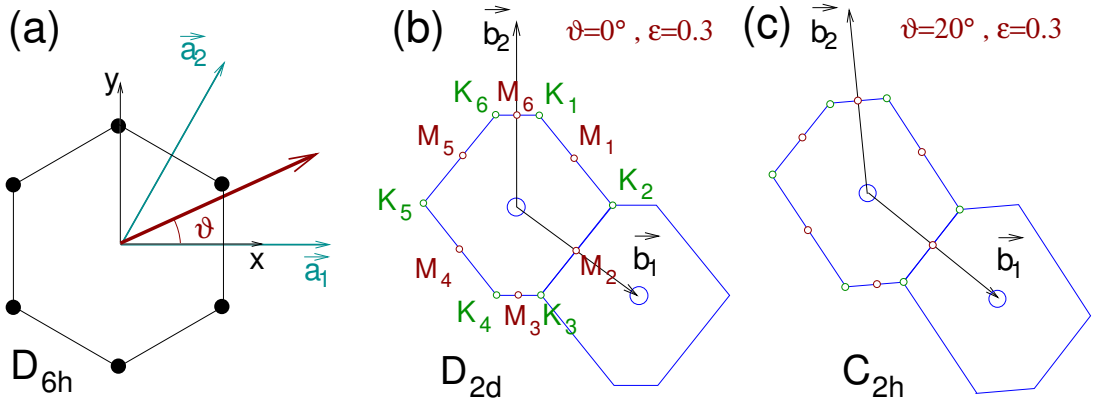

Figure 3.21.: (a) The unit cell vectors $\vec{a_1}, \vec{a_2}$ of hexagonal graphene. The arrow indicates the direction of the applied strain. $\vartheta = 0°$always corresponds to the zigzag direction. (b) Brillouin zone of uniaxially strained graphene in the direction $\vartheta = 0°$. The point group reduces to D_{2d}. $\vec{b_1}, \vec{b_2}$ are the reciprocal lattice vectors. (c) Brillouin zone of uniaxially strained graphene in the direction $\vartheta = 20°$. The point group reduces to C_{2h}.

3.4.1. Changes in the electronic spectrum

The effect of uniaxial strain on the electronic properties has been studied in the literature [70–72]. The question as to whether a gap opens for small strains has remained under considerable controversy [70, 72, 73]. Up to now, there is no comprehensive study on the level of density-functional theory in the literature to address this issue.

The usual way to plot band structures is along the high symmetry directions. For unstrained graphene this corresponds to $\Gamma - K - M - \Gamma$. In strained graphene, as the 6-fold symmetry is broken these lines are not sufficient to cover all high-symmetry lines. For strain in the $\vartheta = 0\,°$direction we choose the lines $\Gamma - K_2 - M_2 - \Gamma$ and $\Gamma - K_3 - M_3 - \Gamma$, the remaining ones are equivalent. In Fig. 3.22 we plot the electronic band structure of 2% strained and unstrained graphene. The most obvious changes in the electronic band structure include an

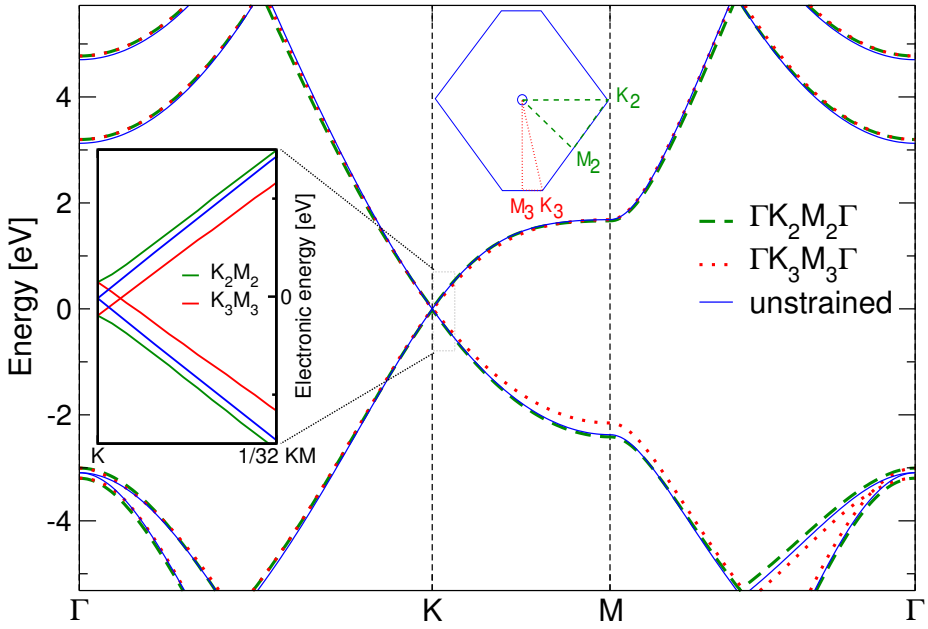

Figure 3.22.: The electronic band structure of unstrained and $\epsilon = 0.02$-strained graphene along the $\vartheta = 0°$-direction. The corresponding paths in the Brillouin zone are indicated. A closeup along KM is shown in the inset.

increase in energy of the π-type valence bands along the $K - M$ direction. The splitting of the σ-type valence bands at $E = -3\,\mathrm{eV}$ can clearly be seen. A closeup of the vicinity of the K-point reveals that the crossing of the Fermi level only takes place between K_3 and M_3. Along $\Gamma - K_2 - M_2 - \Gamma$ there is no crossing of the bands. To further investigate the position of the Fermi crossing we evaluate the direct optical transition (DOT) energy of the π-π^* -bands in the vicinity of the K_1-point. In Fig. 3.23 we show energy contour plots of the DOT energy of the π-π^* -bands. Each plot is centered at its respective K_1-point. The dimension of the sides of the square is $0.02\,\pi/a_0$, where a_0 is the lattice constant . We show an unstrained and a 2%-strained configuration for $\vartheta = 0°$ and $20°$. Although our plots show only the vicinity of the K_1 point, the remaining plots can easily be constructed. Three of the six K-points are equivalent: This can be seen by apparent simple arguments: an arbitrary K-point, K_i corresponds to a set of different of K-points in the adjacent Brillouin zones (K_{i+2}, K_{i+4}) . The equivalence to the remaining three K-points follows by the C_2 rotation (or inversion), where K_i maps to K_{i+3}. Thus the contour plots of K_i i=1,3,5 are identical, the remaining contour plots K_i i=2,4,6 are found by inversion.

As can be seen, for the unstrained configuration the Dirac cones coincide with the K-point.

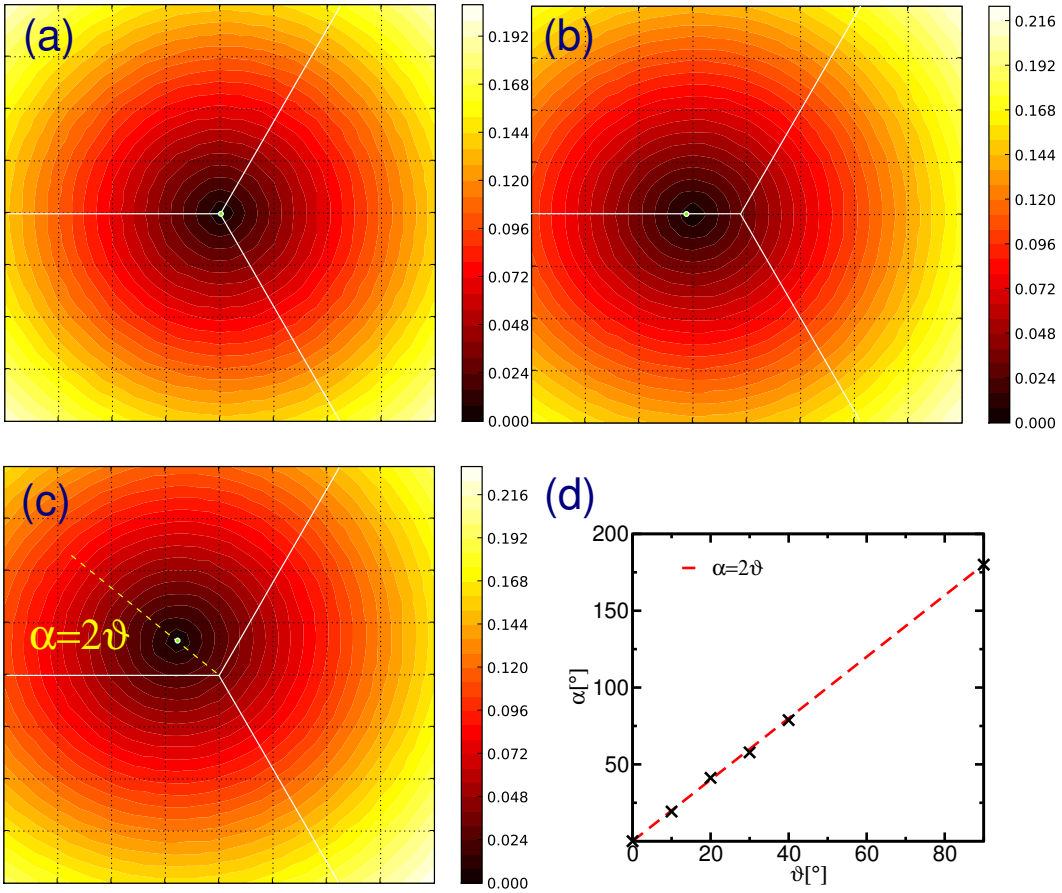

Figure 3.23.: (a)-(c) Contour plots of the direct optical transition energy of the π-π^* -bands. The energy is given in eV. Each plot is centered at its respective K-point. The length of each side is $0.02\pi/a$. Shown here is the plot around K_1. Plots around K_i (i=3,5) are identical. K_i (i=2,4,6) can be found by inversion. (a) Unstrained configuration, (b) 2%-strained configuration for $\vartheta = 0\,^\circ$ and (c) 2%-strained configuration for $\vartheta = 20\,^\circ$. (d) Numerically obtained angle α as a function of the direction of strain ϑ. The line shows the function $\alpha = 2\vartheta$.

For the strained configuration at $\vartheta = 0°$ the crossing moves along the $K_3 - M_3$-line. Now the origin of the bands in Fig. 3.22(a) becomes clear: the line along $K_2 - M_2$ cuts the Dirac cones away from the center, resulting in a small opening of the bands.

For the strained configuration at $\vartheta = 20\,^\circ$ shown in Fig. 3.23(c) the Fermi crossing moves away from the zone-edge into the Brillouin zone. The question of whether or not a gap opens in graphene under small strains must be answered by looking into the appropriate direction in reciprocal space. The tips of the Dirac cones, according to our DFT calculations, lie on lines through K that enclose an angle of $\alpha = 2\vartheta$ with the $K - M$ line [see Fig. 3.23(c)]. Looking at the band structure along the strained high-symmetry directions, in contrast, corresponds to cuts of the Dirac cones not centered at the Fermi level crossing, seemingly suggesting an energy gap. This becomes important for strain in directions other than $\vartheta = 0°$ and $\vartheta = 30°$, when the

Fermi level crossing does not coincide with the Brillouin zone edges.

In summary, depending on the direction and amount of strain, the Fermi crossing moves away from the K-point. Graphene remains semimetallic under small strains. The deformation of the cones gives different Fermi velocities parallel and perpendicular to the strain [74], which may lead to anisotropic resistance found recently in experiments [75].

3.4.2. Changes of the vibrational properties

Recently, uniaxially strained graphene was investigated by Raman spectroscopy [70,76,77]. The magnitude of strain could be determined from the shift of the Raman-active modes. In addition, the crystallographic orientation of the graphene sample could be determined by polarized Raman measurements [76,77].

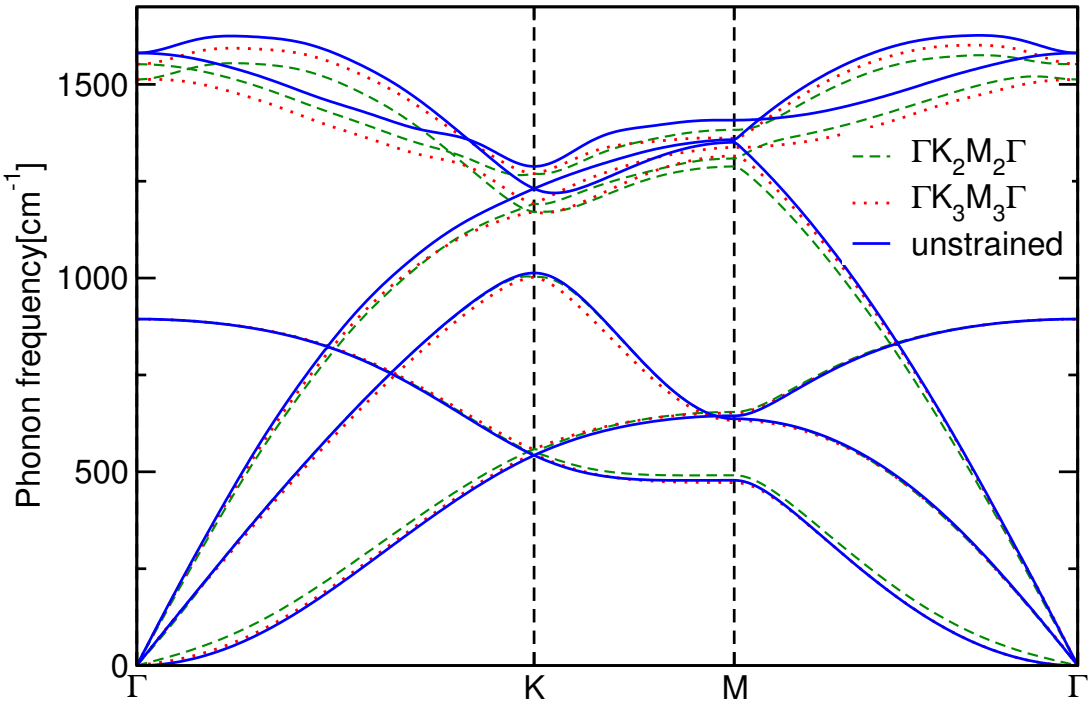

Figure 3.24.: The phonon dispersion curves of unstrained and $\epsilon = 0.02$-strained graphene along the $\vartheta = 0°$-direction. The paths in the Brillouin zone are the same as in Fig. 3.22. The path within the Brillouin zone is shown in the inset of Fig. 3.22.

Theoretically, the effects of uniaxial strain on the vibrational properties have been investigated *via ab-initio*-calculations only for very large strains on the order of 40 % and only for armchair and zigzag directions [78]. In contrast, the maximum strain realized experimentally has been a few percent [70, 72, 73]. For realistic strain values or for strain in arbitrary directions, a comprehensive study is missing.

Table 3.3.: Shift rates for the G^+ and the G^- modes in strained graphene (in $\mathrm{cm}^{-1}/\%$ strain).

	Ref.76	Ref.77	exp.	theory
G^+	-5.6	-18.6	-16.1	-15.2
G^-	-12.5	-36.4	-35.2	-33.7

Phonon dispersion under strain In Fig. 3.24 we show the phonon dispersion along the lines $\Gamma - K_2 - M_2 - \Gamma$ and $\Gamma - K_3 - M_3 - \Gamma$ for a strain of $\epsilon = 0.02$ in the $\vartheta = 0\,^\circ$direction. The vibrational bands show the general trend of softening under strain. Except the lowest-energy acoustic mode hardens. This mode, which shows a quadratic dependence for $q \to 0$ for unstrained graphene, is an out-of-plane mode and therefore referred to as ZA-mode [68]. The hardening only occurs along the the $\Gamma - K_2$ direction. Also the quadratic dependence for $q \to 0$ changes into a linear dependence. This line describes propagating waves along the direction of the applied strain. Thus the hardening can be compared to the frequency increase when tension is applied to a string.

Evolution of the G-band under strain The G-band stems from the E_{2g}-mode at the Γ-point. Its frequency is at 1581 cm^{-1} and it is two-fold degenerate for unstrained graphene. Uniaxial strain reduces the hexagonal symmetry of the system and leads to a lifted degeneracy under strain. In this way the crystallographic orientation of graphene can be determined from the polarization dependence of the split G-band [76, 77].

As shown in Fig 3.25 the E_{2g}-mode of strained graphene splits into two distinct modes. These two modes possess eigenvectors parallel and perpendicular to the strain direction (see right side of Fig. 3.25). The mode parallel (perpendicular) to the strain direction undergoes a larger (smaller) redshift and is therefore entitled G^- (G^+).

The strain rate of the G^- (G^+) -mode is independent on the direction of strain. This result stems from the isotropy of the hexagonal lattice. The strain rates are perfectly linear, a fact that is important for the determination of strain in experiment.

In Table 3.3 we show a summary of the determined shift rates for the G^+ and G^--modes.[‡]. I have calculated shifts for small strain values up to 4 %. In experiments, compressive strain leads to saturation effects at $\approx 0.7\%$, most probably due to a buckling of the graphene sheet [79]. From polarized Raman measurements of the G^+ or G^- the crystallographic orientation with respect to the strain direction of the Graphene flakes can be determined [76, 77].

3.4.3. Evolution of the $2D$-mode under strain

The $2D$-mode is the strongest feature in a Raman spectrum of graphene (see Fig. 3.5 for a Raman spectrum of graphene). This mode is energy-dependent and double-resonant [80, 81]. Because of the doping dependence of the G-band-frequency [82] and the higher shift rate of the $2D$-mode

[‡]The experiments were performed by Otokar Frank, University of Patras, Greece

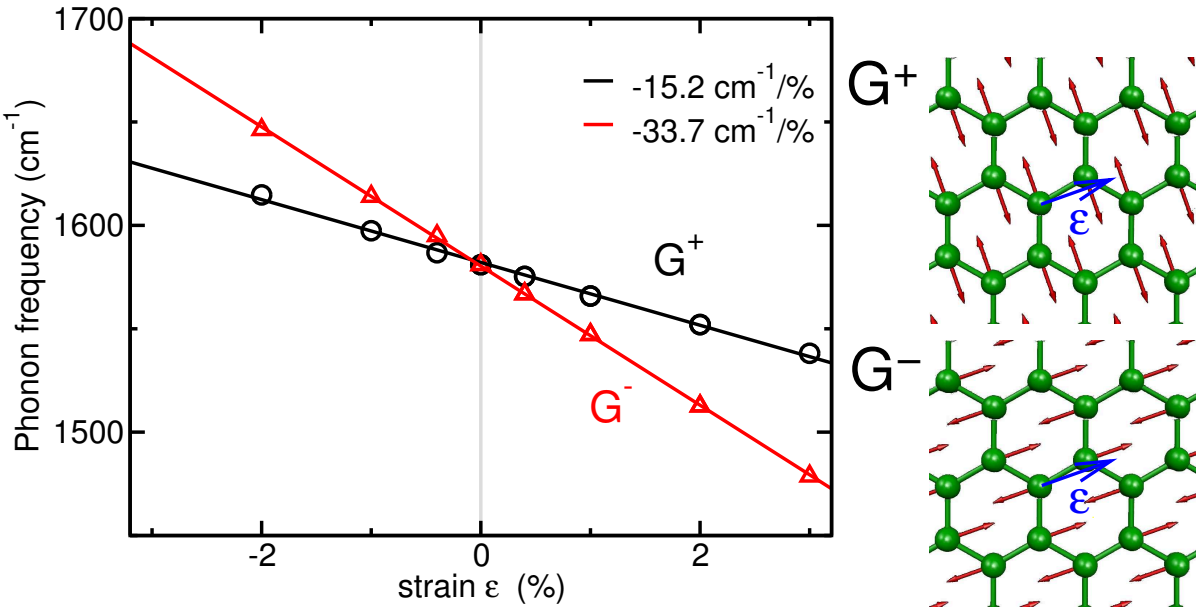

Figure 3.25.: (left) Frequency of the split E_{2g} mode in uniaxial strained graphene calculated from ab-initio methods. (right) Displacement patterns for the G^+ and G^- modes. Here the strain is applied in direction $\vartheta = 20°$.

the latter is more commonly used to quantify strain in graphene. The shift of the $2D$-mode under strain is currently under discussion and usually only single values are given [76, 77, 79]. However, recent experiments show that the shift of the $2D$-mode in addition depends on the crystallographic orientation and the polarization of the incident and outgoing light during the Raman experiments (see Fig. 3.26) Furthermore at least two contributions of the $2D$-mode can be seen in the right section of Fig. 3.26.[§]

To understand these results a comprehensive theoretical description is needed to quantify the shift of the $2D$-mode under strain that also consideres the polarization of the incident light and the crystallographic orientation of the sample.

The mechanism of a double-resonance process (DR-) as currently established in the literature for the $2D$-mode is shown in Fig. 3.27 [33, 83, 84]. An electron-hole pair is created by an incoming photon with energy E_l. The electron or hole is scattered inelastically by a phonon with a wavevector $q_1 \neq 0$ into a real state. From there it is scattered back inelastically by another phonon $q_2 = -q_1$ where it recombines with an energy $E = E_l - 2\hbar\omega(q_1)$. The difference to the $2D$-mode is that in D-mode scattering, one inelastic scattering process is replaced by an elastic scattering at a defect. The contributing phonon stems from the fully-symmetric TO-derived branch [68].

The changes of the electronic and vibrational bands under strain both influence the $2D$-mode. Fig. 3.28(a) shows a contour plot of the lowest-energy conduction band and two different

[§]Currently unpublished data from Hugen Yan, Columbia University show similar features.

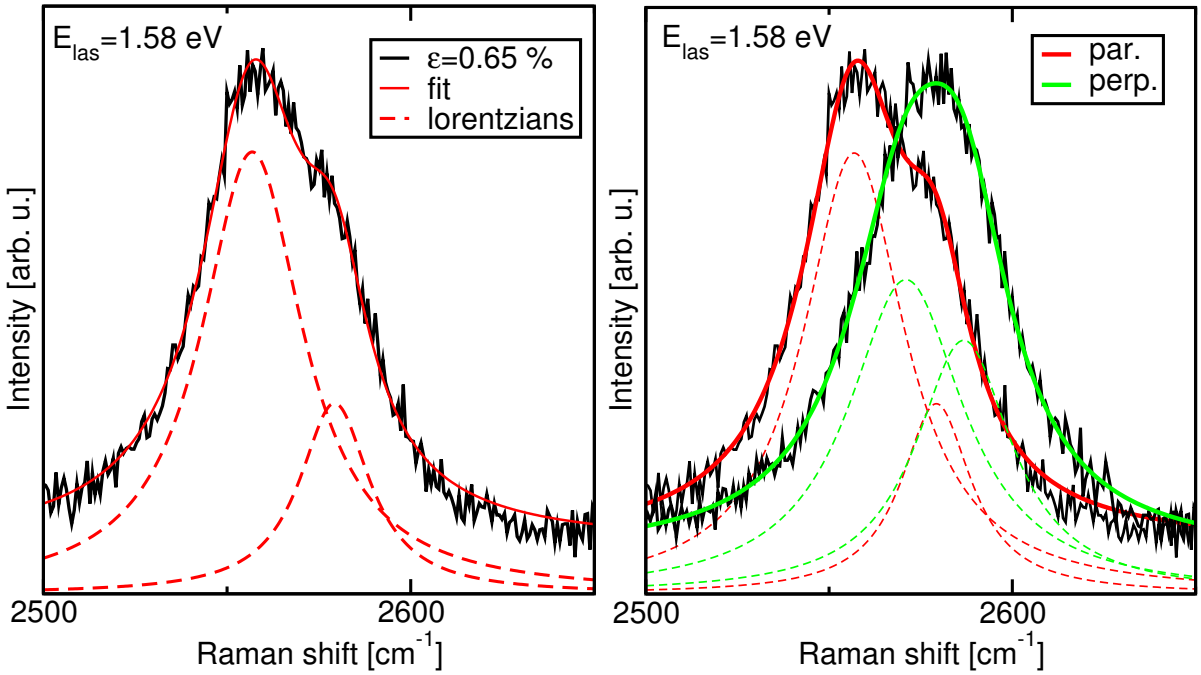

Figure 3.26.: (left) Raman spectrum of uniaxially strained graphene ($\epsilon \approx 0.6\,\%$ and $\vartheta = 17°$) . Contributions from two lorentzians are clearly visible. (right) Raman spectra of uniaxially strained graphene with polarization parallel and perpendicular to the strain direction. (Spectra were recorded by Dr. Otakar Frank, University of Patras, Greece)

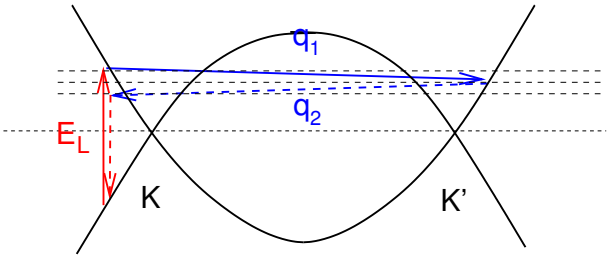

Figure 3.27: Scattering mechanism of the $2D$-mode plotted in the electronic bands of graphene along KMK'. This mechanism is currently established in the literature [33, 83, 84].

$K - K'$ paths for strain in the $\vartheta = 0°$direction. In Fig. 3.28(b) we plot the electronic bands along these two paths. Depending on the wavevector of the electronic transition a different phonon wavevector is doubly resonant enhanced. This leads to differences in phonon energy of up to $10\,\mathrm{cm}^{-1}/\%$ strain and leads to a little broadening of the $2D$ mode under strain [76, 77] but quantitavely is not able to explain the large separation observed in the experiment.

In order to obtain an idea on the scattering processes that contribute to double-resonant Raman scattering in graphene I calculate the Raman spectra for different scattering configurations. I will first use analytical expressions of the electronic and vibrational band structure to calculate the Raman spectra and identify the dominant processes. With this knowledge I will then extract phonon frequencies from density functional theory (DFT) calculations of the strained graphene sheet.

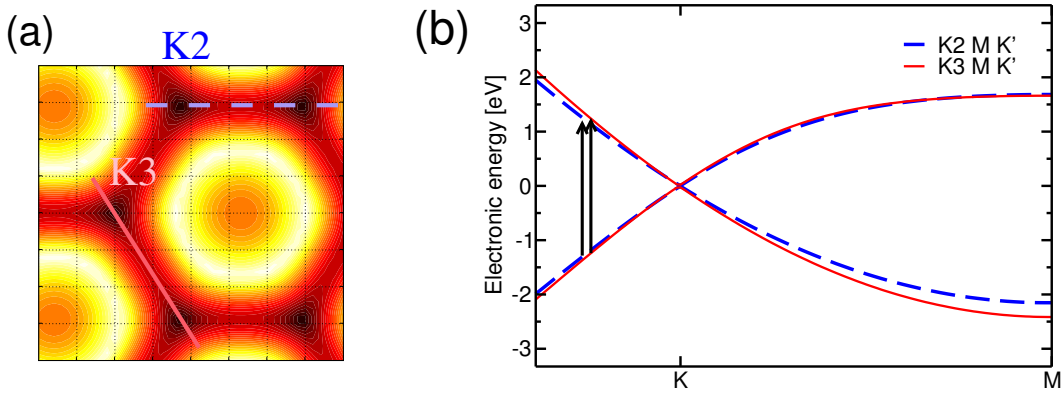

Figure 3.28.: (a) Contour plot of the lowest-energy conduction band. (b) Band structure between K and K' between different K-points. The corresponding paths are shown in (b). Depending on the electronic transition a different wavevector of the scattered phonon becomes resonantly enhanced. This leads to a broadening of $2D$ mode, as contributions from the vicinity of all K-points are added up.

Simulation of the double-resonant Raman modes

In the following we first use analytical expressions of the electronic and vibrational band structure to calculate Raman spectra for different scattering configurations. With these results we identify the dominant processes and motivate their extraction from density functional theory (DFT) calculations under strain. The cross section $K_{2f,10}$ of a resonant Raman process can be calculated by [21, 22]

$$K_{2f,10} = \sum_{a,b,c} \frac{M_{fc}M_{cb}M_{ba}M_{ai}}{(E_l - E_{ai} - i\hbar\gamma)(E_l - \hbar\omega - E_{bi} - i\hbar\gamma)(E_l - \hbar\omega - E_{ci} - i\hbar\gamma)} + \frac{M_{fc}M_{cb}M_{ba}M_{ai}}{(E_l - E_{ai} - i\hbar\gamma)(E_l - E_{bi} - i\hbar\gamma)(E_l - \hbar\omega - E_{ci} - i\hbar\gamma)}. \quad (3.4)$$

This is the formula for the D-mode. The first term denotes incoming resonance, and the second outgoing resonance. E_{xy} is the energy difference between the electronic states x and y. E_l and $E_l - \hbar\omega$ are the energies of the incoming and outgoing photon, respectively. M_{xy} is the matrix element for the scattering over the intermediate states x and y, and γ is the broadening parameter of the electronic transition.

To investigate which processes contribute to the D-mode we evaluate Eq. (3.4). The sum is converted into an integral and the matrix elements are taken constant. The electronic bands are from a tight-banding approach [85], where we use the values $\gamma_0 = 2.8\,\mathrm{eV}$ and $\gamma_0{}' = 0\,\mathrm{eV}$. The TO phonon dispersion around the K-point is taken from the analytical expression derived from recent inelastic X-ray measurements [55].

In a first approximation we integrate along the line that connects two neighboring K-points (see Fig. 3.29(a) for a plot of the two-dimensional band structure of graphene). We have to

take special care in this one-dimensional integration as it leads to erroneous results: in the one-dimensional integrations phonons with $q \approx K$ do not interfere destructively and give a major contribution [81]. Still the one-dimensional integration gives a good idea for identifying the contributing processes. We find contributions from phonons from the $K - M$ and $\Gamma - K$ directions. The cross section $K_{2f,10}$ as a function of phonon frequency is plotted in Fig. 3.29(b). Here, a small broadening parameter of $\gamma = 0.005\,\mathrm{eV}$ was used. The two peaks of each color correspond to incoming and outgoing resonance.

In a second approximation we now look at the integration in two dimensions. The integration areas are highlighted as shaded areas in Fig. 3.29(b), where scattering into all neighboring K-valleys is considered. The integral is evaluated with the Monte-Carlo method with 5×10^6 points. Now, the K-phonon contribution (not shown) cancel out due to destructive interference, in agreement with Ref. 81 . Comparing the result in 3.29(b) with the one-dimensional integration we find similar features. We thus can conclude that phonons from the $K - M$ direction and phonons from the $\Gamma - K$ direction do contribute to the D-mode in graphene. We will refer to them as outer processes (phonons from $K - M$, see Fig. 3.30) and inner processes (phonons from $\Gamma - K$). Using a larger value of $\gamma = 0.05\,\mathrm{eV}$, the distinct features merge and a single broad D-band arises (dotted curve in Fig. 3.29(b))

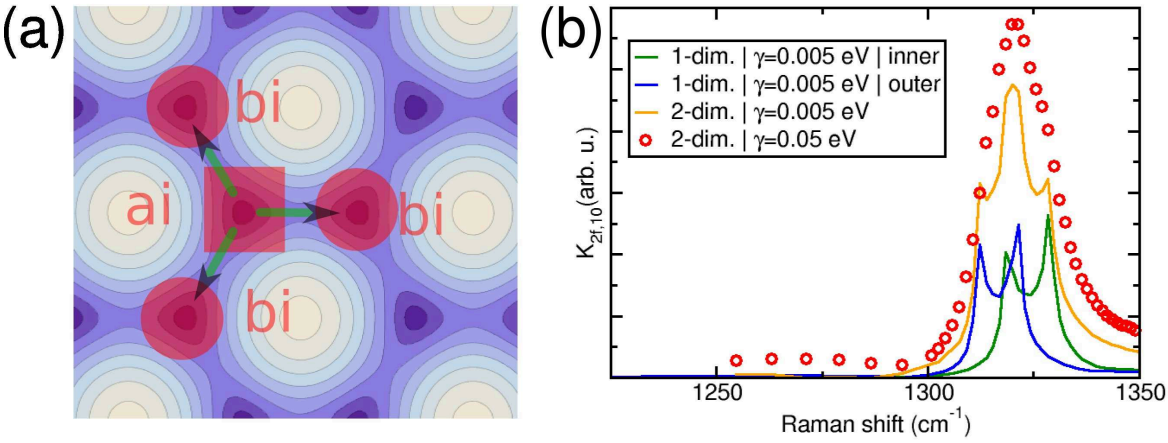

Figure 3.29.: (a) The two-dimensional integration area plotted in the electronic energy contours. The electron absorption happens near "ai" and the electron is scattered to regions near "bi". (b) Raman cross section $K_{2f,10}$ for several different parameter sets. Integration is either performed along lines connecting neighboring K-points (denoted by '1-dim.') or two-dimensional within the highlighted area ('2-dim.'). The similar features in both types of integration verifies that contributions from the inner processes are visible in the two-dimensional integration as well. At higher values of γ, single contributions are not distinguishable and a single D-peak is visible.

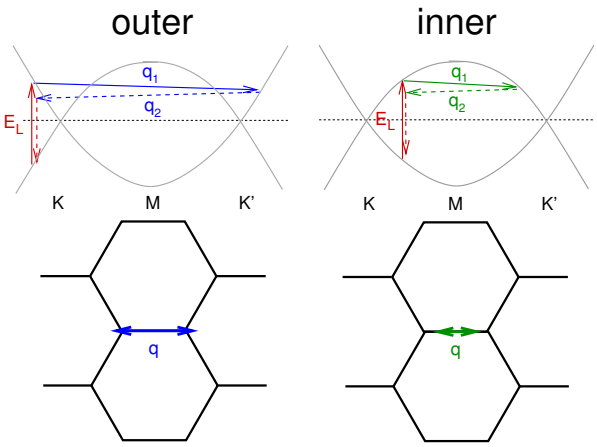

Figure 3.30: Double-resonance mechanism (left: outer process, right: inner process) plotted into the band structure scheme of graphene along KMK'. Below is the mechanism plotted in the Brillouin zone.

Polarization In a perfect graphene flake the D-band does not depend on the polarization of the incident light. The polarization of the incoming laser affects the absorption in k-space. Electrons with a wavevector parallel to the polarization of a photon can not be excited during an absorption process [86]. A way to incorporate this property in the above calculation of the Raman cross section is to leave out areas in the integration process. This is illustrated in 3.31(a) for "vertical" polarization indicated by the arrow $\vec{p}$. As expected, neglecting this area in the integration process has no influence on the D-band for unstrained graphene in 3.31(b). Now we simulate tensile strain, by compressing the band structure in strain-direction. This is indicated in 3.31(a) for strain in the zigzag direction. A strain of 9% was used, which is large compared to experimentally achieved values. This is just a proof of concept, as we have not included the phonon softening, and used the unstrained phonon dispersion. The resulting Raman cross sections are shown in 3.31(b). The labels parallel and perpendicular are w.r.t. the strain direction. Depending on the polarization, the D-band has a different energy shift.

Mapping with atomistic calculation Using DFT calculations of the phonon dispersion and the electronic band structure we now make quantitative predictions on the peak positions of the 2D band for several scattering configurations. The strain (tensile and compressive) is applied in several directions between the zigzag and armchair direction for strain values up to 3 %. The largest differences are found between zigzag and armchair direction. With this data we can perform a mapping of the expected $2D$-band frequencies, using the scattering processes shown in 3.30. The scattering of the electrons is considered to be elastic for identifying the contributing phonon's wavevector (this corresponds to horizontal arrows in Fig. 3.30).

Depending on which direction in reciprocal space the electron is scattered, different resonance conditions apply. This is a consequence of the symmetry-breaking induced by the strain. [87] In addition, as mentioned above, when the light is polarized, some areas in the reciprocal space do not have excited electrons that contribute to the $2D$-band. With this argument the most

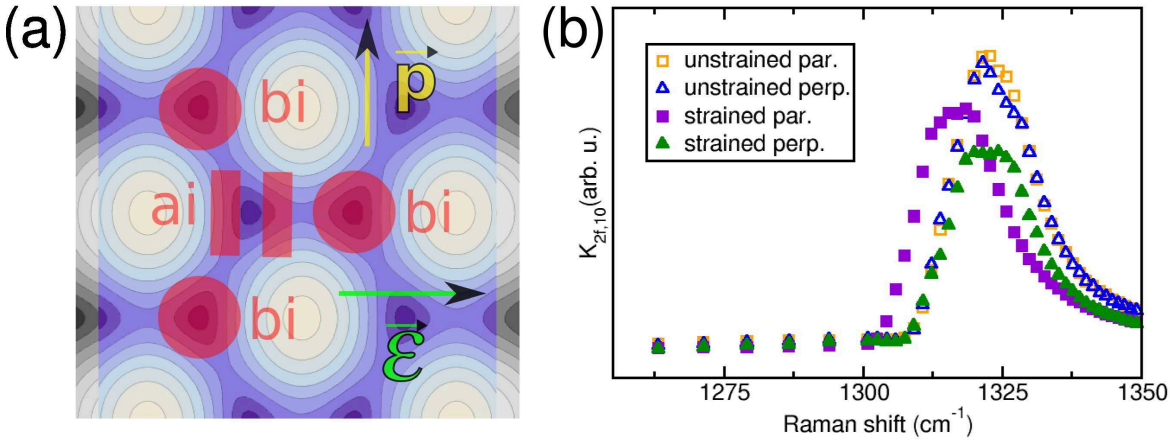

Figure 3.31.: (a) Modelling of strain by compressing the band structure. To account for the anisotropic absorption depending on the polarization, parts of the integration area have been omitted. (b) Raman cross section $K_{2f,10}$ for strained and unstrained graphene with polarization parallel and perpendicular to the strain direction. Only when strain is applied, a polarization dependent shift is observed.

dominant processes are those that are perpendicular to the polarization of the incoming light. The corresponding processes are depicted in 3.33(a). The notation K_1 means along K_1, the K-points are numbered clockwise, beginning with the top right as number 1.

3.32 shows the obtained $2D$ frequencies for inner and outer processes (as shown in 3.30), for strain in armchair and zigzag direction, and for two different laser energies (1.5 eV and 2.4 eV). As can be seen, the splitting is larger for zigzag (ZZ) strain. Also the polarization dependent shift is larger for ZZ strain.

Both, inner and outer processes lead to a polarization dependent splitting. However, the inner processes lead to a larger splitting. In 3.33(b) we show the phonon dispersion along two different paths in the reciprocal space. The TO branch between Γ and K shows a large splitting depending on the chosen path. The softening is stronger in the direction perpendicular to the strain direction. This can be understood looking at the displacement patterns of this mode: the displacement is parallel to the strain direction and the involved atomic bonds are weakened due to the strain. The same argument is responsible for the stronger softening of the G^--mode at the zone-center [76, 77, 87]. Between K and M the displacement patterns of the TO branch are not parallel anymore and have lost their TO character and thus are not so strongly affected by the strain direction.

With the above method of frequency mapping we cannot determine the details of intensity and lineshape of the D and $2D$-bands. Simple arguments like looking at the electronic density of states do not take into account the phonon density of states. Sometimes it is argued that

the outer processes only contribute to the $2D$-mode because of the trigonal warping effect and a higher density of states [83,84]: The trigonal warping effect becomes stronger for larger excitation energies, however for optical transition energies <2 eV the equi-energy contours are still more or less round. In addition, the phonon dispersion of the TO-derived mode near the K-point was a long time believed to show a strong trigonal warping. This was recently resolved by Grüneis *et al.* performing inelastic x-ray experiments revealing almost-round equi-energy phonons of the TO-branch near the K-point [55] with almost no trigonal warping.

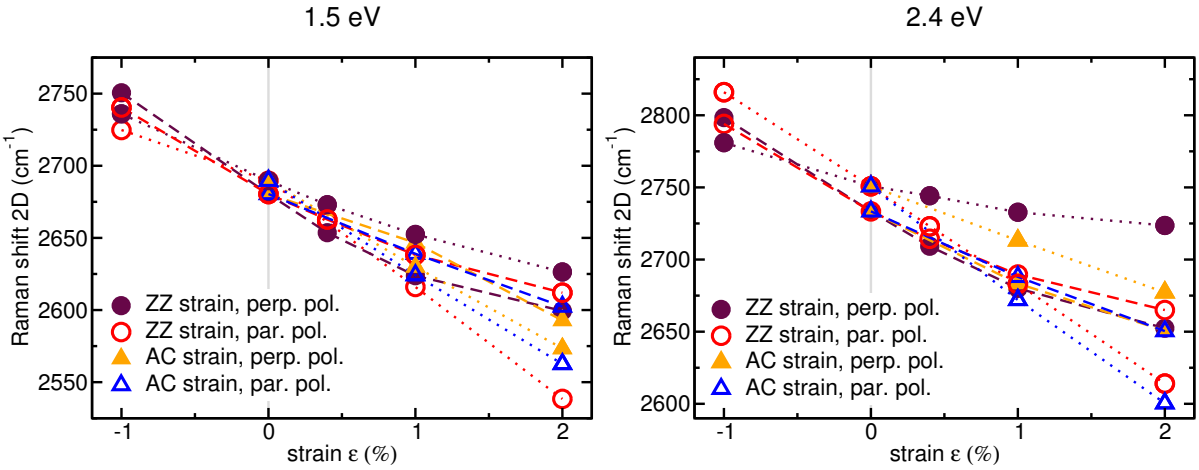

Figure 3.32.: Mapping of the Raman $2D$ contributions for inner and outer processes for the laser energies 1.5 eV and 2.4 eV. Circles (triangles) correspond to strain in zigzag (armchair) directions. Open (closed) symbols denote parallel (perpendicular) polarization w.r.t. the strain direction. The data points are connected with lines that denote inner (dotted) and outer (dashed) processes.

3.4.4. Biaxial strain

Biaxial strain was also applied to the system. In this case, the symmetry is conserved, there is no splitting. For the G-band we obtain a shift rate of 60 cm^{-1}/ %. This is in excellent agreement with the value of 63 cm^{-1}/ % obtained in Ref. [88] . Also a mapping of the $2D$-mode was performed as in the previous section. As in the relaxed case, the splitting is almost not present, and will not be distinguishable in experiments. The result is shown in Fig. 3.34 for the two laser energies of 1.5 eV and 2.4 eV. For the $2D$-band we find a shift rate of 135 cm^{-1}/% for both inner and outer processes for 1.5 eV. For 2.4 eV the shift rates of inner and outer processes do slightly differ: the outer process has a shift rate 135 cm^{-1}/%, while the inner process has a shift rate 124 cm^{-1}/%.

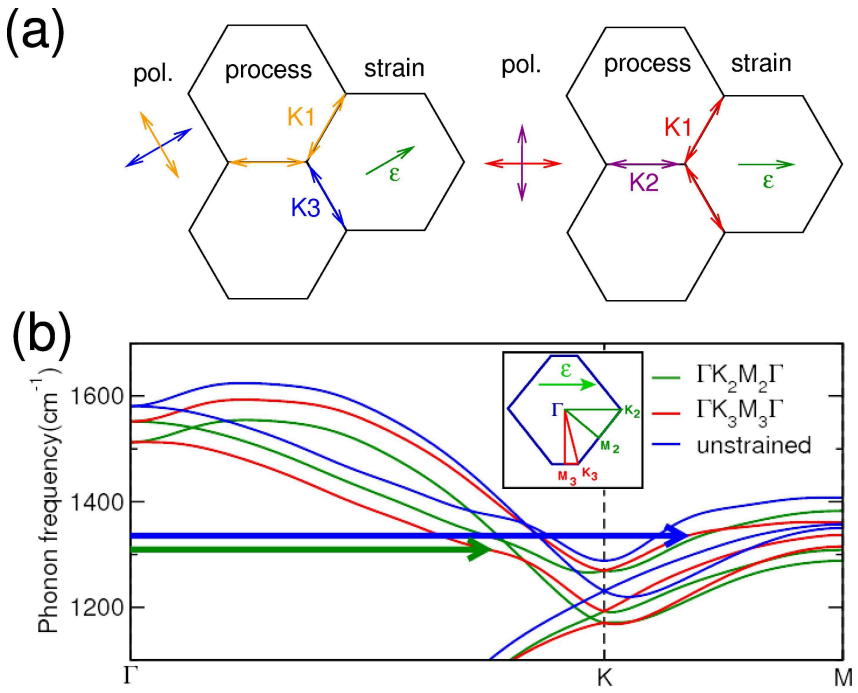

Figure 3.33.: (a) Dominant processes for perpendicular and parallel polarizations for strain in ZZ and AC direction. (b) Optical phonon branch along ΓKM in graphene for unstrained (blue) and 2% strain in ZZ direction (green, red). The corresponding paths in the Brillouin zone is shown in the inset. The blue (green) arrow indicates an outer (inner) process.

3.5. Graphene nanoribbons

In this section the electronic and vibrational properties of graphene nanoribbons are investigated.[¶]Graphene nanoribbons are small stripes of graphene, ideally one-dimensional crystals. They have been fabricated through lithographic [89] techniques, chemical dissolving from bulk graphite [90] and, most recently, the fabrication of nanoribbons by cutting suitable nanotubes has been achieved [91–93]. The restriction in size leads to confinement effects, but nevertheless the chemical bonds are still sp^2-type like in graphene. The propagation of valence electrons in graphene structures is accompanied by an exceptionally strong electron-phonon coupling [94]. The investigation of the vibrational spectrum in these materials is thus of fundamental importance for the electron transport in electronic devices. But also for the characterization of nanoribbons the knowledge of the vibrational properties can be extremely useful. In another well studied low-dimensional structure, the carbon nanotubes (CNTs), details on the exact geometry can be easily obtained from it: The radial breathing mode (RBM) in CNTs corresponds to the vibration of the carbon atoms in the radial direction, as if the tube was breathing. The RBM's frequency is highly diameter sensitive. Resonant Raman measurement of the RBM in CNTs is a standard, straightforward method to precisely determine the CNT diameter and characterize

[¶]The calculations in this section have been performed by Roland Gillen, TU Berlin.

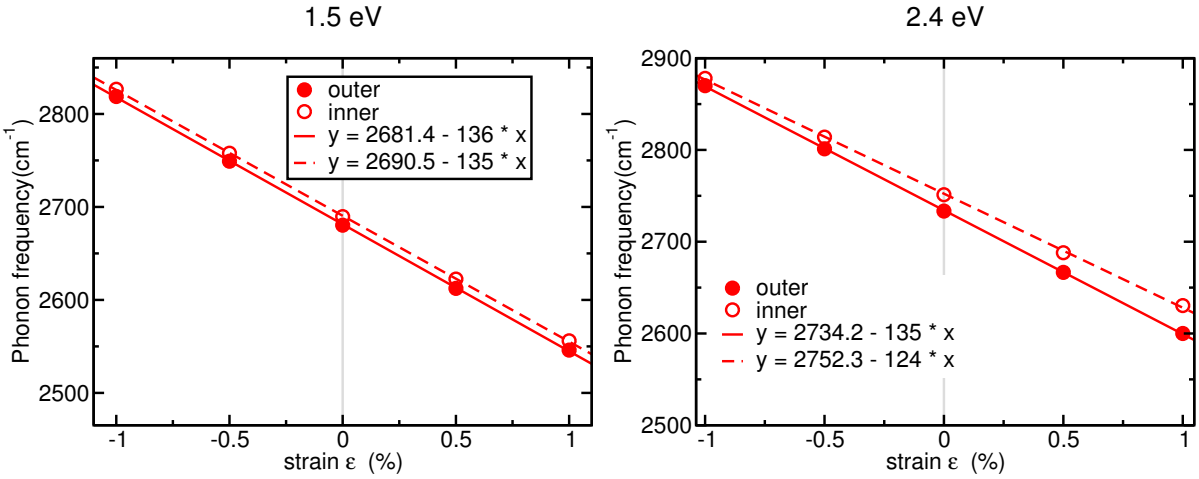

Figure 3.34.: Mapping of the Raman $2D$ contributions for inner and outer processes for the laser energies 1.5 eV and 2.4 eV for biaxial strain. The data points are fitted with a linear function (lines). Dotted lines denote inner, dashed lines denote outer process.

CNT conglomerates [95–97]. Without the systematic study of the electronic and vibrational properties this would not have been possible. To analyze size and geometry-dependent effects the structural, electronic, and vibrational properties of graphene nanoribbons were calculated by means of first-principles calculations on the basis of density functional theory.

Due to limited computational resources, the study of GNR concentrates on those with purely straight edges. For the classification we use the approach of Fujita *et al.* [98], where GNRs are classified by their edge into armchair graphene nanoribbons (AGNR) and zigzag nanoribbons (ZGNR). This classification is in contrast to carbon nanotubes where armchair and zigzag denote the circumference. The corresponding structures are shown in Fig. 3.35. The unit cell is depicted in light gray. The classification is unique by stating the number of dimers N in the unit cell (see Fig. 3.35).

Calculational details

Graphene nanoribbons can be understood as unrolled carbon nanotubes. The edge atoms have a lower coordination number. The formation of dangling bonds at the edges is suppressed in the calculations by adding H atoms to edge atoms. Thus the sp^2-hybridization of graphene is conserved. In Ref. 100 different types of edge passivation have been compared energetically.

Density functional theory in the local approximation [6] was used to calculate N-AGNRs and M-ZGNRs with N=7..15 and M=4..14 respectively. The pseudopotentials were generated with the Troullier-Martins scheme [101] for the following valence-state configurations: C $2s^2(1.49), 2p^2(1.50)$; H $1s^1(1.25)$, where the value in parenthesis indicates the pseudopotential core radii in Bohr. The valence electrons were described by a double-ζ basis set plus an additional polarizing orbital. The localization of the basis followed the standard split scheme and

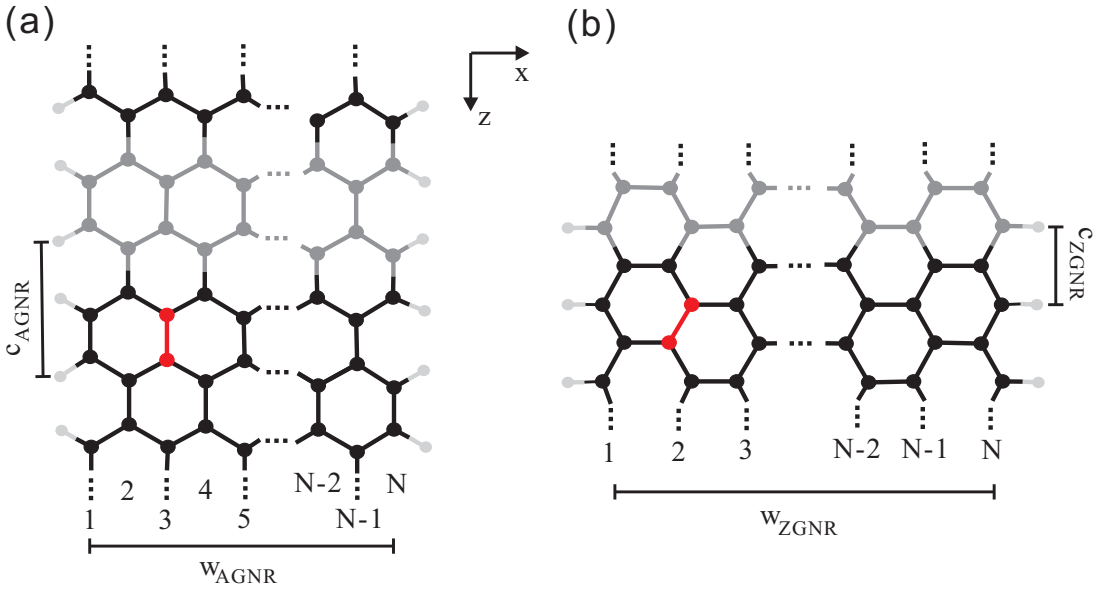

Figure 3.35.: Structure of (a) a N-AGNR and (b) a N-ZGNR. In each case one dimer is emphasized in light grey (red) and a unit cell is emphasized in grey, respectively. The ideal lattice constants of the nanoribbons are $c_{\mathrm{AGNR}} = \sqrt{3}a_0$ and $c_{\mathrm{ZGNR}} = a_0$, where a_0 is the lattice constant of graphene. The corresponding ideal ribbon widths, i.e. the distance between C atoms at opposing edges, are given by Eq. (3.6) and (3.7).

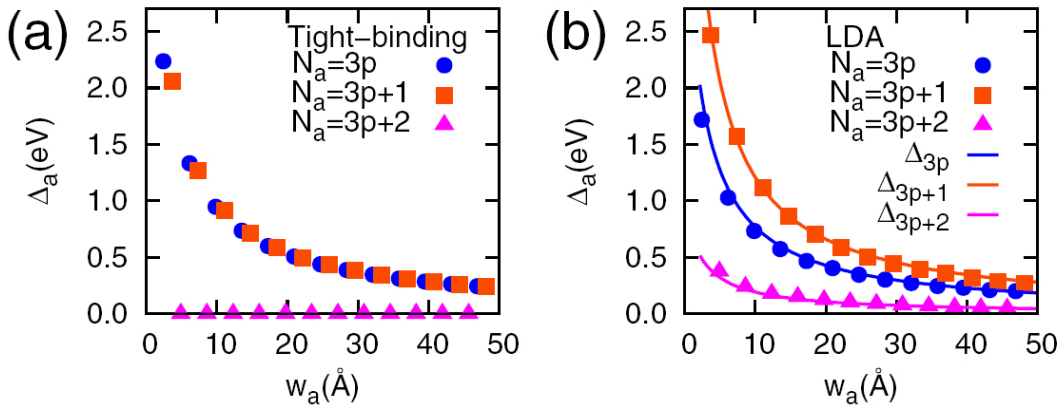

Figure 3.36.: Band gaps of GNR nanoribbons from tight-binding (a) calculations and DFT (b) calculations. Taken from Ref. 99.

was controlled by an internal SIESTA [9, 102] parameter, the energy shift, for which a value of 50 meV was used. This resulted in basis functions with a maximal extension of 3.31 Å (C) and 3.2 Å (H). Periodic images of the nanoribbons were separated by at least 20 Å in order to prevent an interaction. Real space integrations were performed on a grid with a fineness of 0.08 Å, capable to represent plane waves up to an energy of 270 Ry. A minimum of 30 k-points equally spaced along the 1D Brillouin zone was used. The phonon calculations were performed with the method of finite differences [13]. The atomic positions of both AGNRs and ZGNRs were relaxed until the atomic forces were less than 0.01 eV/Å . The total energy was minimized as a function of the lattice constant. A $9 \times 9 \times 1$ supercell was used to calculate the phonon dispersion of graphene. All calculated frequencies were scaled by a constant factor to match the experimentally obtained E_{2g} frequency of 1580 cm^{-1} [33].

3.5.1. Electronic properties

Tuning the ribbon width opens possibilities for band gap engineering [89,99,103,104]. In Fig. 3.36 the width dependence the band gap of AGNR is shown from tight-binding (TB) and DFT calculations. In the TB calculations AGNRs with $N = 3p+2$ dimers show metallic character. Also there is no distinction between the $3p + 1$ and $3p$ families. This behaviour changes completely when using DFT calculations. Now all three families can be well separated. In addition, the nanoribbons which are metallic in TB calculations are now semiconducting as well. This semiconducting behavior can be reproduced in TB calculations by adjusting the hopping integrals at the edges to comply with the reduced bond length at the edges. With this modified hopping parameters the solid lines in Fig. 3.36(b) are obtained [99].

ZG nanoribbons are semiconducting as well. At first sight however, they are metallic. Using the same calculational parameters for ZGNRs as for AGNRs the band structure of Fig. 3.37(a) is obtained. Here no band gap occurs. The edges of zigzag nanoribbons allow peculiar localized states in ZGNR around the Fermi level that induce magnetism [99, 105]. Using spin-orbit interaction this behaviour is correctly reproduced and a band gap opens [Fig. 3.37(b)]. In contrast to AGNRs no family dependence is observed in ZGNR, but a width dependence is present [99]. Applying an external magnetic field the band gap can be closed [99]. This remarkable feature could allow the construction of a magnetic nanoswitch out of ZGNRs.

3.5.2. Vibrational properties

Six of the phonon branches in each nanoribbon correspond to the six phonon modes of graphene. The two in-plane optical modes that correspond to the E_{2g} are not degenerate like in graphene: the transverse optical mode (TO) has a higher frequency than the longitudinal optical mode (LO) for each of our studied AGNRs. Here longitudinal and transversal refers to the axis of the nanoribbon.

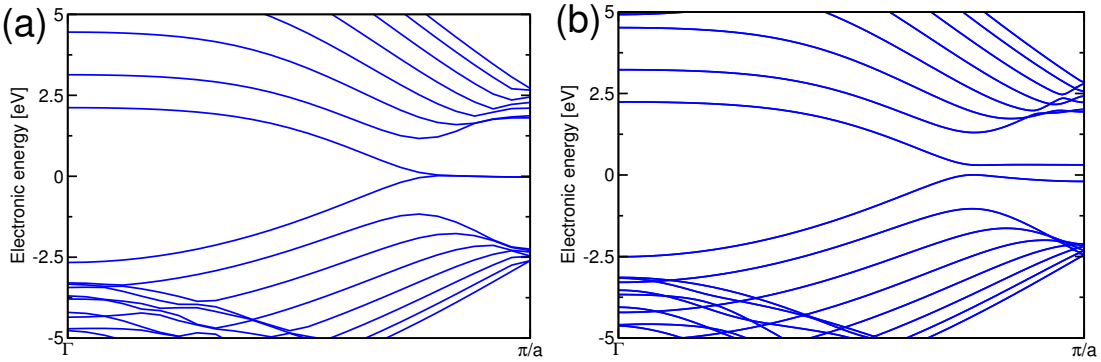

Figure 3.37.: Band structure of a 8-ZGNR without (a) and with (b) the inclusion of spin-orbit interaction. As can be seen, a small gap of ≈0.3 eV is opened at the zone-edge when using spin-orbit interaction.

The frequencies of LO and TO mode of AGNRs are displayed in Fig. 3.38, together with the frequency of the E_{2g} mode in graphene. Graphene can be interpreted as a nanoribbon with an infinite width, thus the frequency of graphene has to be resembled in the limit of large widths. This trend is confirmed. As discussed in the earlier AGNRs can be classified into families $(3p)$, $(3p+1)$ and $(3p+2)$. The splitting between LO and TO found for ribbons of the $N = 3p$ family is ≈29 cm^{-1} for the smallest investigated nanoribbon and around 14 cm^{-1} for the largest one. For the $(3p+1)$ family, we found a splitting of 12-14 cm^{-1} for all investigated nanoribbons. The $(3p+2)$ family displays a larger splitting. It is around 46 cm^{-1} for the 8-AGNR and decreases with increasing ribbon width to a value of around 27 cm^{-1} for a 20-AGNR. All these LO-TO-splittings are large enough to be detectable experimentally. For all TO-modes and all LO-modes except the (3p+2)-family a hardening, *i. e.*, an increase in frequency, compared to graphene is found. The frequencies of the LO-mode of $(3p+2)$-nanoribbons are softened. This is attributed to the small band gap in these quasi-metallic $(3p+2)$ nanoribbons, it is smaller than 0.3 eV for $p > 3$. In metallic carbon nanotubes the LO phonon is strongly softened [106, 107]. We assume a similar effect of a strong electron-phonon coupling related to a Kohn anomaly [41] also takes place in $(3p+2)$ AGNRs.

3.5.3. Zone folding

Graphene nanoribbons have a huge length to width ratio, which results in a quasi-1D crystal-like behavior with a continuous longitudinal wave vector. However, perpendicular to the ribbon axis boundary conditions are induced

$$k_{\perp,n} \cdot w_{\text{ribbon}} = n \cdot \pi$$

on the phonon wave $f(r,t) = A \cdot e^{i(\mathbf{k}\cdot\mathbf{r}-\omega t)}$, leading to a quantized wavevector

$$k_{\perp,n} = \frac{\pi}{w_{\text{ribbon}}} \cdot n \tag{3.5}$$

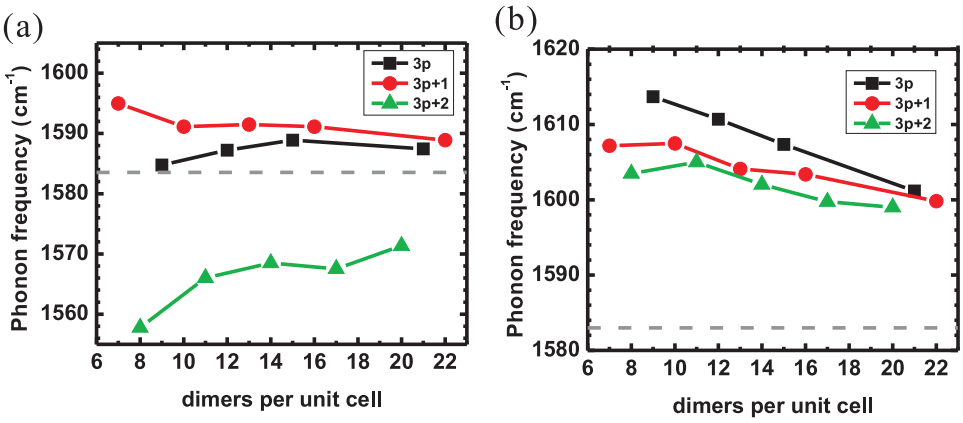

Figure 3.38.: (a) Longitudinal-optical and (b) transverse-optical fundamental mode frequencies of armchair nanoribbons. The dashed line indicates the experimental E_{2g} frequency of graphene.

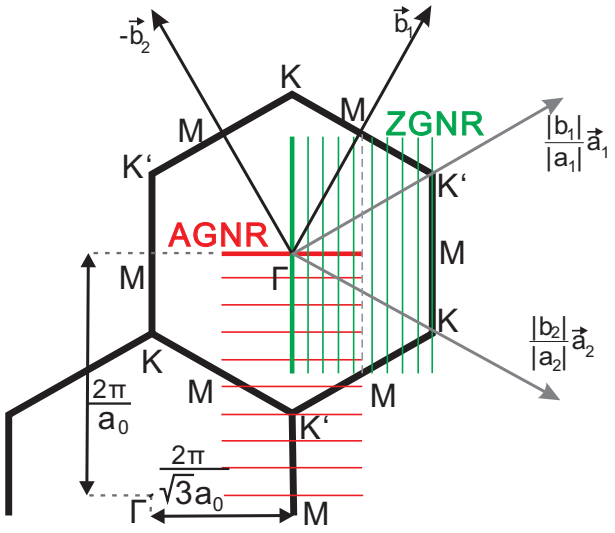

Figure 3.39: Brillouin zone of graphene. $\vec{a}_1$ and $\vec{a}_2$ are the lattice vectors and $\vec{b}_1$ and $\vec{b}_2$ the reciprocal lattice vectors of graphene. The lines visualize the allowed quantized wavevectors of an armchair (10-AGNR) and a zigzag (10-ZGNR) nanoribbons.

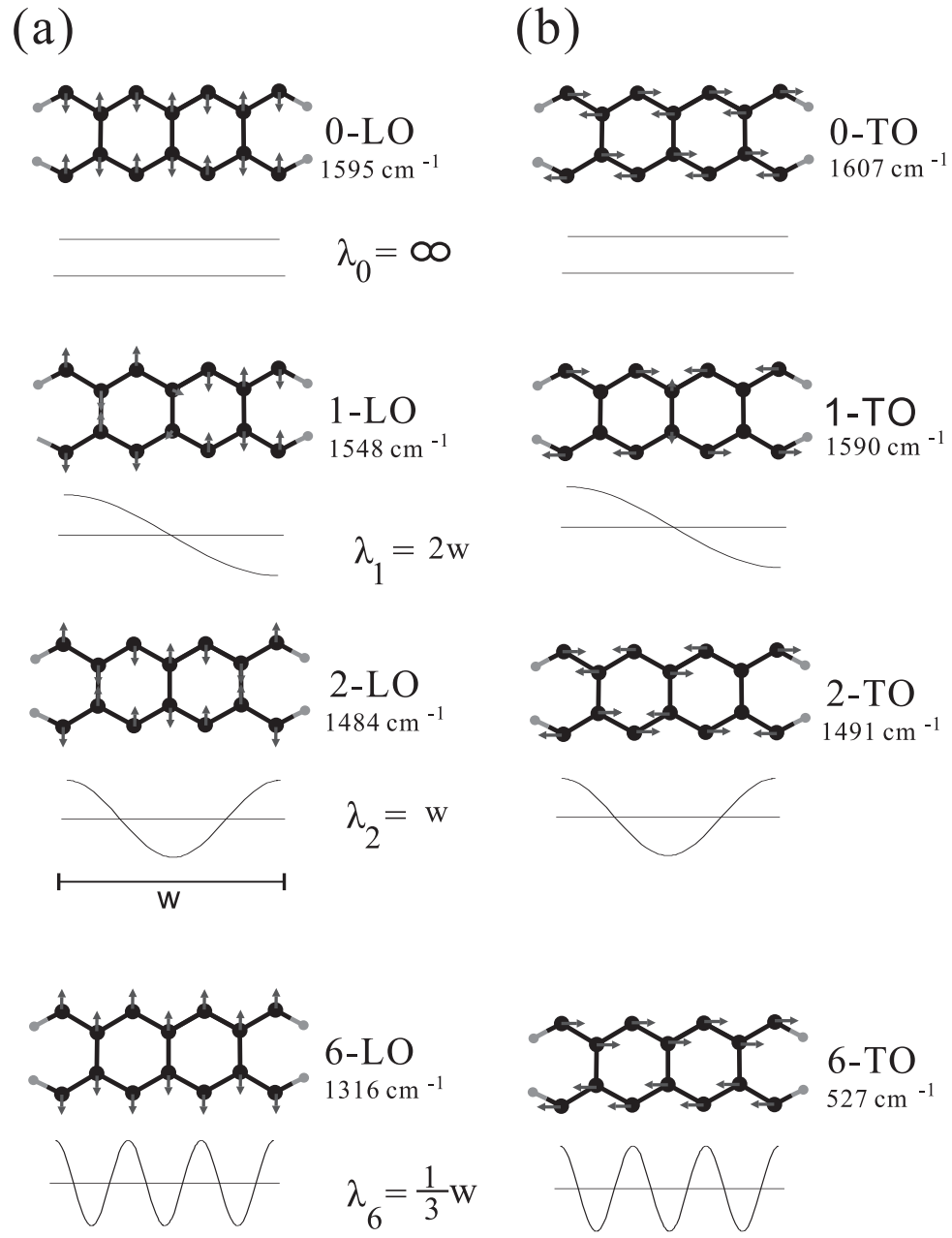

Figure 3.40.: (a) longitudinal-optical (LO) and (b) transversal-optical (TO) fundamental and overtone modes at the Γ point of a 7-AGNR. The arrows display the displacements of the atoms in the unit cell. The displacement strength is equalized to emphasize the node positions. For the n-LO/TO, the eigenvectors of the atoms reverse n-times across the ribbon width compared to the 0-LO/TO. This is further clarified by the envelope curves. The wavelength of the vibrations is $\lambda = \frac{2}{n} w_{\mathrm{AGNR}}$.

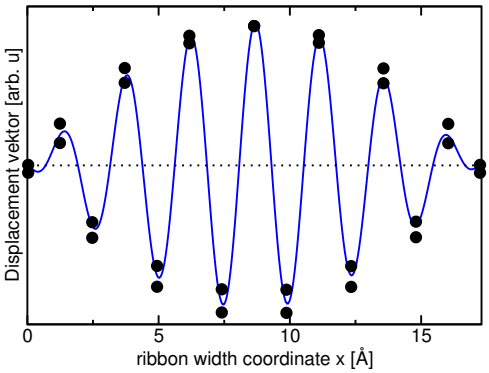

Figure 3.41: Displacement amplitude and fit of the highest optical out-of-plane overtone, the 14-ZO, of a 15-AGNR.

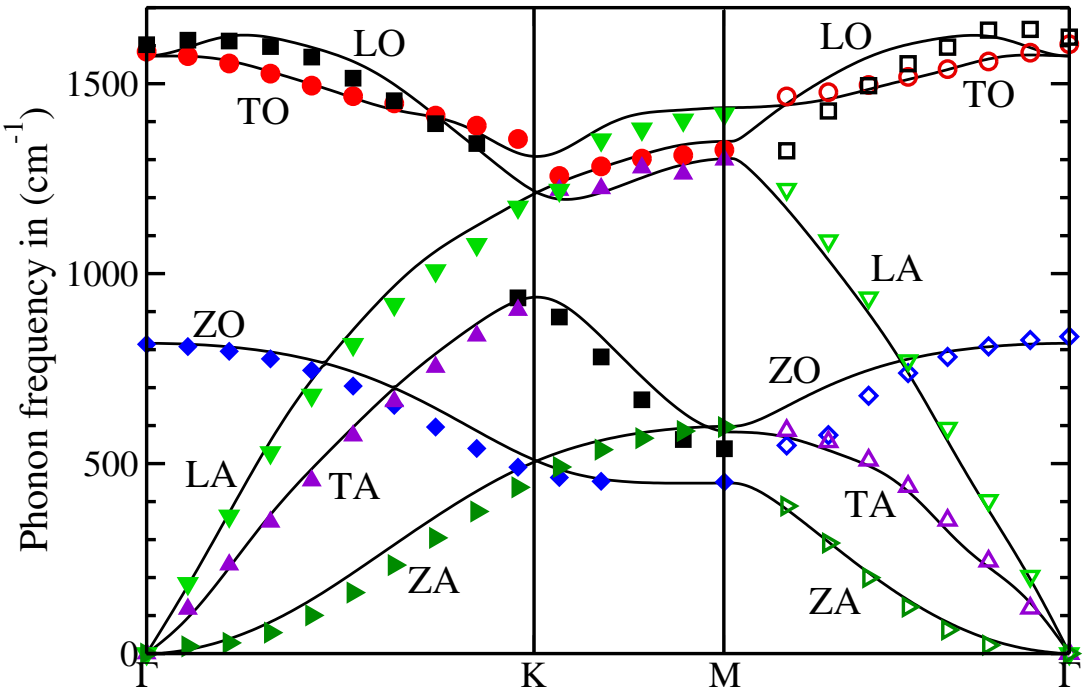

Figure 3.42.: Mapping of TO (black squares), LO (red circles), ZO (blue diamonds), TA (violet upwards triangles up), LA (bright-green downwards triangles), ZA (dark-green rightwards triangles) fundamental and overtone frequencies of a 15-AGNR (filled symbols) and a 8-ZGNR (empty symbols) onto the calculated phonon dispersion of graphene (solid lines).

where n goes from $0, ..., N-1$, where N denotes the number of dimers.

The selection of distinct k-points can be shown in the Brillouin zone of graphene. Fig. 3.39 shows the hexagonal Brillouin zone of graphene. The Brillouin zone of nanoribbons is one-dimensional. When we plot the allowed wavevectors into the Brillouin zone of graphene we obtain equidistant lines. These lines are shown in Fig. 3.39 for a 10-AGNR and a 10-ZGNR.

Defining the width of a graphene nanoribbon is not an unambiguous task. It can be defined as the center of the outermost atoms. However, in experiments, like scanning tunneling microscopy, the visible width is determined by the extended electron cloud. Here, we use the distance between the centers of the outermost dimers as its definition (refer to Fig. 3.35). The idealistic ribbon width (the width of an unrelaxed nanoribbon) depends on N and is given by

$$w_{\mathrm{AGNR}} = \frac{1}{2}(N-1)a_0 \tag{3.6}$$

and

$$w_{\mathrm{ZGNR}} = \frac{\sqrt{3}}{2}(N-1)a_0 \tag{3.7}$$

with the graphene lattice constant a_0.

Analyzing the Γ-point phonons of nanoribbons we find modes whose one-dimensional projection show similarities to the fundamental mode of a string. In addition, other modes' projection look like overtones of this fundamental mode. This is illustrated in Fig. 3.40 for a few modes. For every ribbon we find $(N-1)$ overtones for the LO, TO and ZO-mode, respectively. The nodes do not have to coincide with carbon atom positions in the unit cell. Figure 3.40 shows displacement patterns of a 7-AGNR. The phonon modes are characterized by their direction of vibration (longitudinal, transverse, out-of-plane) and their nature (acoustic, optical) as n-LA/TA/ZA and n-LO/TO/ZO, with n = number of nodes.

The displacement pattern and the fit with Eq. (3.8) is shown in Fig. 3.41 for the highest, *i. e.*, $(N-1) = 14$ overtone of a 15-AGNR. The length of the displacements $f_n(x)$ are best described by the circular function

$$f_n(x) = A_n \sin k_{\perp,n} x = A_n(x) \sin(\frac{2\pi}{\lambda_{\perp,n}} x), \tag{3.8}$$

where the amplitude $A_n(x)$ is defined by $A_n(x) = \tilde{A}_0 \cdot \sin(\frac{2\pi}{2w_{\mathrm{ribbon}}}(x)))$.

With the knowledge of the wavelength $\lambda_{\perp,n}$ the wavevector $k_\perp$ can be determined. We tentatively plotted the resulting mapping of all Γ-point modes of a 15-AGNR and a 8-ZGNR with the resulting wavevectors $k_\perp$ onto the phonon dispersion of graphene in Fig. 3.42. The modes of the AGNR are plotted on the dispersion along $\Gamma K M$, that of the ZGNR on the dispersion along ΓM (see also Fig. 3.39). As can be seen, the agreement is excellent. This implies that effects of the edges or the hydrogen passivation have only little influence on the vibrational properties of GNRs. This is remarkable, as the bond lengths of the C-C bonds at the edges are smaller than

in the center.

4. Carbon nanotubes

4.1. Introduction

Carbon nanotubes are thin hollow tubules consisting of carbon atoms. They were first discovered and characterized in 1991 [24]. Depending on the number of walls they are classified into single-walled, double-walled or multi-walled carbon nanotubes. Single walled nanotubes (SWNT) have quite small and uniform diameters in the 1 nm-regime. This small diameter combined with crystalline perfection along several microns make them an ideal 1D crystal and a test system for confinement and quantum effects. Besides they are interesting also for applications due to their extraordinary properties: the strong sp^2 binding makes them a very hard material, combined with a low density [23, 108]. Also their electronic properties are outstanding, giving rise to ballistic conduction (or ballistic transport) in metallic nanotubes [109]. This implies coherent transport over μm-distances.

Because carbon nanotubes can be interpreted as rolled-up graphene sheets, the classification of SWNT is done using the graphene lattice (see Fig. 4.1). All nanotubes (NTs) can geometrically be obtained rolling up a graphene strip which can be defined by its circumferential vector, also called chiral vector $\mathbf{C}_h$. This vector is given by adding multiples of graphene lattice vectors $\mathbf{a}_1$ and $\mathbf{a}_2$: $\mathbf{C}_h = n_1 \cdot \mathbf{a}_1 + n_2 \cdot \mathbf{a}_2$. So by giving the pair of indices (n_1, n_2) all nanotubes can be uniquely defined. This is illustrated in Fig. 4.1. The chiral angle φ is defined between the $\mathbf{c}_h$ and $\mathbf{a}_1$. Depending on this angle nanotubes are classified into zigzag [$\varphi = 0°$, (n,0)] and armchair [$\varphi = 30°$, (n,n)]. These are referred to as achiral NTs, all others ($0 < \varphi < 30$) are referred to as chiral NTs.

Remarkable is the strong influence of the chiral indices (n_1, n_2) on the electronic properties with non-monotonic behaviour: the (5,2)-tube is metallic, whereas the (5,1) and the (5,3) have band gaps E_g of 2.2 eV and 1.3 eV, respectively.

The symmetry of nanotubes can be described in terms of line groups [110]. They are specially designed for 1D-crystals, *e.g.* , DNA, polymers, nanotubes, and nanowires. In line groups the translation along the axis is entirely implemented. In that sense, they correspond to the space groups that describe infinite 3D crystals. One main difference between line groups and space groups is the fact that arbitrary rotations are allowed, not only rotations by $2\pi/n$, where $n = 2, 3, 4, 6$. Symmetry considerations in nanotubes are extremely helpful. All SWNT are single-orbit systems: for the generation of a nanotube only the coordinates of one atom is

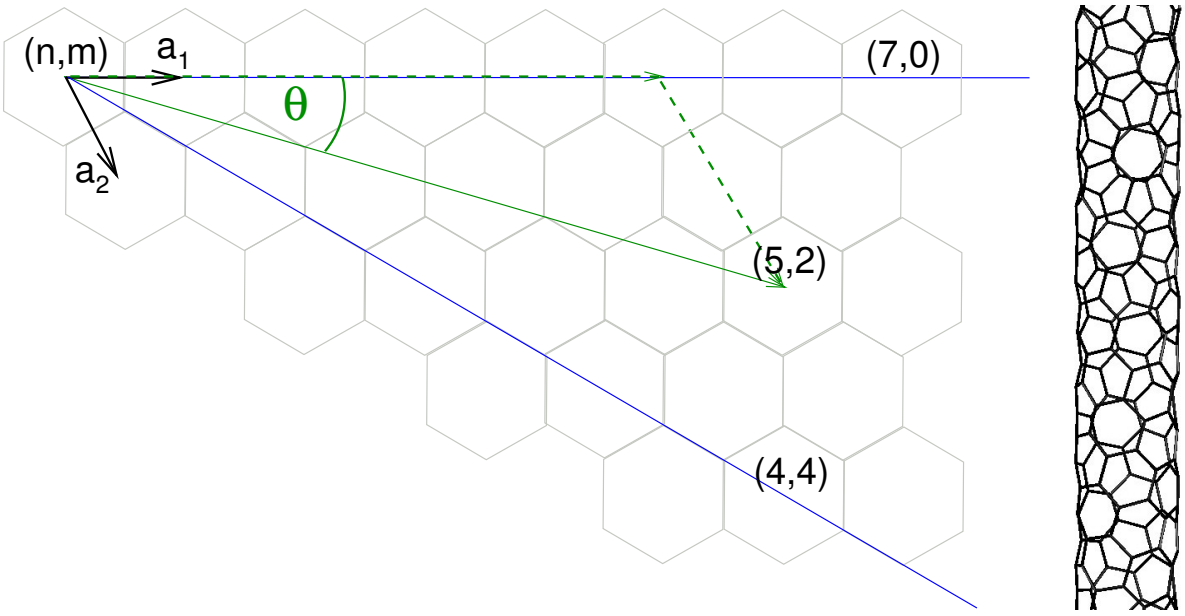

Figure 4.1.: Graphene honeycomb lattice with lattice vectors $\mathbf{a}_1$ and $\mathbf{a}_2$. The chiral vector $\mathbf{C}_h$ of a $(5,2)$-tube is displayed. Perpendicular to $\mathbf{C}_h$ is the tube axis. The resulting $(5,2)$ tube is shown on the right.

needed, the coordinates of all other atoms are obtained by symmetry [111].

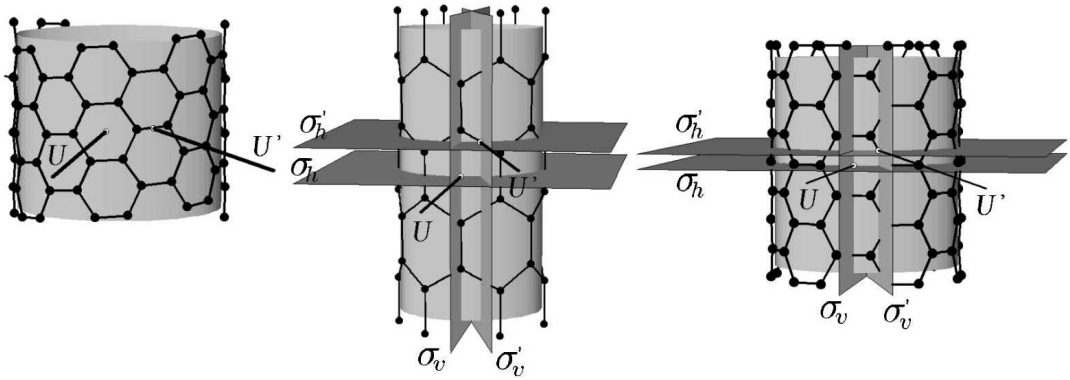

Figure 4.2.: Symmetries of the single-wall nanotubes (8,6), (6,0) and (6,6). The rotational axes U and U' are symmetries in all NTs. The mirror planes (σ_v and σ_h), the glide plane σ'_v and the rotoreflectional plane σ'_h are only symmetries in zigzag and armchair NTs. Taken from Ref.111.

4.2. Raman-active modes

A widely established method for characterization of carbon nanotubes is Raman spectroscopy [112]. A Raman spectrum of a nanotube bundle is shown in Fig. 4.3. The Raman spectrum of nanotubes mainly consists of the following features: the radial breathing mode (RBM) in

the low energy range, the defect-induced D-mode around 1300 cm^{-1} and the high-energy modes (HEMs) around 1600 cm^{-1}.

The RBM plays a key role in the characterization of carbon nanotubes (NTs). Its diameter-dependent frequency is used in resonant Raman spectroscopy to estimate the nanotube diameter d and for chirality assignments [97,113]. The defect-induced D-mode, common to all sp^2 carbon structures, is a double-resonant Raman mode. Its Raman shift is excitation-energy dependent. The origin of the D-mode in nanotubes is the same as in graphene, which was discussed in Sec. 3.4.3. The high-energy modes (HEMs) around 1600 cm^{-1} correspond to the doubly-degenerate optical E_{2g} in graphene.

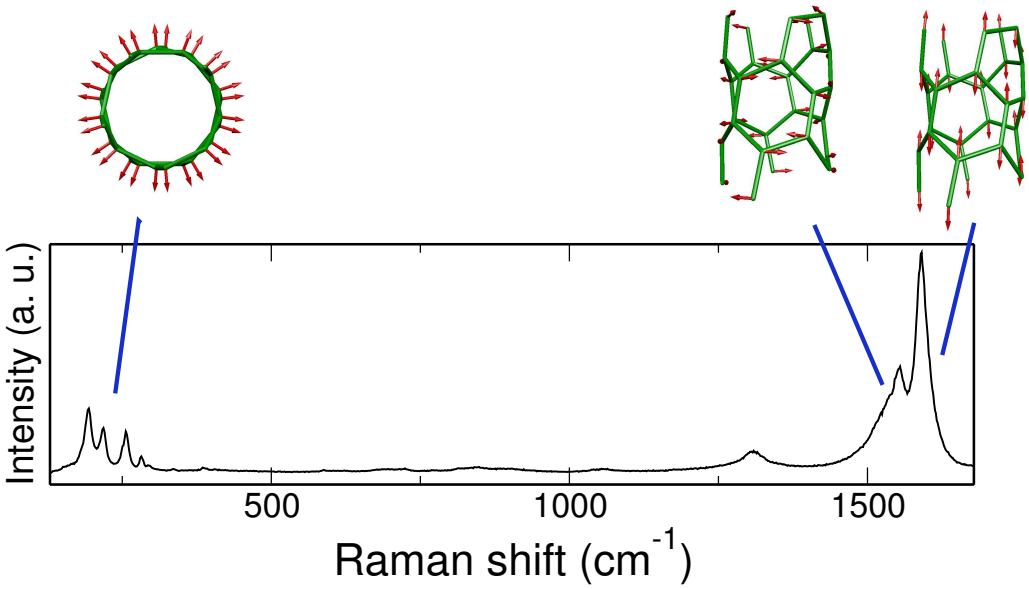

Figure 4.3.: Raman spectrum of a carbon nanotubes bundle recorded with an excitation wavelength of 514 nm. The corresponding displacement pattern of the RBM and the HEM of a (4,1)-tube are shown.

The radial breathing mode is often assumed to be purely radial, [114, 115] although several independent studies showed that it has small non-radial components [61, 116–118]. Similarly, for the HEM small non-tangential components have been found [54].

Since both the RBM and HEMs are fully symmetric their coupling is not forbidden by symmetry. This was first pointed out by Kürti *et al.*, [116] who found slight deviations from the ideal $1/d$ behavior of the RBM-frequency, depending on tube chirality and conduction character.

4.3. Variational method

Our variational DFT approach is based on the fact that an atomic displacement increases the total energy of a nanotube. If we displace all atoms according to a pattern that corresponds to an

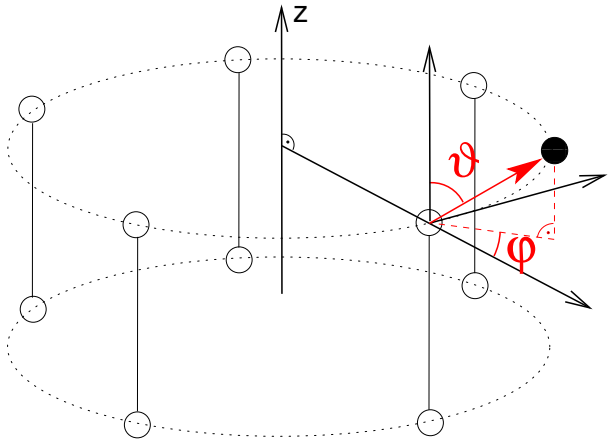

Figure 4.4: A section of a (5,0) nanotube illustrating the definition of φ and ϑ.

irreducible representation, the direction with extremal value of this energy increase corresponds to a vibrational normal mode. Said another way, for a set of displacement patterns with a given symmetry, the energy has a local extremum when the pattern coincides with a vibrational eigenvector. The same idea has been applied in Ref. 119 for nanotubes, but within oversimplified dynamical model, and Ref. 120 for benzene.

The displacement pattern was obtained in the following way: one atom of the relaxed nanotube structure was moved on the surface of a sphere centered on the relaxed position of the atom with a fixed radius r. This is shown in Fig. 4.4 for a (5,0)-tube. Then, the same symmetry operations that are used to construct the nanotube from one atom (not including mirror operations) were applied to the displacement and the resulting set of displacements was added to the relaxed positions [111]. Thus, the displacement pattern of the whole NT is defined by the displacement of one atom. The displacement pattern obtained in this way for a (7,4) tube is shown in Fig. 4.5. We define the displacement direction by two parameters φ and ϑ as shown in Fig. 4.4 and evaluate the total energy as a function of these parameters. For $r = 0.02\,\text{Å}$, far enough within a region where nonlinear effects are negligible (even for $r = 0.04\,\text{Å}$ the deviation from linear behavior is smaller than 1%) we find considerable differences in total energy between different directions. As required by a fully-symmetric displacement, all atomic forces are equal within our accuracy of $0.01\,\text{eV/Å}$. *

4.4. Eigenvectors and frequencies

We scanned the full (ϑ, φ) parameter range for selected nanotubes. The energy $E(\vartheta, \varphi)$ over a half sphere for all nanotubes shows a minimum in the vicinity of $(\vartheta = 90°, \varphi = 0°)$ and two

* *Ab-initio* calculations were performed with the SIESTA code [9,102] using the LDA functional in the parameterization of Perdew and Zunger [6] and Troullier-Martins [101] pseudopotentials. An equivalent energy cutoff of 270 Ry was used for the real space grid integrations and an $(1\times1\times30)$ Monkhorst-Pack [121] mesh in reciprocal space. The valence electrons were described by a double-ζ basis set with a cutoff radii of 5.12 and 6.25 Bohr for the s and p orbitals, respectively plus an additional polarizing orbital. The undisplaced coordinates were obtained from relaxing all atoms until all forces were below $0.01\,\text{eV/Å}$.

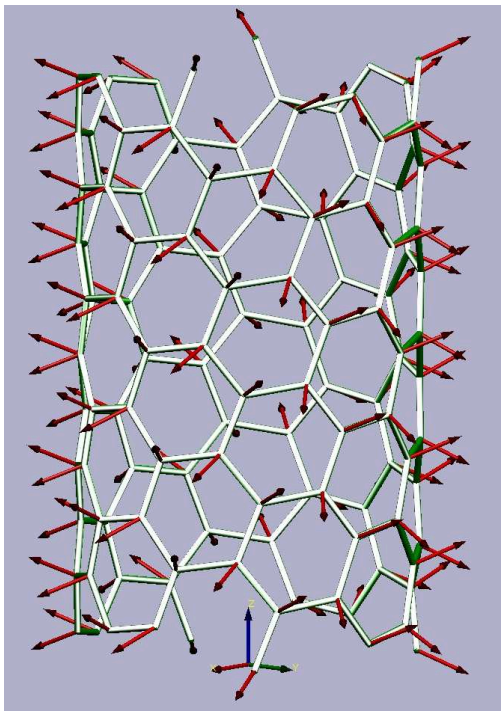

Figure 4.5: Fully symmetric displacement scheme for the (7,4) nanotube for $\varphi = 2.9°$and $\vartheta = 87.1°$.

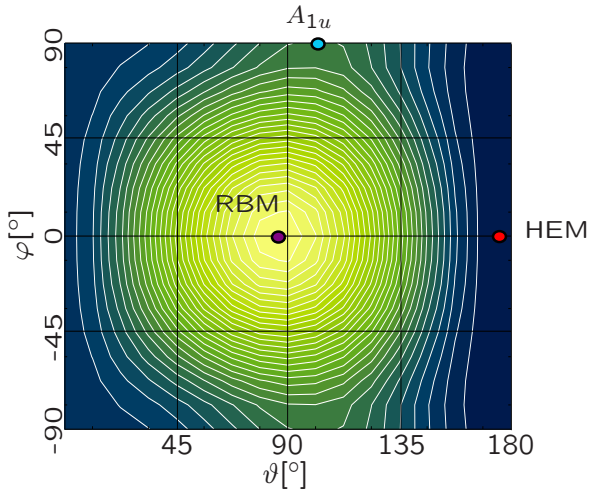

Figure 4.6: Contour plot of the total energy for a full spherical fully-symmetric displacement of a (5,0) nanotube. The minima (bright yellow) is slightly displaced from the point $(90°, 0°)$, which would correspond to a purely radial displacement. The mirror symmetry at $\varphi = 0°$ corresponds to the mirror plane of zigzag-tubes and can nicely be seen.

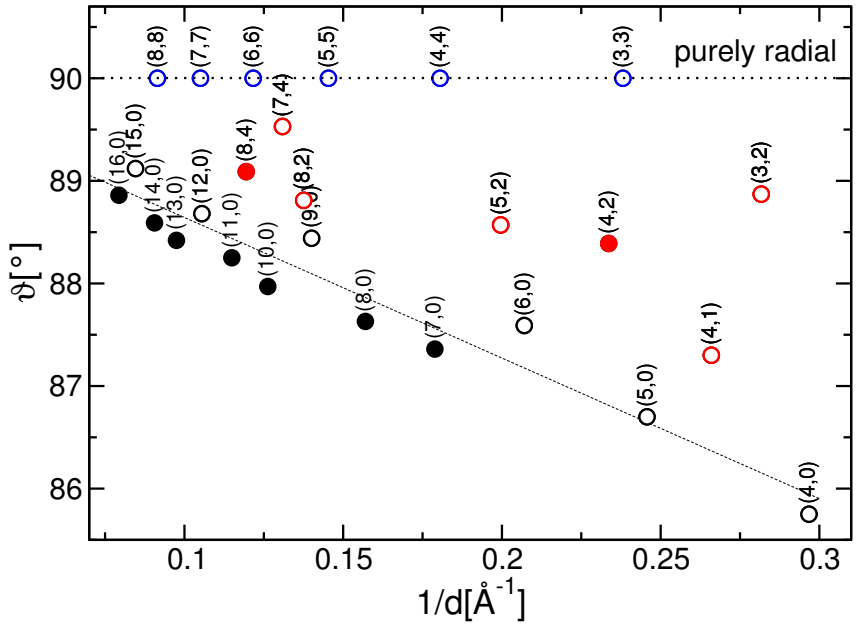

Figure 4.7.: Angle ϑ as function of the inverse nanotube diameter for several nanotubes (open symbols denote metallic, filled symbols semiconducting NTs). The full line shows a linear fit for all zigzag NTs. The metallic $(n,0)$ NTs are above the line, the semiconducting $(n,0)$ are below. Thus, the RBM is more radial for metallic zigzag NTs than for semiconducting zigzag NTs.

saddle points close to $(\vartheta = 90°, \varphi = -90°)$ and $(\vartheta = 180°, \varphi = 0°)$ (see Fig. 4.6) For achiral NTs one of the saddle points corresponds to the fully symmetric HEM and the other to an A_{1u}-mode, as expected by symmetry.

For all other NTs we scanned only the vicinity of the minimum around the point $(\vartheta = 90°, \varphi = 0°)$ which corresponds to the radial displacement. To obtain the direction of minimal energy, the total energy values were then fitted to a two-dimensional function of third degree. This fit was used to find the energy minimum $E(\vartheta, \varphi)$ analytically. In the following the position of this minimum is called the eigenvector of the RBM. The values of ϑ and φ of the RBM eigenvector over the inverse NT diameter are shown in Figs. 4.7 and 4.8, respectively. As can be seen, the radial-breathing mode has non-radial components irrespective of the chirality of the tube. These components become smaller as the diameter of the tube increases.

The achiral nanotubes have $\varphi = 0°$ (zigzag NT) and $\vartheta = 90°$ (armchair NT). This is due to their higher symmetry as compared to chiral nanotubes. Achiral NTs possess mirror planes, and therefore the fully-symmetric representation A_1 of chiral NTs splits into the two representations A_{1g} and A_{1u}, even or odd under the mirror operation, respectively. Since armchair NTs possess a mirror plane perpendicular to the z-axis and zigzag tubes possess a mirror plane that contains the z-axis, the even A_{1g} mode cannot have components perpendicular to these planes. This symmetry restriction is the reason for the specific values ϑ and φ of these NTs in Figs. 4.7 and 4.8 ($\vartheta = 90°$ for armchair and $\varphi = 0°$ for zigzag NTs).

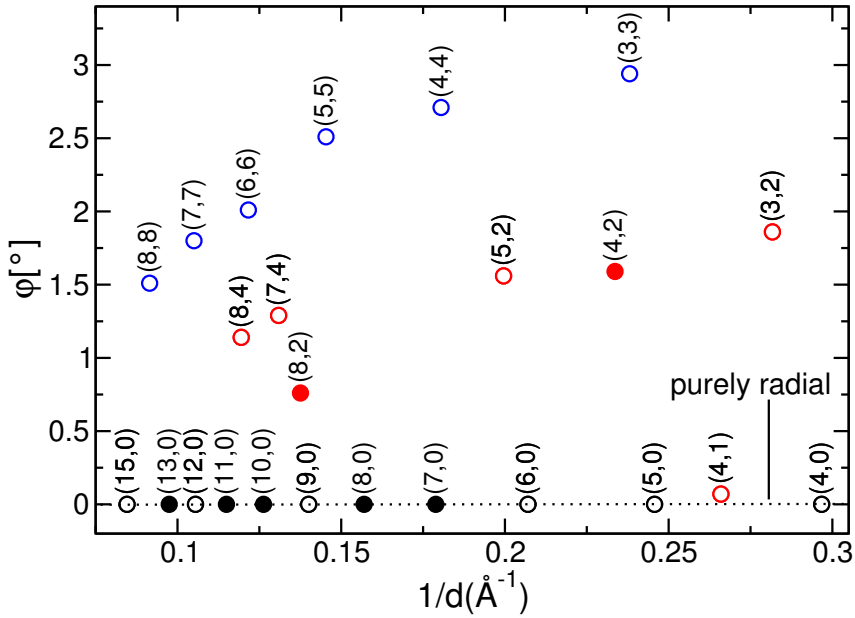

Figure 4.8.: Angle φ as a function of the inverse nanotube diameter. We use the same symbols as in Fig. 4.7.

Estimate of the non-radial component The RBM of metallic zigzag NTs [$(n, 0)$, n divisible by three] shows a smaller non-radial component than semiconducting NTs of similar diameter. The non-radial component of metallic zigzag NTs shows a good agreement with the calculations of Dobardžić *et al.* [61], whereas we obtain slightly larger non-radial components for semiconducting zigzag NTs. As the force constants in Ref. 61 were obtained from (semimetallic) graphite, differences between semiconducting and metallic NTs are not expected.

A simple model for the magnitude of the non-radial component of the eigenvector can be derived from considering the atomic forces in graphene. The non-radial component of the RBM compensates the non-radial forces caused by the bond stretching due to radial deformation. To simulate a purely radial vibration of a zigzag tube in graphene, we calculated the atomic forces after stretching the unit cell of graphene in zigzag direction. Due to graphene's symmetry the resulting forces are perpendicular to the stretching direction, and form a HEM-like pattern. We calculated the length of the HEM displacement necessary to compensate these forces. From a fit of these data we obtain the normalized non-radial component of the RBM eigenvector $z_{\mathrm{RBM}} = \cos\theta$ of $(n,0)$ zigzag nanotubes

$$z_{\mathrm{RBM}} = \frac{2\pi}{19.7}\frac{1}{n}. \tag{4.1}$$

This is in good agreement with our data and the calculations of Ref. 61, as can be seen in Fig. 4.9. For larger NTs, where the effect of curvature becomes small, the agreement with Ref. 61 is excellent. This result can be extended to chiral tubes when multiplied with the factor $\cos(3\Theta)$,

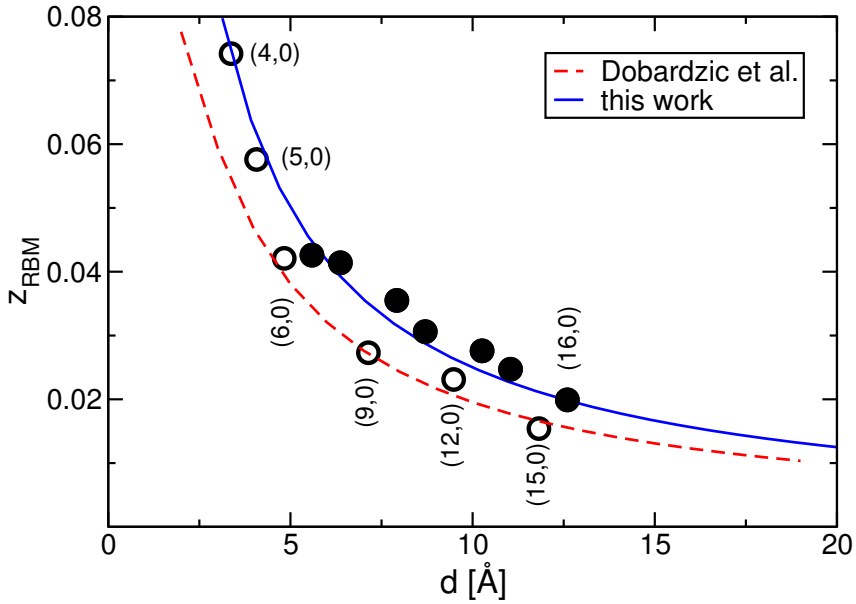

Figure 4.9.: Normalized non-radial component of the RBM eigenvector z_{RBM} for zigzag NTs compared with Dobardžić *et al.* [61] and our simple graphene model. The data of the metallic NTs fit well the model of Dobardžić *et al.*, whereas the semiconducting NTs that show larger components, better fits with this model. The same symbols were used as in Fig. 4.7.

where Θ defines the chiral angle of the NT.

Frequencies of the fully-symmetric modes We are interested in the influence of the small non-radial component on the phonon frequency. We calculated the RBM frequency in a frozen-phonon (FP) approach (see Sect. 2.1.5). For comparison we also calculated the frequencies for the purely radial displacement and found them to be overestimated by up to $10\,\mathrm{cm}^{-1}$. This confirms the results of Milošević *et al.* [117] The frequencies are in excellent agreement with experimental results and with *ab-initio* finite-differences calculations [118, 122]. A linear fit of our data $\omega_{\mathrm{RBM}} = c_1/d + c_2$ leads to $c_1 = 2221\,\text{Å}\,\mathrm{cm}^{-1}$ and $c_2 = 2\,\mathrm{cm}^{-1}$ in excellent agreement with other *ab-initio* results, e.g., $c_1 = 2282\,\text{Å}\,\mathrm{cm}^{-1}$ from Ref. 123 or $c_1 = 2340\,\text{Å}\,\mathrm{cm}^{-1}$ from Ref. 116, or experimental data $c_1 = 2150\,\text{Å}\,\mathrm{cm}^{-1}$ and $c_2 = 18\,\mathrm{cm}^{-1}$ from Ref. 122. So for accurate frequency calculations, the RBM may not be approximated as a purely radial displacement.

Similarly we calculated the frequencies of the Raman-active HEM for the non-mixed displacement, strictly perpendicular to the radial direction. We compare them to frequencies from finite-differences calculations that include mixing with the RBM in Fig. 4.14 [124]. Differences for the HEM frequency between semiconducting and metallic NTs, the so-called phonon softening, are well established in literature [54, 125]. Also the mixing has different consequences for metallic and semiconducting NTs: For semiconducting NTs the results differ by up to $20\,\mathrm{cm}^{-1}$. In metallic NTs the difference is as high as $50\,\mathrm{cm}^{-1}$ in the opposite direction: the frequencies are higher if no mixing is allowed. As for the RBM frequency, the mixing influences the phonon

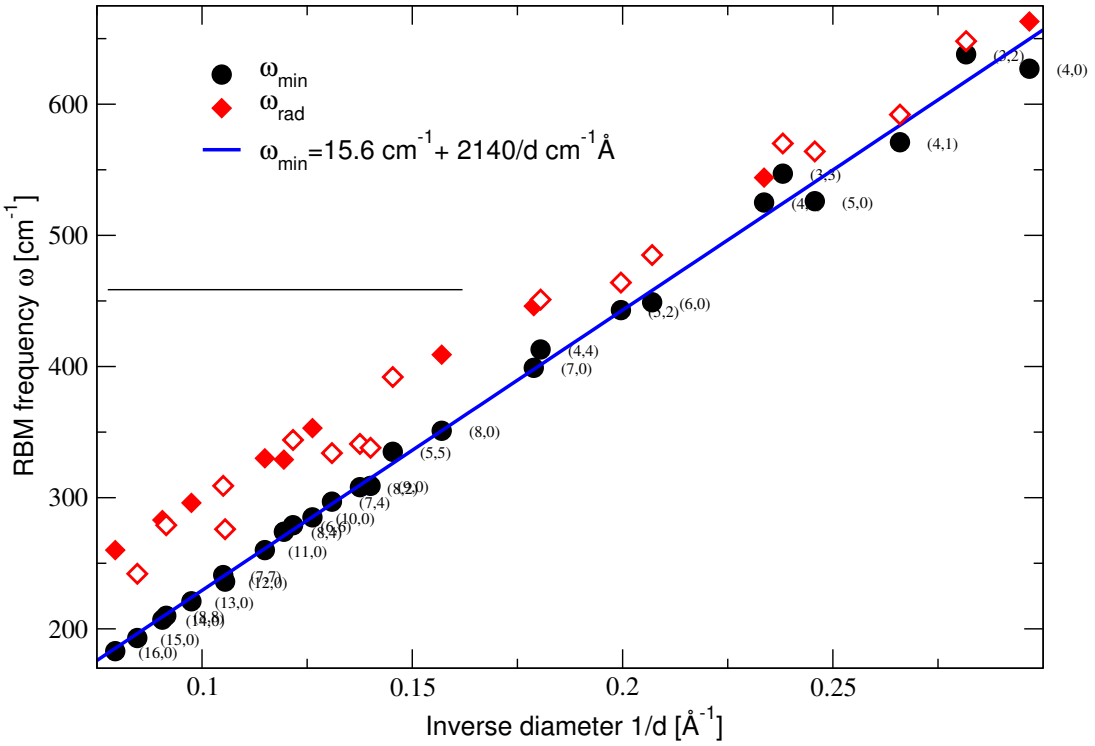

Figure 4.10.: The RBM frequencies: $\omega_{\rm rad}$: pure radial displacement $\omega_{\rm min}$: taking the HEM-RBM mixing into account, Excellent agreement with experimental fit: $\omega_{\rm RBM} = 18\ {\rm cm}^{-1} + 2150/d\ {\rm cm}^{-1}{\rm Å}$.[3] For larger NTs the deviation of $\omega_{\rm rad}$ from $\omega_{\rm min}$ increases. The widely used pure radial displacement oversimplifies the problem and leads to wrong frequencies. In addition a pure radial displacement leads to a chirality-dependent frequency. Semiconducting NTs (filled symbols) show a stronger deviation than the metallic NTs (open symbols).

frequency and the fully-symmetric HEM is not purely axial or not purely circumferential in zigzag and armchair NTs, respectively.

4.4.1. Anharmonicity of the high-energy mode (HEM)

A closer look at Fig. 4.6 reveals that the energies at ϑ=0° and 180° are not exactly equal. However for purely harmonic vibrations this is expected. † A frozen-phonon *ab-initio* calculation for the E_{2g}-mode in graphene show also differing energies at positive and negative displacements for the corresponding direction. This direction correspond to displacements parallel to the C-C bonds. The result for graphene is shown in Fig. 4.12. This is a consequence of the three-fold geometry. To prove this we use a simple model that only considers bond-stretching interaction between nearest neighbors. In an E_{2g}-mode of graphene neighboring atoms move in opposite directions (see Fig. 3.14). If we fix the three neighbors and only move the central atom, the

†A similar anharmonicity is found in MgB_2, which is also a hexagonal system. The anharmonicity of the E_{2g}-mode in MgB_2 is believed to play a role in superconductivity [11].

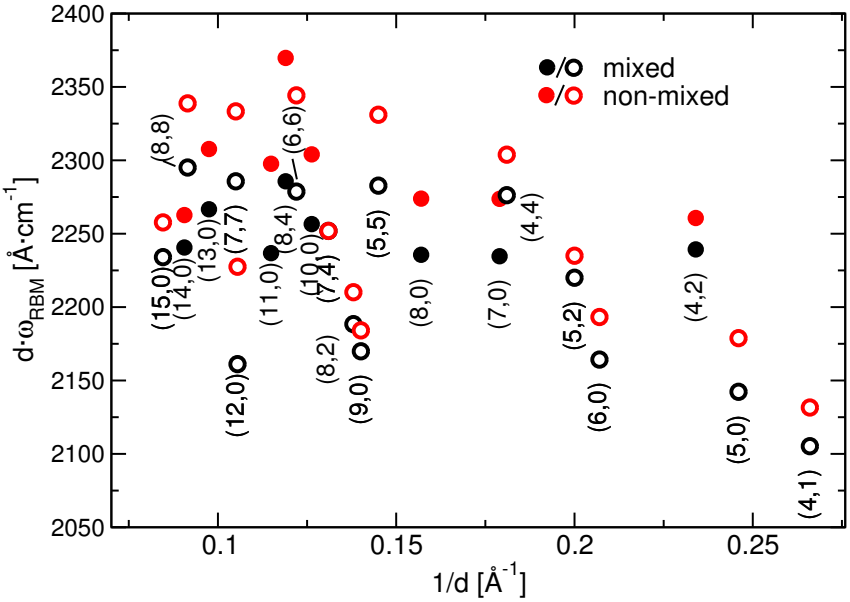

Figure 4.11.: Frequency ω_{RBM} multiplied with tube diameter d for mixed (black symbols) and non-mixed (red symbols) frozen-phonon calculation.
(metallic=open symbols, semiconducting=filled symbols)

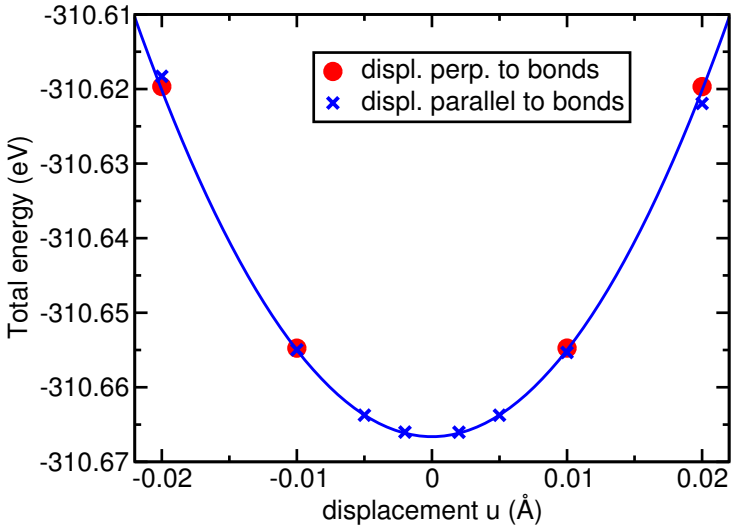

Figure 4.12: Total energy of graphene subjected to a displacement pattern corresponding to the E_{2g}-mode. Solid line is a strictly quadratic fit to $y = ax^2 + b$. An anharmonicity can be seen, when the atoms are displaced parallel to the graphene c-c bonds.

same relative distances are obtained as in the E_{2g}-mode. The central atom (see Fig. 4.13) is considered to be connected to its neighbors with springs with a linear force-constant k. The C-C distance is considered to be 1 unit of length and $k = 1$ unit of force unit/ unit of length. Now the potential energy stored in the system is that of of the three springs, $E = \sum_i \frac{1}{2}k(\Delta s_i)^2$, where Δs_i denotes the change in length of the i-th spring. On the right side of Fig. 4.13 the potential energy of the three springs is plotted for a displacement of 2 % of the C-C distance as a function of the radial angle α. The radial angle $\alpha = 0°$ is indicated on the left side of Fig. 4.13. Only for the values $\alpha = 30°$, $90°$ and $150°$ the potential energies for the positive (α) and negative

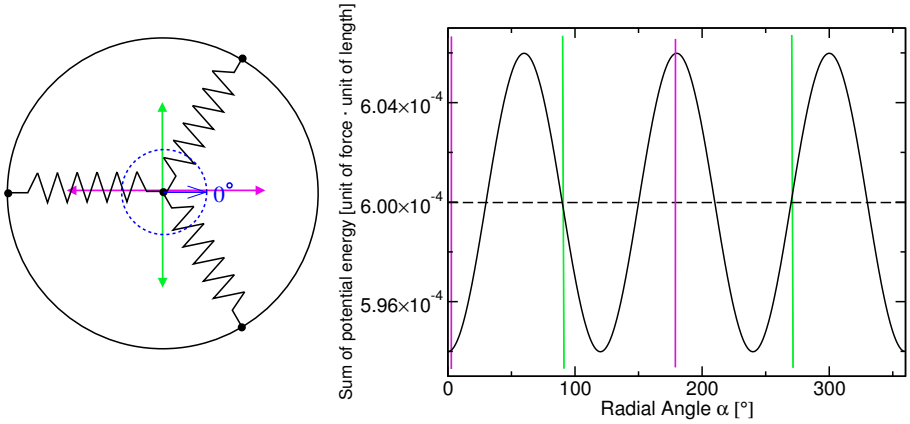

Figure 4.13.: (Left) Three-spring model to prove the geometric origin of the anharmonicity of the HEM or E_{2g}-mode. (Right) Sum of potential energy for the radial displacement as shown in left figure. Green line: Potential energy remains the same for positive and negative displacement [as required by the mirror symmetry, see (left)]. Violet line: Maximum difference in potential energy for positive and negative displacement. This occurs, when the displacement is parallel to the bond in agreement with Fig. 4.6 for nanotubes and Fig. 4.12 for graphene.

displacement ($\alpha+180°$) are equal. This is in agreement with all mirror-planes and the three-fold rotation. For all other values of α the potential energy at positive and negative displacements differ. For a displacement of 2 % of the nearest-neighbor distance, we find a relative difference in potential energy of 2 % between the maximum and the minimum. This is of similar magnitude as the relative energies at ϑ=0° and 180° and supports the geometric origin of this anharmonicity.

The anharmonicity does not seem to have an effect calculating the phonon frequencies. Within the frozen phonon approximation, the frequency is obtained from the quadratic coefficient of the potential energy versus the displacement [13]. A fit of the energy versus displacement for $\alpha = 90°$ is perfectly harmonic. A 3rd order fit for $\alpha = 0°$ leads to non-zero values for the linear and cubic coefficients, but to the same quadratic coefficient as for $\alpha = 90°$, and thus yields the same phonon frequency. As the common methods for phonon calculations (finite differences or linear response) use the harmonic approximation to obtain the phonon frequency, this effect could not be detected by these methods.

4.5. Deformation potentials and electron-phonon coupling

Experimentally, nanotubes are often identified *via* resonant Raman scattering of the diameter-dependent RBM and comparing the results with empirical data or theoretical predictions [97]. The squared magnitude of the electron-phonon interaction $|\mathcal{M}_{e-ph}|^2$, among other factors, determines the Raman cross section and can be observed experimentally [115,124,126]. For small-chiral-angle NTs $|\mathcal{M}_{e-ph}|^2$ can be one order of magnitude larger than for armchair tubes [118]. This finding has consequences for the determination of abundances in an ensemble of nanotubes;

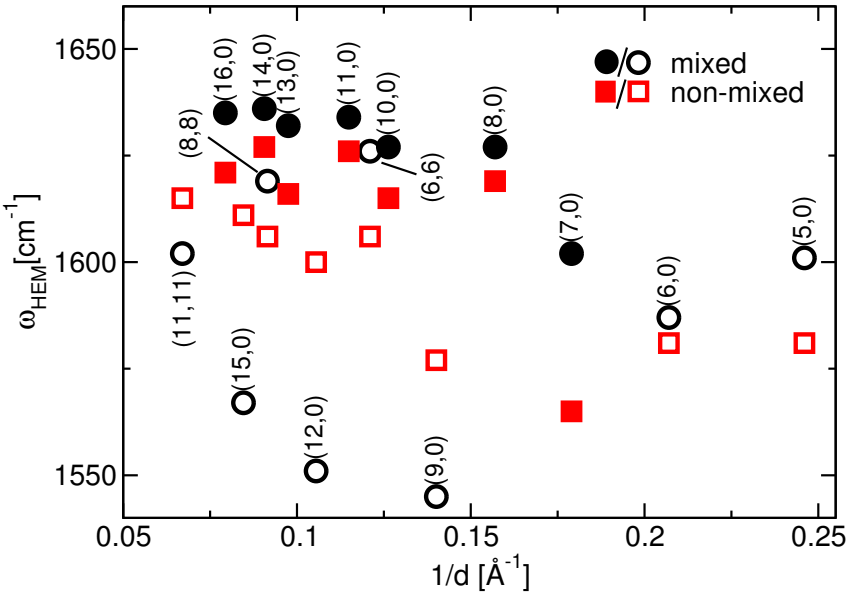

Figure 4.14.: Frequency ω_{HEM} from finite-differences calculation (black symbols) and for the non-mixed frozen-phonon calculation (red symbols). Open (closed) symbols denote metallic (semiconducting) NTs. The frozen-phonon calculation underestimates the frequency, except for most metallic zigzag NTs.

the relative abundances of particular chiralities are not strictly proportional to signal size [127].

In the assumption of small perturbations $\mathbf{u}_a$ the electron-phonon matrix element $\mathcal{M}_j^i$ for the j-th optical transition and phonon i can be obtained from [118, 128]

$$\mathcal{M}_j^i = \sqrt{\frac{\hbar}{2MN\omega^i}} \sum_a \epsilon_a^i \frac{\partial E_j(\mathbf{k})}{\partial \mathbf{u}_a}, \tag{4.2}$$

where a denotes the atom in the unit cell, $\mathbf{k}$ and j correspond to the wavevector and band index of the electronic state. M is the atomic mass, ϵ_a^i is the polarization vector of the phonon, which was normalized to satisfy $\sum_a \epsilon_a^i \epsilon_a^j = \delta_{ij}$. The deformation potential $\partial E_j(\mathbf{k})/\partial \mathbf{u}_a$ for the displacement patterns was obtained in a frozen-phonon approach from the difference of conduction and valence band energy $\partial E_j(\mathbf{k})/\partial \mathbf{u}_a = \partial(E_j^C(\mathbf{k}) - E_j^V(\mathbf{k}))/\partial \mathbf{u}_a$.

All calculations in this chapter are performed in a single-particle picture, *i. e.*, there is no electron-hole interaction. However, the Raman process in carbon nanotubes is governed by the interaction of excitons and phonons [122, 129]. We expect the excitonic states follow the single-particle band changes. Thus the below calculated electron-phonon coupling matrix elements should constitute an approximation to the exciton-phonon coupling matrix elements.

Results From the deformation potentials the matrix elements $\mathcal{M}_j^i$ were obtained for the HEM and RBM without mixing. We find an increase for the deformation potential $\partial E_j(\mathbf{k})/\partial \mathbf{u}_a$ and

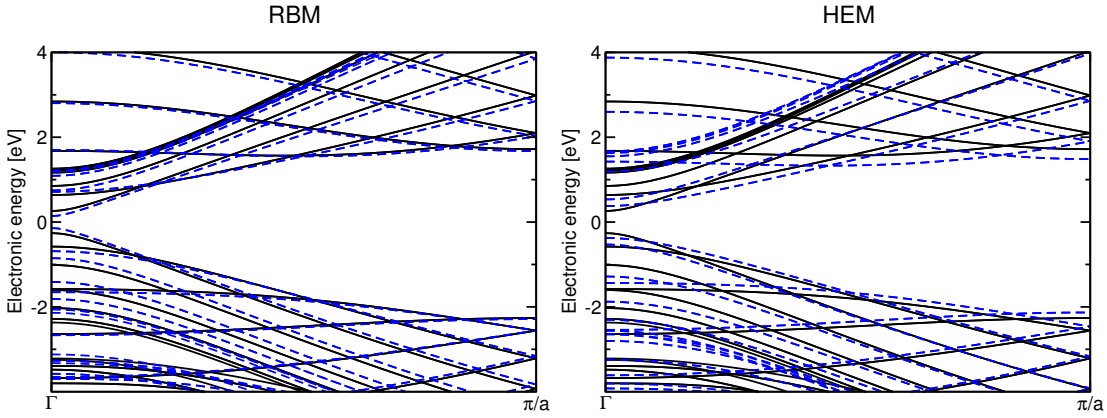

Figure 4.15.: Electronic bands of a (16,0) nanotube for relaxed configuration (black, solid lines) and displaced according to a RBM (left) and HEM (right) phonon (blue, dashed lines). As phonon amplitude $|\mathbf{u}_a|$ the values 0.15 Å(RBM) and 0.02 Å(HEM) were used.

for the matrix elements for the radial displacement pattern between 30 and 60 % compared to the results of Ref. 118 which include the mixing. This is of special interest as the intensity observed in Raman experiments is proportional to the square of $\mathcal{M}_j^i$. The mixed eigenvectors thus yield systematically smaller Raman signals than the assumption of a purely radial mode would suggest.

The change of $\partial E_j(\mathbf{k})/\partial \mathbf{u}_a$ depends on chirality and whether the tube is semiconducting or metallic. In Tab. 4.1 we show the relative increase compared to the values of the mixed eigenvectors in Ref. 118. For semiconducting zigzag NTs, the average of the matrix elements increases by 50 %, whereas for metallic zigzag NTs an increase of 30 % is found. For armchair NTs an increase of between 30 to 40 % is found.

Table 4.1.: Increase of the matrix elements (for the RBM) of the i-th optical transition of the non-mixed radial displacement compared to the matrix elements that include a mixing (shown in Fig. 4.16). The simplified, non-mixed eigenvectors predict systematically larger matrix elements than the mixed ones for all NTs.

NT	$i=1$	$i=2$	$i=3$	$i=4$
(10,0)	1.43	1.58	1.46	1.46
(6,6)	1.36	–	–	–
(8,4)	1.34	–	1.34	–
(8,8)	1.37	1.36	1.36	–
(14,0)	1.51	1.46	1.48	–
(15,0)	1.27	1.35	1.32	1.25
(16,0)	1.45	1.51	1.47	–
(11,11)	1.31	1.36	1.37	–

The matrix elements of the RBM are reduced by the mixing for all NTs. This is surprising, since the relative sign of $\mathcal{M}_j^{\mathrm{HEM}}$ and $\mathcal{M}_j^{\mathrm{RBM}}$ depends on chirality (see Ref. 130). This can be

TABLE I. Calculated diameters, RBM frequencies, and electron-phonon matrix elements $\mathcal{M}_{e\text{-}ph}$ (in eV) for the first optical transitions (*ab initio* calculated energies in eV in parentheses[22]). The matrix elements (boldface for zigzag tubes) were rounded to 0.001 eV. Rows labeled $\mathcal{M}_{1\text{–}4}$ correspond to the first four optical transitions for light polarized parallel to the nanotube axis. A "—" indicates a lack of the transition or a band shift which could not be evaluated for technical reasons. Note that $\mathcal{M}_{e\text{-}ph}$ is normalized to the unit-cell volume V_c.

	(6,0)	(10,0)	(6,6)	(8,4)	(11,0)	(8,8)	(14,0)	(15,0)	(16,0)	(17,0)	(11,11)	(19,0)
V_c(Å^3)	77.2	210	130	626	254	230	406	467	534	603	436	755
d(Å)	4.8	7.9	8.2	8.4	8.7	10.9	11.0	11.8	12.6	13.4	15.0	15.0
ω_{ph}(cm^{-1})	446	287	278	274	257	209	203	188	179	170	151	149
$\mathcal{M}_1$	**0.050**	**–0.028**	–0.015	–0.013	**0.021**	–0.010	**0.016**	**–0.022**	**–0.017**	**0.014**	–0.005	**–0.015**
	(1.0)	(0.8)	(2.3)	(0.8)	**(0.9)**	(1.8)	(0.7)	(1.5)	(0.6)	(0.6)	(1.4)	(0.5)
$\mathcal{M}_2$	**–0.062**	**0.017**	—	0.004	**–0.028**	–0.015	**–0.020**	**0.013**	**0.013**	**–0.016**	–0.010	**0.012**
	(1.7)	(2.0)		(1.7)	**(1.3)**	(3.1)	(1.1)	(2.0)	(1.2)	(1.0)	(2.5)	(1.0)
$\mathcal{M}_3$	—	**–0.030**	—	–0.016	**–0.028**	–0.017	**–0.021**	**–0.022**	**–0.018**	**–0.017**	–0.012	**–0.016**
		(2.4)		(2.6)	**(2.6)**	(3.7)	(2.4)	(2.6)	(1.9)	(2.1)	(3.3)	(1.6)
$\mathcal{M}_4$	—	**–0.031**	—	—	**–0.028**	—	—	**–0.022**	—	**0.009**	—	**–0.016**
		(3.0)			**(3.1)**			(3.2)		(2.4)		(2.7)

Figure 4.16.: Matrix elements $\mathcal{M}_i$ for the first four optical transitions (i=1...4). Taken from Ref.118.

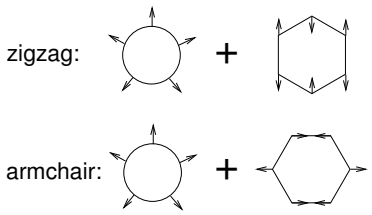

Figure 4.17.: Figure illustrating the mixing between the radial and the tangential components of the RBM in zigzag and armchair NTs when the radial component points outwards.

clarified by looking at the relative orientation of the HEM- and RBM-like components, which is also chirality dependent. We illustrate this in Fig. 4.17. In zigzag nanotubes, when the radial component points outwards, the bonds parallel to the axis are elongated. In armchair NTs the equivalent bonds (that are now perpendicular to the axis) are shortened instead. Thus, the different orientation of both components compensates the opposite sign of the matrix elements, yielding the same trend for all NTs.

In contrast to the RBM, the mixing of the HEMs only little influences their deformation potentials. The deformation potentials of the non-mixed HEM does not show any detectable difference for zigzag tubes; for armchair NTs we find an increase of the matrix elements of $4--7\,\%$ for the non-mixed modes compared to the results in Ref. 124, which include the mixing. The small influence of the mixing on the deformation potential is due to the low electron-phonon coupling strength of the RBM relative to the HEM.

5. CdSe nanowires

Direct band-gap semiconductor nanostructures possess size-dependent optical and electronic properties. This allows a tailoring of the electronic band gap and represents a huge potential for applications. Controlling of the growth kinetics of the II-IV semiconductor CdSe [131] results in nanostructures of various shapes, from nanospheres to nanorods with well defined diameters and aspect ratios [132]. Improved growth techniques nowadays allow the synthesis of semiconductor nanocrystals into rod shaped structures with defined sizes and narrow size distributions. An example are colloidal CdSe nanorods that are synthesized in solution. Up to now diameters below 2 nm with aspect ratios of 5:1 have been reported [133] and higher aspect ratios of up to 20:1 for only slightly larger diameters of 3 nm were synthesized [134]. The nanorods demonstrate a size-dependent photoluminescence that covers the visible spectrum [135, 136]. There has been a considerable effort in understanding the electronic and optical properties of such nanostructures from theory [135, 137] and experiments [135, 138, 139]. In contrast, little is known about their vibrational properties and, surprisingly, of bulk CdSe, either. The phonon dispersion of wurtzite CdSe is available from experiments only in the Γ-A direction [140]. The strong neutron-absorption of ^{113}Cd that is contained in natural Cd makes neutron scattering experiments impossible. The authors of Ref. 140 therefore have grown a sample with weakly absorbing ^{116}Cd and natural Selenium. Another possibility would be to use inelastic X-ray scattering as described in Sec. 3.2.

A wide variety of physical properties of solids depend on their lattice-dynamical behavior such as infrared or Raman spectra or specific heat and heat conduction [15]. The lattice vibrations in nanostructures can, in a first approximation, be estimated from the bulk phonon dispersion within the zone-folding approach [141]. Therefore the bulk phonon dispersion of CdSe will be presented in Sec. 5.2. However, surface effects like a lowering of the coordination number, effects from a surface reconstruction or a realistic surface passivation with adatoms are not covered by such models. Thus *ab-initio*-calculations will also be employed to investigate the structural, elastic, electronic, and vibrational properties of CdSe nanowires. Similar samples, *i. e.*, nanorods with aspect ratios between 6 to 12 are available, too. These CdSe nanorods are experimentally investigated with Raman spectroscopy. This provides an excellent symbiosis of theory and experiment.

One of the major breakthroughs was the experimental verification of a radial-breathing-mode in CdSe nanorods. This mode was predicted beforehand by our calculations and observed in

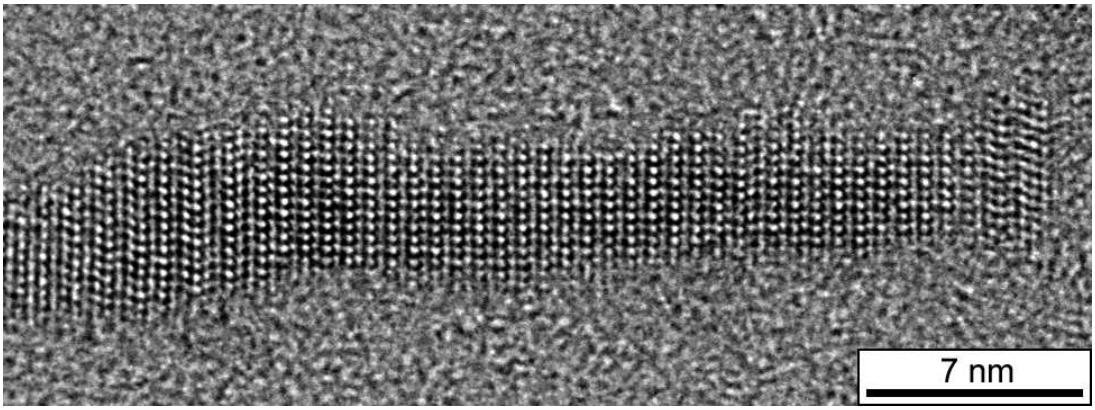

Figure 5.1.: High-Resolution transmission electron microscope micrograph of a CdSe nanorod. The micrograph was recorded by Dr. Tore Niermann, TU Berlin, with a Philips CM200-FEG-UT operated at 200 kV.

Raman experiments.* It will be discussed in section 5.4.3.

The possibility to coat CdSe nanorods with an epitaxial shell of a larger band gap material, like ZnS, is an important enhancement for applications. In this context the transformation from a type-I heterojunction into a type-II one was shown: From the band lineup one finds for CdSe/ZnS superlattices type-I heterojunctions, where the large band gap of ZnS completely encloses the small band gap of CdSe [142]. However, a thin shell of ZnS around the CdSe nanowires results in a type-II heterojunction. This will be discussed in section 5.4.

5.1. Introduction

5.2. Bulk CdSe

Bulk CdSe exists in three different crystal structures: a metastable cubic zincblende structure, a cubic sodium chlorite structure, which exists only at pressures higher than 3GPa and a stable hexagonal wurtzite structure. [143] The wurtzite structure is shown in Fig. 5.2(a). Each Cd atom is surrounded by 4 Se atoms and vice versa. The Brillouin zone with the high-symmetry points and lines is shown in Fig. 5.2(b). It is the same Brillouin zone like that of graphite introduced in section 3.1. In addition to covalent binding, there is a strong ionic binding due to the different electronegativity of the two materials. This ionic binding results in electric dipoles leading to distinct phonon modes. This so-called LO-TO splitting will be discussed later.

Details of the calculation of CdSe Cd has the atomic configuration $[\mathrm{Kr}]4d^{10}5s^2$ and belongs to the transition metals. Before creating a good pseudopotential one has to consider, which

*The Raman spectra of the CdSe nanorods in this chapter were recorded by Dr. Holger Lange, current affiliation TU Berlin.

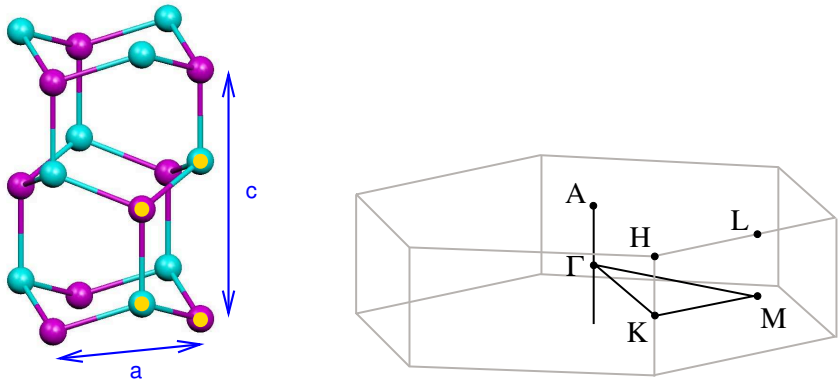

(a) Wurtzite structure **(b)** Hexagonal Brillouin zone

Figure 5.2.: (a) Crystalline structure of wurtzite CdSe. The primitive unit cell is indicated by yellow circles. a and c denote the lattice parameters. Cd atoms are depicted in magenta and Se atoms in cyan. (b) The corresponding Brillouin zone with the high-symmetry points and lines.

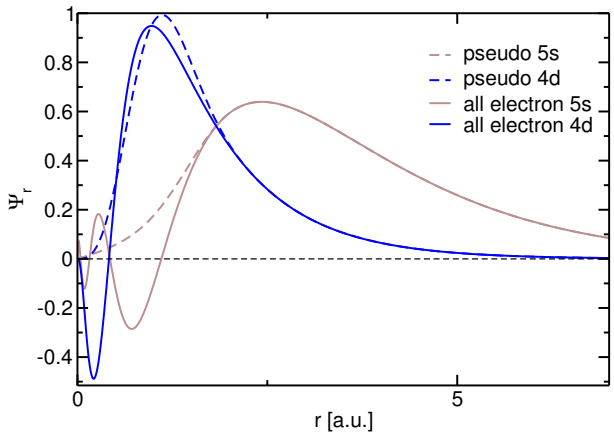

Figure 5.3.: Radial part of the all-electron and pseudo wave function for the Cd $4d$ and $5s$ states

electrons to put into the valence and core states. Putting the $4d$ into the valence state results in a 6-times higher number of electrons. As electronic structure calculations scale by the order of 3 with respect to the number of electrons taking the $4d$ electrons in to account results in much longer calculations. When plotting the all-electron wave function, it can be seen that the $4d$ wave function overlaps with the $5s$ state (see Fig. 5.3). This indicates that a pseudopotential with only the $5s$ states as valence states would be a bad approximation. To investigate this, well-tested analytical pseudopotentials from Hartwigsen, Goedecker and Hutter were used that are available in both flavors: $4d^{10}5s^2$ and only $5s^2$ with semicore-correction. [144] Structural differences are small between both flavors, *i.e.*, lattice constants differences were found to be 0.6 %. However, optical phonon frequencies were underestimated by up to 40 cm^{-1} if only the $5s$ electrons are considered. This clearly forbids the use of semicore pseudopotentials for Cd in this work. For the Se pseudopotential the configuration $4s^24p^4$ was used. The norm-conserving

pseudopotentials were generated with the Troullier Martins scheme [101] with the following core radii in Bohr: Se $4s^2$ (1.89) $4p^4$ (1.89), and Cd $5s^2$ (2.18) $4d^{10}$ (2.5). The valence electrons were described by a double-ζ basis set plus an additional polarizing orbital. The localization of the basis followed the standard split scheme and was controlled by an internal SIESTA parameter, the energy shift, for which a value of 50 meV was used. This resulted in basis functions with a maximal extension of 3.45 Å(Se) and 4.13 Å(Cd). Real space integrations were performed on a grid with a fineness of 0.16 Å, which can represent plane waves up to an energy of 120 Ry. Integrations in reciprocal space were performed on a $(6 \times 6 \times 4)$ Monkhorst-Pack mesh [121].

As a prelimiminary test for the quality of the pseudopotentials the bulk modulus was calculated. It is defined as the pressure increase needed to achieve a given decrease in volume. This quantity usually gives a good estimate for the quality of the pseudopotential w.r.t. the elastic properties of the system. This includes a good estimate for the quality of phonon frequencies. Technically, the bulk modulus was obtained in the following way: the total energy of the system was calculated at different lattice constants around the relaxed values and fitted with the Murnaghan equation of state (see. Appendix B). A bulk modulus of 55.54 GPa was obtained, in good agreement with the experimental value of 53.4 GPa [145]. The lattice parameters for wurtzite CdSe yielded a=4.34 Å and c=7.09 Å, both in good agreement with experimental values of a=4.2999 Å and c=7.0109 Å [140]. The overestimation of the lattice constant can be attributed to the large extension of the basis functions used that are more extended than the default value of the energy shift.

Band structure The obtained band structure is shown in Fig. 5.4. An electronic energy of 0 eV corresponds to the valence band maximum. As expected the result shows CdSe to be a direct semiconductor. The conduction band minimum and the valence band maximum lie at the Γ-point. The band gap from our calculations is 1.13 eV. The experimental value is 1.73 eV [146]. This difference can be accounted for using the scissor's operator [147].

Phonon dispersion The phonon dispersion of bulk CdSe was calculated.[†] For the calculation of the phonon dispersion material linear response theory was used, which is implemented in ABINIT [148, 149]. The exchange correlation functional of Perdew and Wang was used in the local density approximation. [7]. The valence electrons were expanded in a plane wave basis with an energy cutoff of 30 Hartree. A shifted $10 \times 10 \times 4$ sampling grid was used for the integration over the Brillouin zone. The dynamical matrix was calculated on a $10 \times 10 \times 4$ q-grid. Force constants were obtained via a Fourier transformation and interpolated to obtain phonons at arbitrary points in the Brillouin zone. The convergence of the chosen q-grid was validated: a

[†]This is the only part in this chapter where another code than the SIESTA code was used, because it is not capable of calculating 2nd-order derivatives of the total energy. If we had used a supercell for achieving the same amount of accuracy it would have been a $10 \times 10 \times 4$ super cell with 1600 atoms.

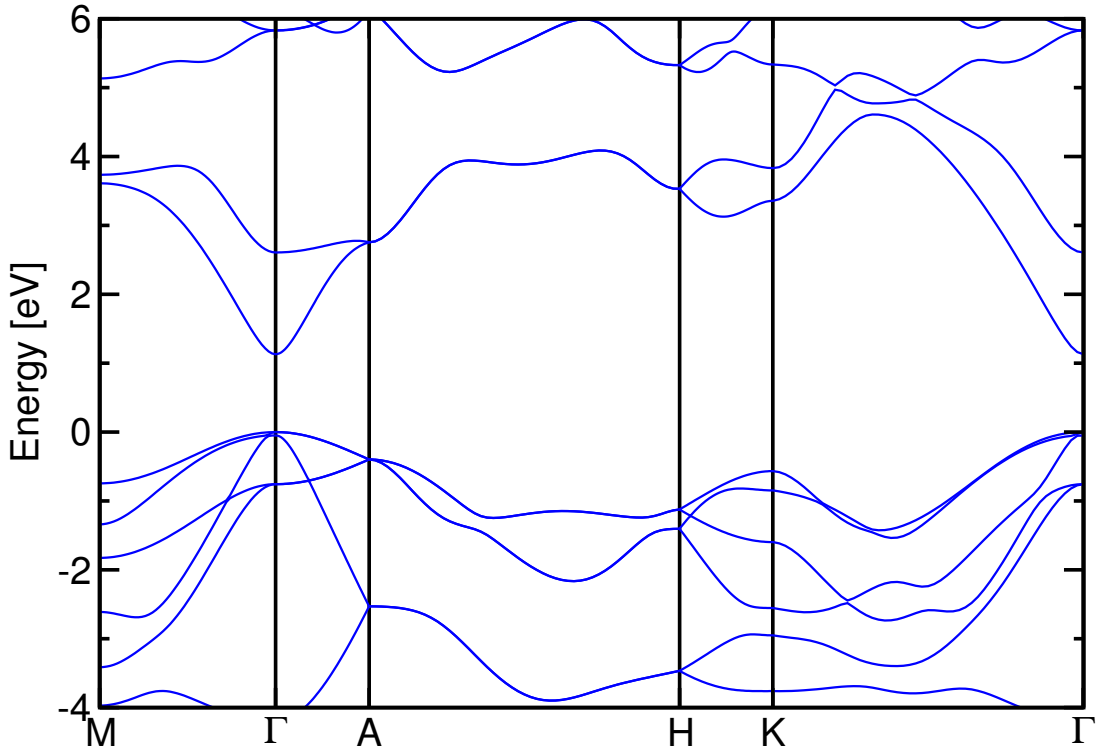

Figure 5.4.: Electronic band structure of wurtzite CdSe along the high-symmetry lines.

$10 \times 10 \times 4$ q-grid leads to a difference in frequencies of less then $1\,\mathrm{cm}^{-1}$. The lattice parameters for wurtzite CdSe obtained with ABINIT were a=4.29 Å and c=7.00 Å, again in good agreement with experimental values of a=4.2999 Å and c=7.0109 Å [140]. As further test the bulk modulus was calculated to 55.58 GPa, in good agreement with the experimental value of 53.4 GPa [145].

The splitting of the LO and TO phonons was calculated with the standard model [150,151].It depends on the dielectric high-frequency constant where ABINIT yields a value of $\epsilon_{\infty}^{||} = 7.2$. All calculated frequencies were multiplied by a constant factor to match the experimental bulk LO frequency at the Γ-point.

The bulk phonon dispersion for the high-symmetry directions calculated with ABINIT is shown in Fig. 5.5. Also shown are experimental frequencies obtained with INS along the Γ−A direction.

The dispersion along $\Gamma - K$ and $\Gamma - M$ shows an overbending near the Γ-point, which can be found in other crystals with hexagonal structures as well [68,152,153]. When treating vibrations with the zone-folding approximation, the existence and the strength of an overbending in the dispersion is of importance [154,155]. When the size is reduced and confinement effects become important, phonons that do not stem from the Γ-point also contribute to the first-order Raman spectrum. This softening of the $q = 0$ selection rule is known for nanostructures [156]. The calculated phonon dispersion was used to estimate the frequency ω_{LO} of the LO mode in CdSe

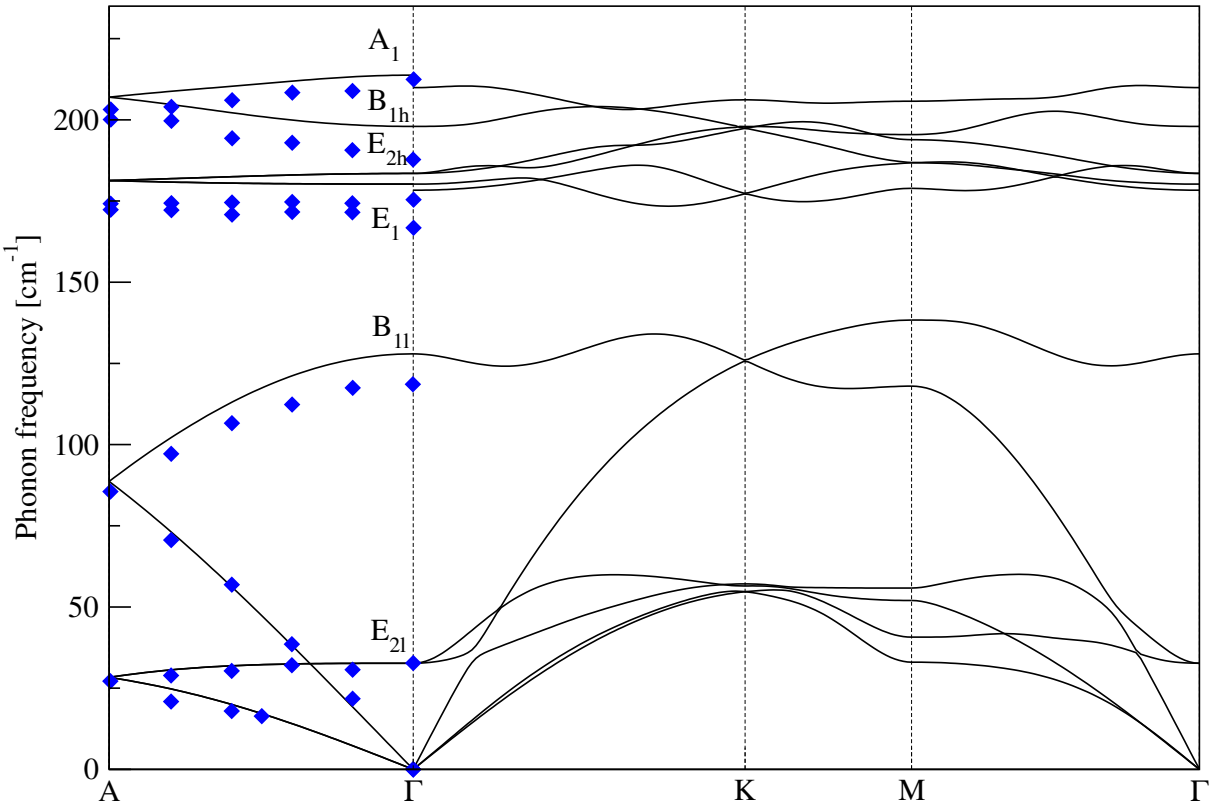

Figure 5.5.: Phonon dispersion curves for bulk CdSe, calculated with ABINIT (solid lines). Diamonds are experimental values from Ref. 140. They were multiplied by $\sqrt{(116/112.4)}$ to account for the use of ^{116}Cd isotope instead of natural Cd with an atomic weight of 112.4 U [140].

nanorods by Holger Lange and co-workers in Ref. 155. This result is shown in Fig. 5.6. The s-shape is a result of the overbending of the highest branch along the $\Gamma - M$ and $\Gamma - K$-directions. The agreement with the experimental data is excellent.

5.3. CdSe nanowires

Using plane waves as basis functions usually is the best choice when studying new materials. One of the advantages of plane waves is their convergence behaviour: Increasing the number of plane waves, *i.e.*, taking into account plane waves with smaller wavelength respective higher energy, results in a more accurate description. The convergence criterion is imposed and easily determines the number of used plane waves.

For large unit cells, as required by one-dimensional systems, however, plane wave basis sets are computationally very expensive.[‡] For these systems localized basis sets are preferable. These are

[‡]During the creation of this PhD thesis, the package BigDFT has been developed. It is now implemented in ABINIT. BigDFT uses wavelets which are similar to plane waves but with a finite extension. In addition, the grid-points for integration are divided into a coarse-fine grid. These two improvements allow the calculation

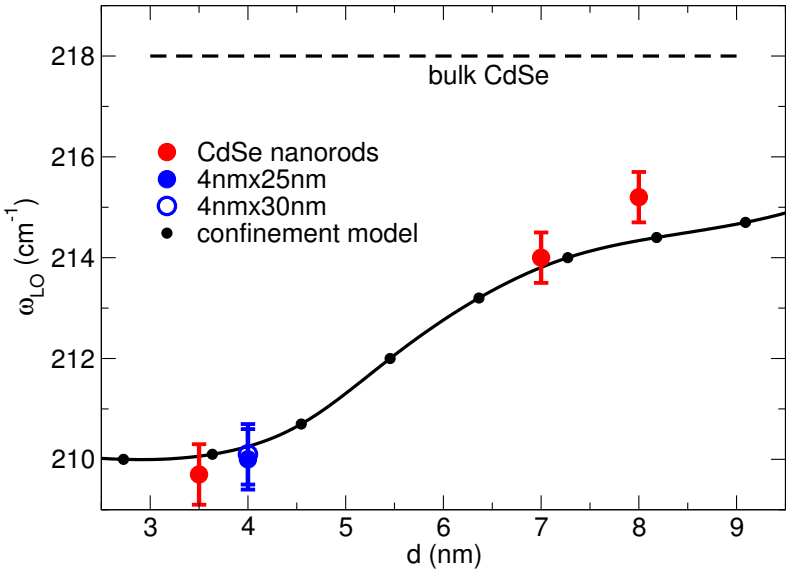

Figure 5.6.: Frequency of the longitudinal optical phonon versus nanorod diameter. Calculated positions are from a confinement model, which uses the phonon dispersion shown in Fig. 5.5. The bulk dispersion shows an overbending near the Γ-point. The slope near the Γ-point determines the direction and amount of shift of ω_{LO} and is responsible for the s-like shape. Taken from Ref. 155.

used in SIESTA, the code which was used for the calculation of NWs. SIESTA uses strictly-confined atom-centered numerical basis functions [9, 102]. The strict confinement ensures that the matrix elements between non-overlapping basis functions are zero and not stored during the calculation.

Calculational details The NWs were generated by cutting out appropriate discs of a wurtzite crystal. The center of the discs was either placed in the middle of a hexagon or an atom. All atoms within a cutoff radius were then added to the unit cell. The cross sections of the relaxed unit cells are shown in Fig. 5.7. Surface atoms have a lower coordination number and dangling bonds can occur. A widespread method to prevent such unwanted effects is to passivate surface atoms by H-atoms or OH-groups. For computational reasons H-atoms were chosen for the passivation and two sets of NWs one without and one with a H-passivated surface were compared. All pseudopotentials were generated with the Troullier-Martins scheme [101] for the following valence-state configurations: Se $4s^2\,4p^4$, Cd $5s^2\,4d^{10}$. As exchange correlation functional the local density approximation was used in the parameterization of Perdew and Zunger [6]. The valence electrons were described by a double-ζ basis set plus an additional polarizing orbital. The localization of the basis followed the standard split scheme and was

of nanostructures with much smaller memory and CPU time resources. The current version of ABINIT only allows the use of BigDFT for molecules or systems with only the Γ point, however developers around A. Neelow are currently extending it to 1D-systems.

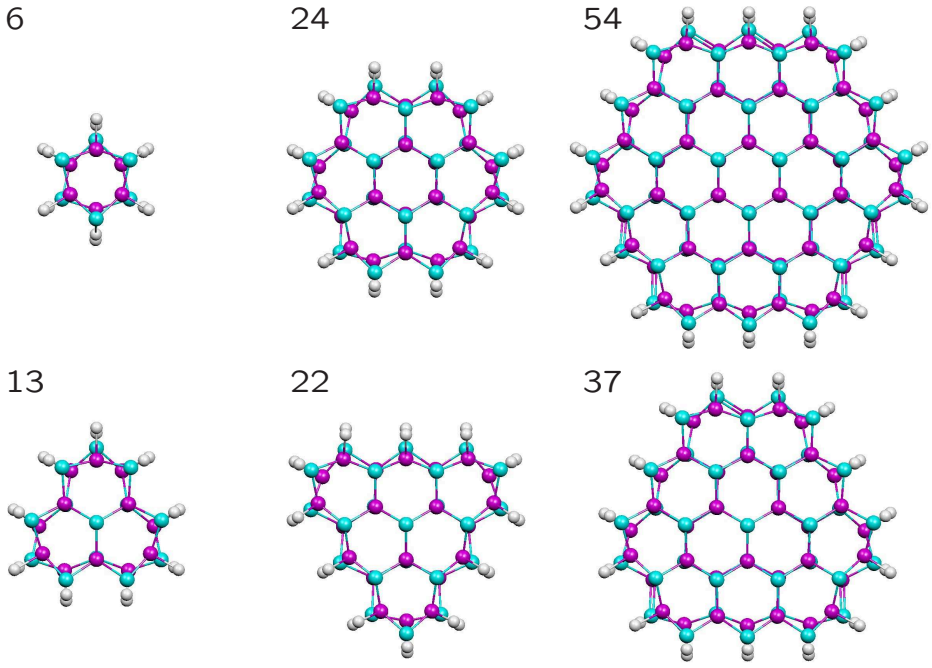

Figure 5.7.: Unit cells of the calculated NWs (shown here with a hydrogen coating). The number n of CdSe-pairs per unit cell is indicated, thus $(CdSe)_n$ uniquely identifies the nanowire. Near the surface, the Cd atoms (magenta, dark) move more inwards, compared to the bulk region [159].

controlled by the energy shift, for which a value of 50 meV was used. This resulted in basis functions with a maximal extension of 3.45 Å(Se), 4.13 Å(Cd) and 3.2 Å(H). Periodic images of the NWs were separated by at least 20 Å. Real space integrations were performed on a grid with a fineness of 0.2 Å, which can represent plane waves up to an energy of 80 Ry. Higher values do not change the total energy by more than 1 meV/atom. At least 16 k-points, equally spaced along the 1D Brillouin zone, were used for integrations in reciprocal space. The phonon calculations were performed with the method of finite-differences [13]. For the calculation of the LO splitting we used the experimental dielectric high-frequency constant $\epsilon_{\infty}^{||} = 6.0$ [157] and a modified version of the vibrator code, described in Ref.158.

A CdSe crystal was also calculated with SIESTA using a $10\times10\times4$ k-point grid and otherwise the same parameters as for the NWs. The lattice parameters for wurtzite CdSe yield a=4.34 Å and c=7.09 Åin good agreement with experimental values [140]. As bulk modulus a value of 55.54 GPa was obtained in good agreement with the experimental value of 53.4 GPa [145].

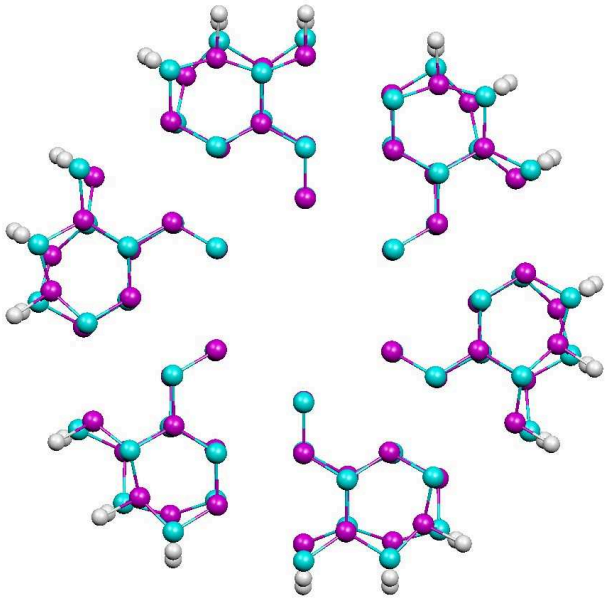

Figure 5.8.: Scheme to illustrate the iterative relaxation. The whole unit cell is generated by symmetry operations from the small slice. The rotation by 60° follows a translation of $c/2$.

5.3.1. Symmetry considerations

Symmetry considerations largely help to reduce the calculation time. Ground state calculations scale by the order of 3 with the number of electrons. Additionally for a phonon calculation each atom has to be displaced separately. Thus phonon calculation roughly scale by the order of 4 with the number of atoms in the unit cell. The largest wire considered here, lasted 1 month on our computer cluster. Without the use of symmetries, the calculation time would have been six times higher.

Every one-dimensional system can be described in terms of line groups, a one-dimensional analogon to space groups. In contrast to space groups line groups allow the application of arbitrary rotations [110]. The NWs from Fig. 5.7 with a hexagon in the center (upper row) belong to the line group $L(6)_3mc$ that has the generator $\{C_6|\mathbf{t}/2\}$. This corresponds to a screw axis. The NWs from Fig. 5.7 with atoms in the center (lower row) belong to the line group $L3m$ that has the generator $\{C_3|0\}$. The force constants were only calculated for the irreducible part of the unit cell. For the remaining atoms, the force constants were determined by symmetry.

Iterative symmetry based relaxation

Symmetries were used to reduce internal stresses in the unit cell that may occur in large systems during the relaxation process. Most routines only regard atomic forces during relaxation, however stresses may appear by cancelling out of two or more forces. To reduce this a symmetry based, iterative relaxation method was used: After a NW was relaxed, the whole wire

was generated by applying symmetry operations to the irreducible part of the unit cell (see section A). This symmetry generated unit cell was then relaxed again. This iterative process was repeated until all forces were below $0.02\,\mathrm{eV/Å}$ after generation of the wire. With this method much better results were observed than with a simple relaxation: Frequencies of phonons belonging to two-dimensional representations that should have degenerate frequencies, were separated by less than $0.05\,\mathrm{cm}^{-1}$. This helped to assign the modes into their corresponding one and two-dimensional representations. In contrast, performing a standard relaxation resulted in frequencies of degenerated modes separated by up to $2\ \mathrm{cm}^{-1}$.

5.3.2. Structural properties of NWs

The unit cell length c of the NWs changes with diameter. It also changes with the addition of a hydrogen passivation shell around them. The unit cell length c over the inverse diameter $1/d$ is displayed in in Fig. 5.9. The diameter is defined by the average distance of the outermost Se atoms to the rotational axis. A distinction is made into bare wires (without passivation) and passivated NWs. The bare wires have a larger unit cell parameter c than the passivated NWs. The largest increase of $3.5\,\%$ between bare and passivated wire was found for the $(CdSe)_{13}$ wire (the smallest wire with a three-fold rotational axis) . For the largest wire, the $(CdSe)_{54}$, the increase is $1.7\,\%$. The lattice parameter c varies with the diameter d. A linear relationship is found, which is best described by the parameters $c_{\mathrm{NW}}(d) = c - m/d$ with the bulk lattice constant $c = 7.09\,\mathrm{Å}$ and $m = 3.25\,\mathrm{Å}^2$ (passivated) and $m = 1.74\,\mathrm{Å}^2$ (bare) NWs.

The most dramatic changes in the atomic structure happen near the surface. The surfaces of all calculated NWs undergo a reconstruction. During this reconstruction [159, 160] the Cd-atoms rotate into the surface to lower the energy as can be seen in Fig. 5.7. The passivation with hydrogen atoms does not change qualitatively this reconstruction. In Fig. 5.10 the bond length deviations for two nanowires is plotted. The CdSe bonds show a broad distribution in lengths. In the core the bond lengths deviate from the bulk value by $< 1\,\%$, while those on the surface change by up to $3\,\%$. After the first monolayer of CdSe the bond length of bulk CdSe is nearly restored.

5.3.3. Electronic properties

As mentioned in Sec. 5.2 bulk CdSe has a direct electronic band gap. It is known from absorption or photoluminescence measurements that the band gap of CdSe nanocrystallites and NWs shows a strong size dependence [135]. In Fig. 5.11 the electronic band structure and the density-of-states (DOS) is plotted of the wires I and II from Fig. 5.10. Both rods have a direct band gap. That of wire I is significantly larger than that of wire II. In Fig. 5.12 the band gap increase is shown compared to the bulk value as function of the inverse diameter. It can be seen that the passivation influences the electronic band structure: passivated NWs have larger band gaps than

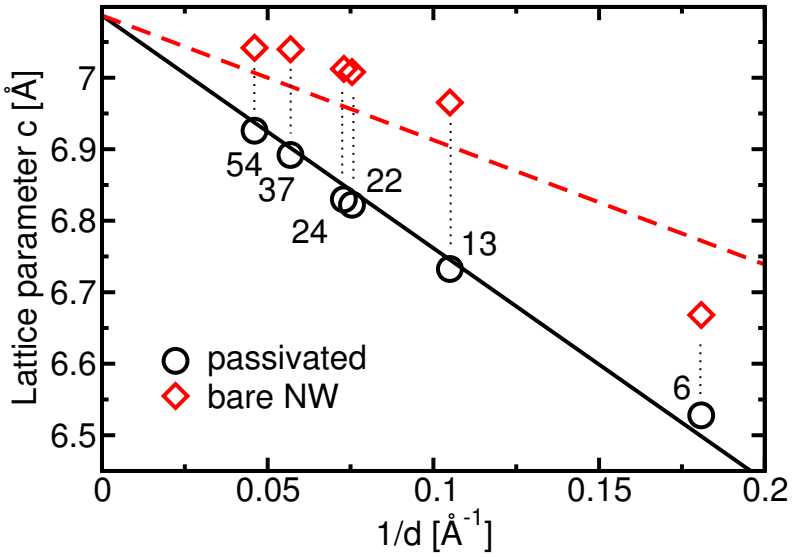

Figure 5.9.: Evolution of the lattice parameter c of the NWs with and without H-atoms. Bulk CdSe is considered at an inverse diameter of $0\,\text{Å}^{-1}$. The number close to the symbols indicates the number of CdSe-pairs in the unit cell.

their unpassivated counterparts. At first sight this is a strange behavior as the H-atoms add electronic states to the unit cell that could energetically occupy the band gap region. However, at the same time, the lattice parameter c decreases with the addition of the H-atoms (see Fig. 5.9). This leads to a stronger confinement and is the stronger effect. The confinement increases, which leads to a net increase of the band gap.

The data from the wires with passivation is in good agreement with the semiempirical pseudopotential calculation (SPC) data from Ref. 135, also displayed in Fig. 5.12. Their pseudopotentials were optimized to fit the experimental data.

5.3.4. Vibrational properties

We now concentrate at the changes in the vibrational spectrum. Because the full phonon dispersion for NWs was not available a histogram is used. This normalized histogram of the Γ-phonons of the largest NW [the $(CdSe)_{54}$] is plotted into the bulk phonon density of states (DOS) in Fig. 5.13. Acoustic modes below $75\,\text{cm}^{-1}$ are shifted to higher frequencies, whereas the optical modes around $200\,\text{cm}^{-1}$ are red-shifted. This is a general trend, *e.g.*, reported by Sun for investigating bond-order deficiencies in nanowires [156]. Additionally, optical modes in NWs are found with frequencies higher than the LO-mode in the bulk: These modes vibrate mainly on the surface, their frequency exceeding the bulk LO by at most $15\,\text{cm}^{-1}$. The reason for this increase lies in the higher coordination of the reconstructed Cd atoms as an inspection of the force constants for the outermost Cd atoms shows. The sum of the forces on this atom when slightly displaced from the relaxed position is by 4 % higher than that of an Cd atom in

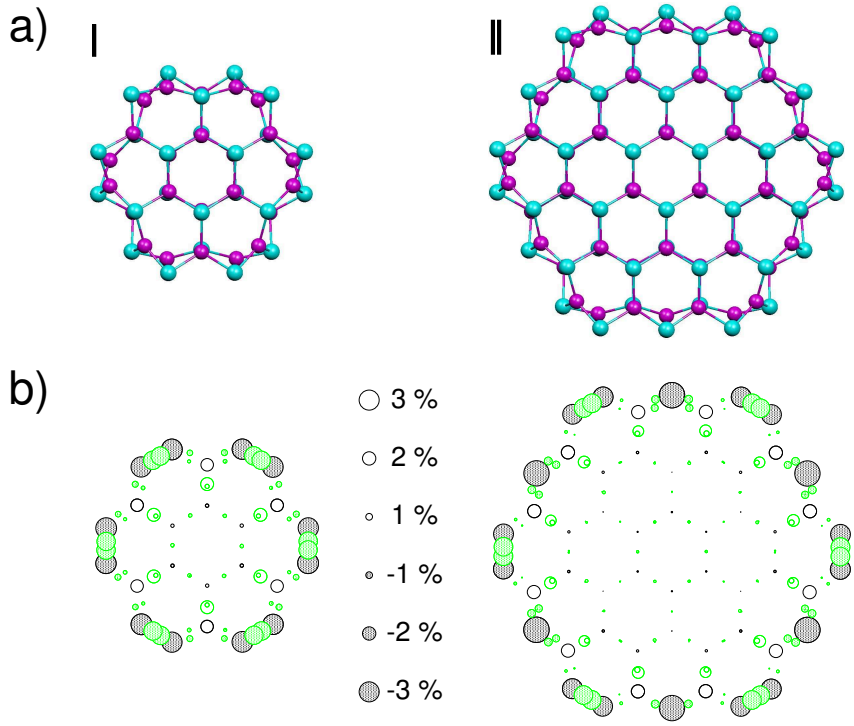

Figure 5.10.: (a) Cross sections of the CdSe nanowires and (b) bond length deviations compared to bulk CdSe. Black circles correspond to axial bonds and green circles to lateral bonds.

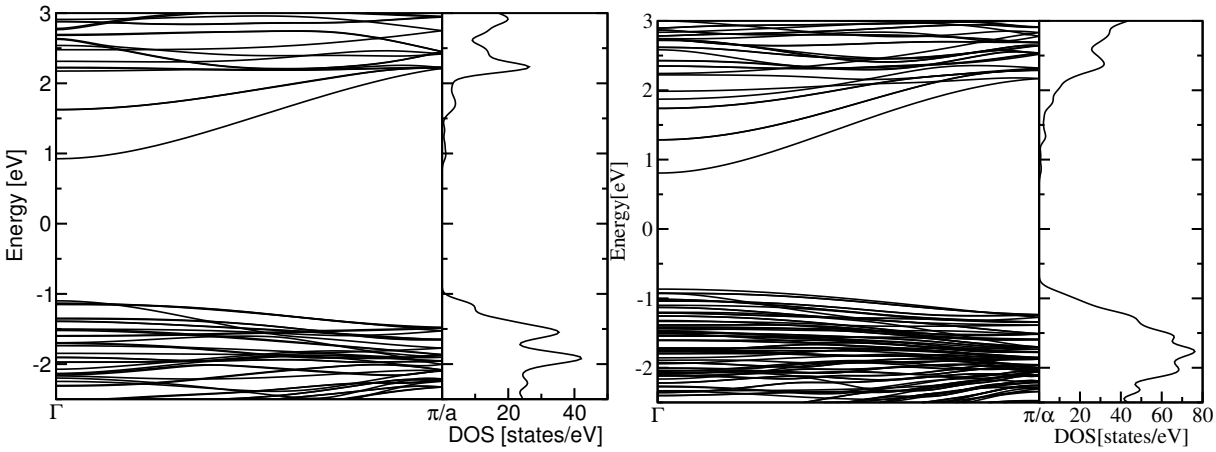

(a) Wire I **(b)** Wire II

Figure 5.11.: Band structure and density of states, with Gaussian broadening of 0.1 eV for the two wires shown in Fig. 5.10.

in the center. Force constants of atoms lying in the 2nd layer or closer to the rotational axis do not significantly differ from those in the bulk. This is similar to the subsurface modes predicted for zirconium slabs [161].

We now focus on optical Γ-point phonon modes of bulk CdSe and their corresponding coun-

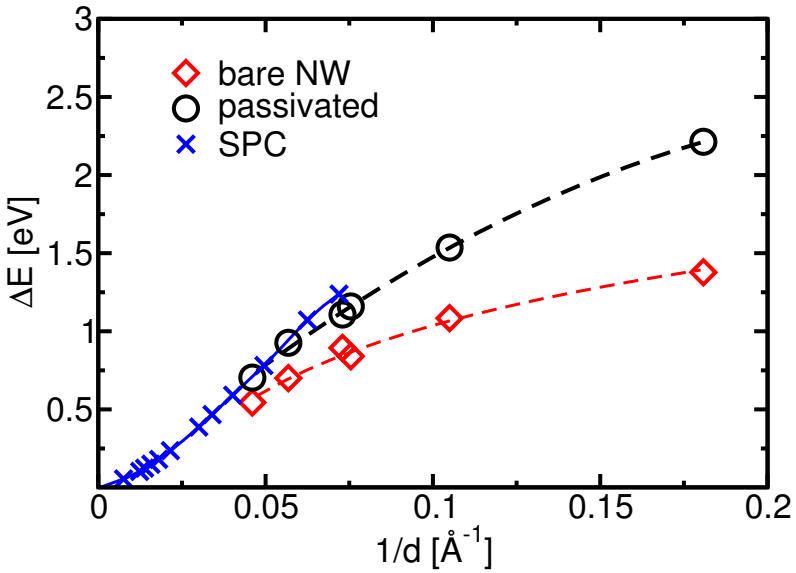

Figure 5.12.: Band gap difference $\Delta E = E_{\mathrm{NW}} - E_{\mathrm{bulk}}$ of the NWs with and without H-passivation. Crosses denote data from semiempirical pseudopotential calculations (SPC) from Ref. 135. Lines are guides to the eye.

terparts in NWs. Frequencies obtained from the wires with passivation do not differ significantly from the bare wires. The evolution in phonon frequency with changing NW diameter is shown in Fig. 5.14, where the phonon-frequency difference between the NW and bulk over the inverse diameter is plotted. All considered bulk modes that belong to one-dimensional representations show a strong systematic redshift for reduced diameters (upper plot) [156]. In contrast, the modes belonging to two-dimensional representations show a smaller size dependence (lower plot). The rigid shift of the E_1-mode will be explained later. This different size dependence has also been predicted for Si NWs in Ref. 163. They find the LO mode with eigenvectors parallel to the NW axis to have a stronger size dependence, than the two TO modes with eigenvectors perpendicular to the axis. This trend is also found in our results, all modes belonging to one-dimensional representations have eigenvectors almost parallel to the wire axis and depend strongly on size.

Polar semiconductors are known to have different frequencies for LO and TO modes at the Γ-point. The reason for this is that long-wavelength longitudinal optical atomic vibration induce a polarization field that contributes to the restoring forces due to the long-range Coulomb interaction. It has been shown that this Coulomb interaction can be treated separately from the short ranged dynamical calculation. In detail, the dynamical matrix can be split into an analytic and a non-analytic part, the latter containing the long-range Coulomb forces. Its evaluation is performed as an Ewald summation [150, 151, 164]. This non-analytic part depends on the unit cell volume and the dielectric high-frequency constant ϵ_∞. In bulk CdSe with an experimental dielectric constant of $\epsilon_\infty^{\parallel} = 6.0$ [157] a splitting of $32\,\mathrm{cm}^{-1}$ is obtained in good

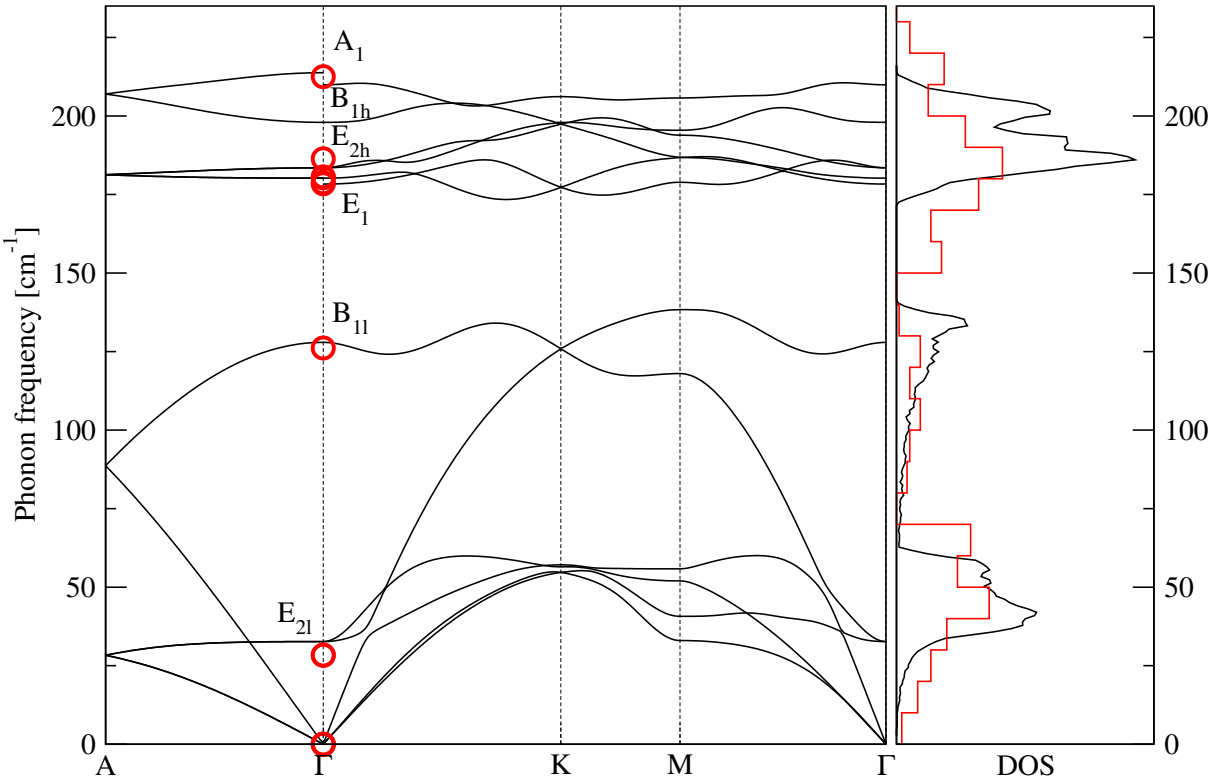

Figure 5.13.: Phonon dispersion curves and DOS for bulk CdSe, calculated with ABINIT (solid lines). Circles are Γ-point frequencies calculated with SIESTA. In the bulk phonon DOS (line) a histogram of the the Γ-point phonons of the bare $(CdSe)_{54}$-wire (stairs) is plotted. The DOS and histogram are normalized.

agreement with the experimental value of $39\,\mathrm{cm}^{-1}$ [140]. The same model is applied to the NWs. The wire cross section times unit cell height is taken as the cell volume. To account for the one-dimensionality only k-vectors along the wire axis contribute to the sum. One obtains a splitting of only a few cm^{-1} for larger wires; much smaller than in the bulk. The underestimated splitting is attributed to the fact that the displacements within the LO mode in the NW are not well ordered. They are parallel only in the NW-core and even anti-parallel near the surface. Consequently the polarization as sum of dipoles becomes weaker compared to bulk. In Fig. 5.14 the energy difference of the A_1-modes is calculated without any contribution from the long-ranged Coulomb interactions, neither for bulk nor NWs. The bulk frequency reference then becomes $177\,\mathrm{cm}^{-1}$. For this mode experimental Raman data is available for nanorods with aspect ratios > 5 and diameters between 4 and 8 nm [165, 166]. A linear fit $\omega_{\mathrm{NW}} - \omega_{\mathrm{bulk}} = m/d$ leads to $m = -149\,\mathrm{cm}^{-1}$ Å. The calculated frequencies of the A_1-modes shown in Fig. 5.14 are in good agreement with the extrapolated experimental fit.

A rigid shift of a mode similar to the E_1-mode was predicted by Fuchs and Kliewer for an ionic crystal slab [162]. They find for the mode with a polarization perpendicular to the slab,

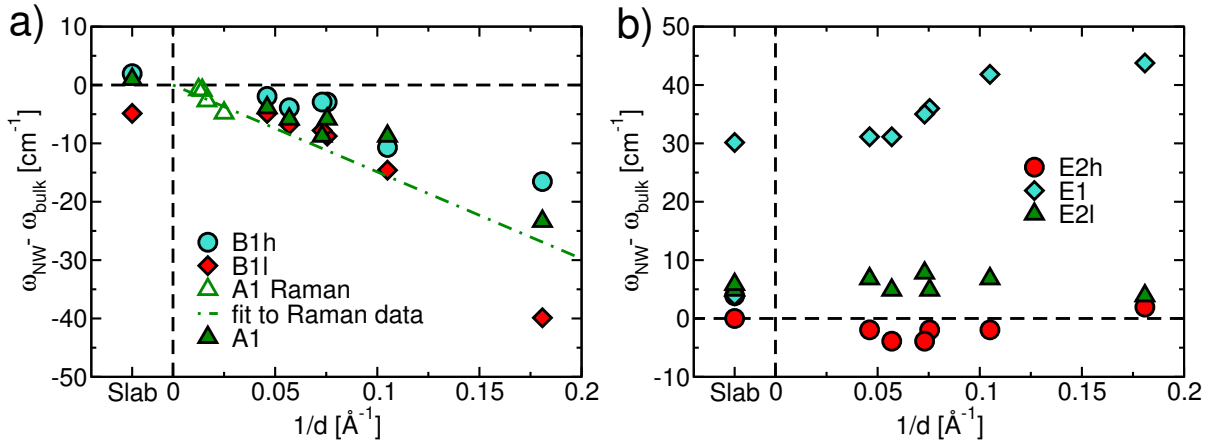

Figure 5.14.: Phonon energy difference $\omega_{\mathrm{NW}} - \omega_{\mathrm{bulk}}$ over inverse diameter for all optical bulk modes. On the left are the modes of a slab with a thickness of 20 Å which corresponds to the diameter of the biggest calculated NW. a) Phonons belonging to 1-dimensional representations. b) Phonons belonging to 2-dimensional representations.

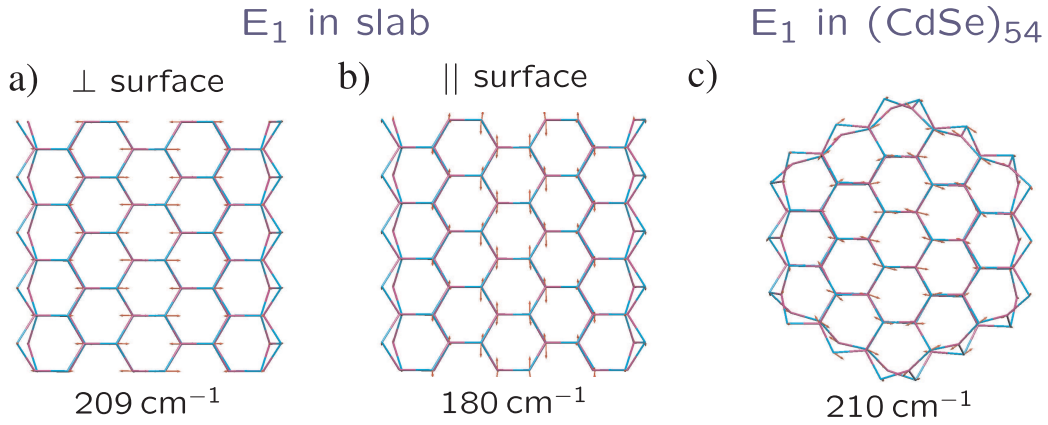

Figure 5.15.: Displacement patterns and energy of the E_1-modes in a slab and in a wire. Characteristic for this mode is the opposite movement of the two sub-lattices of Cd and Se atoms, creating a net polarization stemming from surface contributions [162]: a) in a slab where the atoms move perpendicular to the surface, b) in a slab where the atoms move parallel to the surface, and c) in a wire.

frequencies in the range of the LO-mode in the bulk. In this mode the two sub-lattices of Cd and Se move into opposite directions, creating a net polarization stemming from surface contributions. The corresponding modes in the slab are depicted in Fig. 5.15. These modes are also found when calculating the phonon frequencies of a thin slab with SIESTA. The in the bulk degenerated E_1-mode is lifted into two modes in the slab: One with a polarization perpendicular to the surface and a frequency like the LO in the bulk [as predicted by Fuchs and Kliewer [162]], the other with a polarization parallel to the surface and a frequency of the

E_1-mode in the bulk. In NWs we have surface contributions in all lateral directions for the E_1-mode. This leads to a degenerated E_1-mode again but with a frequency similar to that of the LO mode in the bulk. These E_1-modes also show a size dependence. This can qualitatively be explained by considering that the polarization field generated by the surface contributions becomes weaker for larger diameters and becomes zero in case of the bulk limit.

5.3.5. Radial breathing mode

In carbon nanotubes, details about the exact geometry can be obtained by purely optical measurements. The radial breathing mode in carbon nanotubes corresponds to the atomic vibration of the carbon atoms in the radial direction, as if the tube was breathing (see Fig. 4.3). The RBM's frequency is highly diameter sensitive (see Fig. 4.10). Resonant Raman measurement of the radial breathing mode in nanotubes are used to determine the nanotube diameter and characterize nanotube ensembles. In this way, it is possible to detect single chiralities (n_1, n_2) of carbon nanotubes [95, 96, 167].

The calculations of the vibrational properties of CdSe nanowires reveal the presence of a similar, fully symmetric vibrational mode in the NWs. This mode is strongly diameter sensitive. To prove the existence Raman scattering experiments on a set of colloidal CdSe nanorods and *ab-initio* calculations of the vibrational properties of CdSe NWs were performed. The frequency dependence of a solid cylinder can be estimated from linear elasticity theory. For a long isotropic cylinder the frequency of such a mode is given by [168]:

$$\omega = \frac{2\tau_n}{d}\sqrt{\frac{E(1-\nu)}{\rho(1+\nu)(1-2\nu)}} \tag{5.1}$$

where ν is the Poisson's ratio, and ρ and E are the density and the Young's modulus of the nanowire material. τ_n is the n-th root of the equation $\tau J_0(\tau) = \frac{(1-2\nu)}{(1-\nu)} J_1(\tau)$, where J_m are the Bessel functions of the first kind. The square root in Eqn. 5.1 depends only on the material properties, the diameter dependence of this radial modes' frequency is thus proportional to $1/d$. The same diameter dependence has also been deduced from a Stillinger-Weber-type model for calculated Raman spectra of Si[111] nanowires by Thonhauser and Mahan [169]. Using bulk parameters [32, 170] for Eqn.5.1 results in $C_{el} = 82.8$ cm^{-1}nm for the diameter dependence of $\omega_{\mathrm{RBM}} = C_{el}/d$.

The *ab-initio* calculations reveal a vibrational mode where the atoms move almost radially, which is present in all calculated NWs. This mode is fully symmetric. An exemplary displacement pattern is displayed in Fig. 5.16. The modes' frequency is diameter dependent, resulting frequencies of this RBM range from $40 - 160$ cm^{-1} for a diameter range of $2.6 - 0.6$ nm. As expected from Eqn.5.1, the calculated frequencies show a $1/d$ dependence on the diameter. The absolute values, however, are about 10cm^{-1} larger than those predicted from elasticity theory,

and constitute a more precise estimate of the frequencies from the microscopic calculation.

For the Raman measurements the samples [§] were placed on Si-wafers and held in a commercial Oxford cryostat, which was evacuated to $2 \cdot 10^{-6}$ mbar. The samples were cooled to liquid helium temperature. The 514 nm line of an Ar^+-laser was used as excitation source, the laser power was kept below 20 mW to avoid laser heating. The combination of a bandpass filter and a monochromator suppressed possible plasma lines. A Dilor-XY triple monochromator system in backscattering geometry was used with a nitrogen-cooled CCD to acquire the Raman spectra. All samples were measured in two configurations, in focus and out of focus, to exclude possible artifacts. Fig. 5.16 displays a Raman spectrum from CdSe nanorods of 4 nm diameter and 25 nm length in the low-frequency regime. The background present between 20 cm^{-1} and 100 cm^{-1} is attributed to elastically scattered laser light and fitted with a cubic polynomial. Two Raman bands can be identified in the observed frequency range. The prominent asymmetric line around 200 cm^{-1} is attributed to the CdSe longitudinal optical phonon (A_1). The asymmetric shoulder on its low energy side stems from surface optical phonons [165]. The second observed band is located at lower frequencies and can be fitted with a Lorentzian function centered at 21.9 cm^{-1}. To investigate the diameter dependence of the observed Raman band at low frequencies, Raman spectra of samples of various sizes were recorded. Exemplary spectra are displayed in the inset of Fig. 5.16. No significant deviations of the modes frequency from nanorods 4 nm diameter and 30 nm length, compared to the frequency from the 4×25 nm^2 nanorods were found. The observed Raman band at low frequencies does only depend on the nanorod diameter, and follows the diameter-dependent behavior predicted for the RBM, and is thus assigned to the RBM. For nanorods with a diameter around 6 nm and above, the RBM is at quite low frequencies, which makes it harder to detect. We were not able to determine the position of the RBM from nanorods with diameters above 6 nm.

In order to obtain a value for the proportionality constant in $\omega_{\mathrm{RBM}} \propto 1/d$ we fitted the calculated RBM frequencies and our experimentally obtained values. We fitted $\omega_{\mathrm{RBM}} = C/d$ to the RBM frequency versus diameter data. The fit to the complete set of frequencies resulted in $\omega_{\mathrm{RBM}} = 91.0$ $cm^{-1}nm/d$. Fig. 5.17 displays the measured and calculated RBM frequencies along with the C/d-dependence. The determination of the RBM frequency allows a good approximation of the nanorod diameter with a macroscopic technique.

The measurement of the RBM is especially useful to determine the diameter of very thin nanorods where transmission electron microscopy is close to the resolution limit. The RBM frequency is very sensitive to diameter fluctuations below 4 nm, while the frequency of the RBM is less sensitive for diameter changes of thicker nanorods and vanishes for larger structures. These results can be used to characterize thin nanorods *via* Raman spectroscopy. For related

[§] The CdSe nanorods used in the Raman experiment were grown by a standard technique based on the high temperature (300 °C) reaction between organometallic precursors of Cd (dimethylcadmium) and Se (trioctylphosphine selenide) in trioctylphosphine oxide in the presence of hexadecylphosphonic acid as a surface growth modifier [132]. The Raman measurements were performed by Holger Lange, present affiliation TU Berlin.

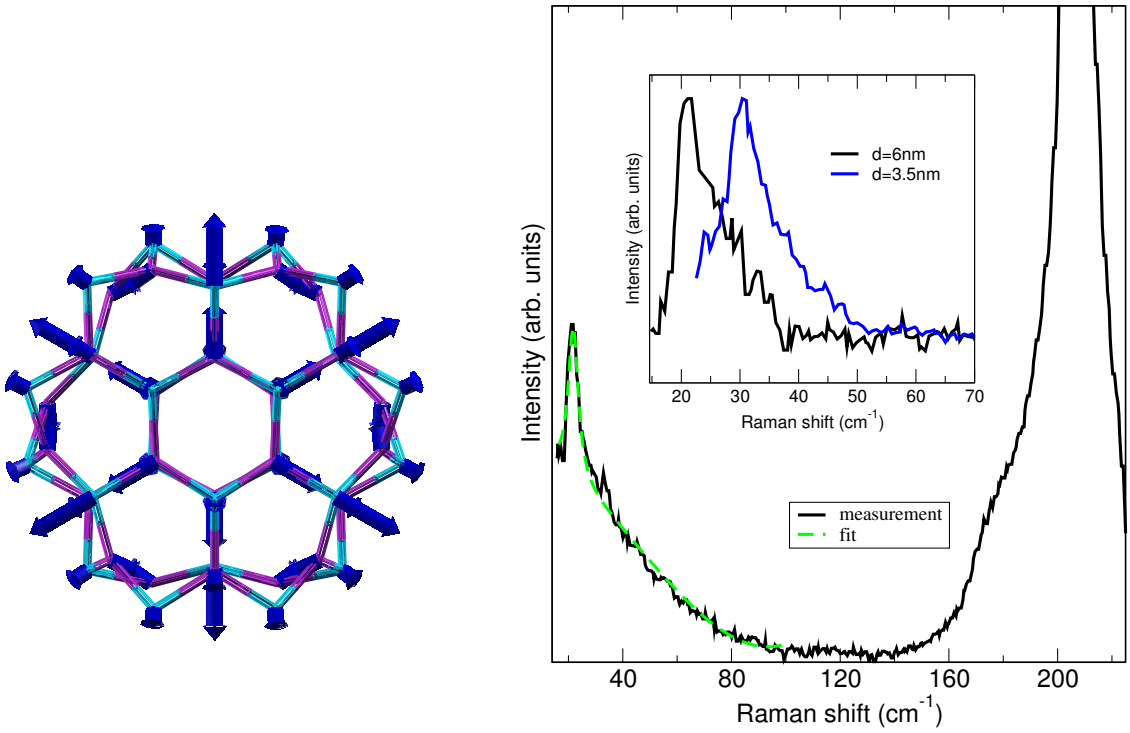

Figure 5.16.: (left) Calculated displacement pattern of the radial breathing mode (RBM) of a 1.4 nm diameter CdSe nanowire. (right) Raman spectrum from CdSe nanorods of 4 nm diameter and 25 nm length. Inset: low-frequency Raman spectra from nanorods of 3.5 nm diameter and 20 nm length, and 6 nm diameter and 35 nm length. The laser-related background was subtracted.

material systems like ZnO, ZnS, ZnSe, where even smaller structures with diameters down to 1 nm exist [171, 172], we predict the existence of the RBM with a similar diameter dependence, but a different material-specific parameter C.

5.4. CdSe/ZnS core/shell nanowires

The possibility to coat the CdSe nanorods with an epitaxial shell of a larger band gap material, like ZnS, is an important enhancement for applications. The ZnS shell increases the luminescence efficiency, decreases the laser threshold and gives rise to further surface modifications that allow *e.g.* biocompatibility [134, 173]. Thus, they are interesting for both, fundamental research [174–176] and technological applications [177, 178]. However, details about the shell and its influence on the CdSe core are difficult to obtain due to the lack of sufficient TEM resolution and the small X-ray structure factor of ZnS compared to CdSe. While there has been considerable effort in understanding the structural and electronic properties of CdSe nanowires from theory [135, 137] there have been little efforts to understand the effects of a surrounding ZnS shell.

In this section the influence of a ZnS shell on the structural and electronic properties is

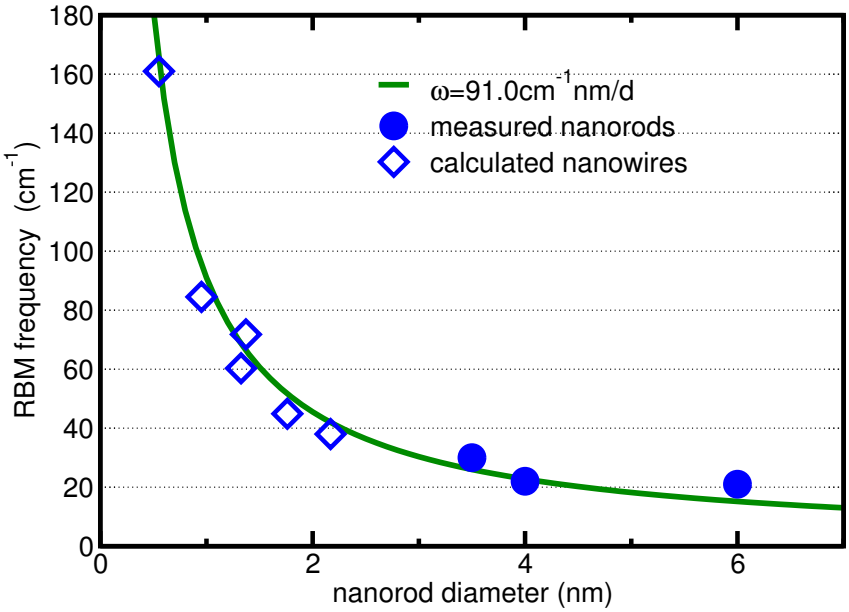

Figure 5.17.: RBM frequency versus nanowire diameter. The curve results from a fit to the experimental and theoretical values.

investigated. The ZnS shell leads to a shortening of the CdSe bond length, the magnitude depending on the bond length orientation with respect to the axis. The electronic band gap is reduced by the presence of the ZnS shell. The CdSe/ZnS multistructure forms a type II heterojunction, in contrast to plane CdSe/ZnS superlattices.

Calculational details To investigate the influence of a ZnS shell, calculations are performed on a nanowire with one and two layers of ZnS shell. To exclude shell effects from size effects, we compare our results also with a thicker nanowire (II) [These two were discussed in Sec. 5.3.2]. The cross section of the relaxed nanowires is shown in Fig. 5.18a). The largest nanowire (IV) consists of a total number of 192 atoms.

For zinc and sulfur norm-conserving pseudopotentials were generated with the Troullier Martins scheme [101] for the following valence-state configurations: Zn $4s^2$ (2.43) $3d^{10}$ (2.09), S $3s^2$ (1.63) $3p^4$ (1.76), where the value in parenthesis indicates the pseudopotential core radii in Bohr. All calculational parameters did not vary except the mesh cutoff compared to those in the CdSe nanowire section 5.2. Because of the smaller core radius of Sulfur compared with Se one has to use a finer calculation grid to obtain equally converged results. Therefore the real space integrations were performed on a grid with a fineness of 0.16 Å, which can represent plane waves up to an energy of 120 Ry in contrast to 80 Ry in section 5.2.

To verify the quality of our Zn and S pseudopotentials bulk ZnS was modeled. A $(6 \times 6 \times 4)$ Monkhorst-Pack [121] mesh in reciprocal space was used. The deviations from the bulk lattice constants were found to be small (<1 %) for wurtzite ZnS, *i.e.*, values of a=3.81 Å and c=6.25 Å,

were found for ZnS. [143] Another test for the validity of our calculations is the bulk modulus and a value of 80.2 GPa was obtained for ZnS, in good agreement with the experimental value of 76.0 GPa [145, 179]. The used formula and its derivation can be found in Appendix B.

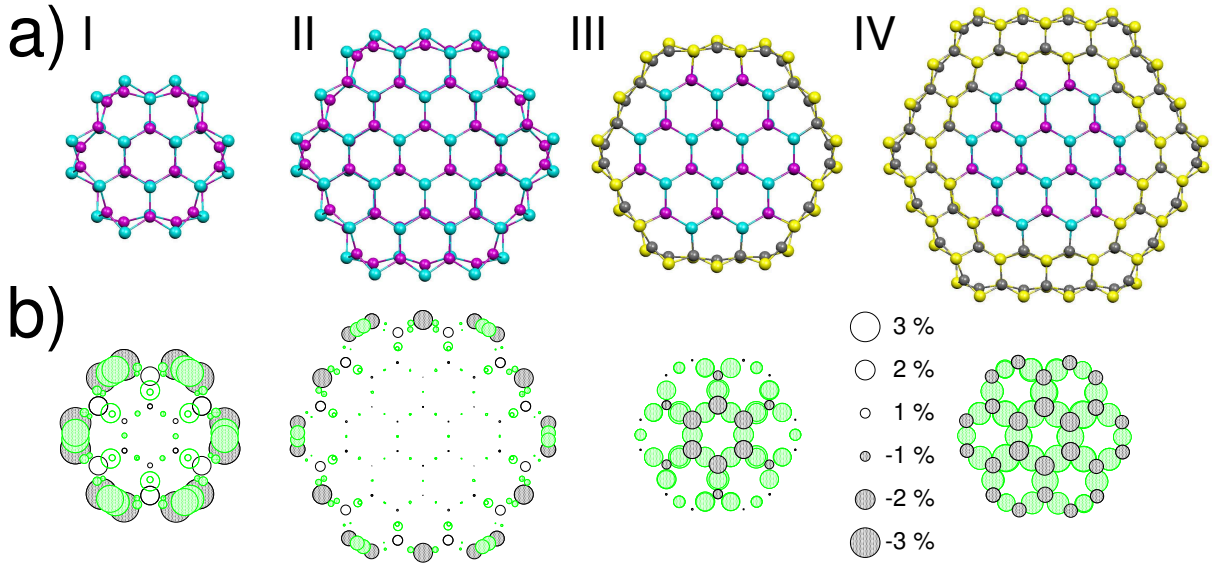

Figure 5.18.: Cross sections of the CdSe nanowires and core/shell CdSe/ZnS nanowires (upper row) and bond length deviations compared to bulk CdSe (lower row). The following color code is used: Cd (magenta), Se (cyan), Zn (black), S (yellow)

5.4.1. Structural details

From the relaxed cross sections in Fig. 5.18(a) it can be seen that the most dramatic changes in the atomic structure happen in the outermost monolayer: the Cd or Zn-atoms rotate into the surface to lower the energy. A hydrogen shell does not qualitatively changes this reconstruction. The effect of the surface reconstruction becomes smaller after the first monolayer. The crystal structure of bulk CdSe is resembled with small deviations, as can be seen in wires I and II.

Figure 5.18 b) shows the bond lengths of the relaxed CdSe nanowires projected on the plane perpendicular to the c-axis. The bonds are centered in the middle of the atoms they connect. The radius of the circles is proportional to the deviation from the bulk CdSe bond length. Black circles correspond to bonds parallel to the nanowire axis, green circles correspond to bonds not parallel to the c-axis (lateral bonds form a ≈120°angle with the nanowire axis).

The coverage of a CdSe NR with a ZnS shell leads to a compressive strain of the CdSe core due to the smaller lattice parameter of ZnS compared to CdSe. The diameter d of wire III is ≈ 5 % smaller than that of wire II. All bonds of the CdSe core are shortened. The bonds in the lateral direction are more strongly compressed than the bonds parallel to the c-axis. The average decrease is 1.75 %, while it is 0.76 % for the bonds parallel to c. The maximal decrease

is 2.3 % and 1.8 % for lateral and parallel bonds, respectively. The bonds parallel to the c-axis show the trend of being less compressed when lying closer to the surface. In contrast, the lateral bonds are homogeneously compressed throughout the CdSe core. A second ZnS layer increases the compression on the CdSe core. The average decrease is 2.3 %, while it is 1.5 % for the bonds parallel to c. The maximal decrease is 2.8 % and 1.9 % for lateral and parallel bonds, respectively. Now the bonds are homogeneously compressed throughout the core [see Fig. 5.18(b)].

Our results show a good agreement with experiments on CdSe/ZnSe nanocrystals. ZnSe has nearly half the lattice mismatch than ZnS, therefore the observed decrease in the experiment is expected to be smaller than in our calculations. The authors of Ref. 180 find a decrease of 1.234 % and 1.511 % for the parameters a and c. The nanocrystals they investigate are spherical, which may explain the similar decrease for a and c, in contrast to our cylindrically shaped wires.

5.4.2. Radial breathing mode in core/shell nanowires

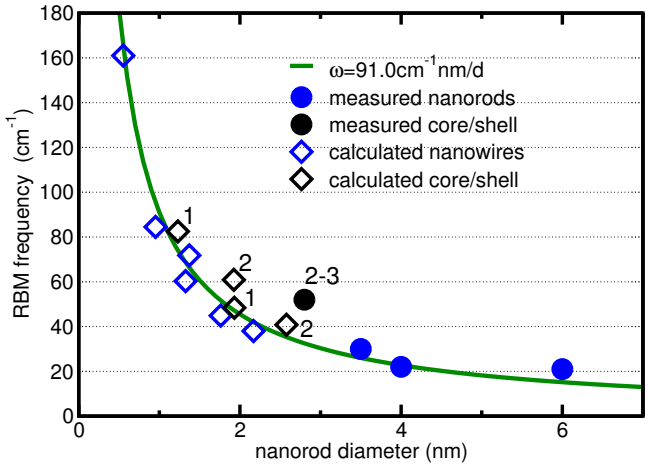

Figure 5.19.: RBM frequency versus nanowire diameter. The curve results from a fit to the core structures only. The core-shell structures are labeled by the number of monolayers.

The radial breathing mode is present in CdSe/ZnS core/shell nanowires as well. In Fig. 5.19 we show the calculated/measured RBM frequencies of bare nanowires and core/shell nanowires. The RBM frequencies of the core-shell structures are higher by $7 - 15$ cm^{-1} than their counterparts of bare CdSe. This is due to compressive strain and the shortened bond lengths in the CdSe core with the addition of a shell (see Fig. 5.18(b)). The effect increases with a thicker shell and thin NWs are influenced more. This is supported by Raman experiments: The RBM of a CdSe nanorod with a diameter of 2.8 nm and a length of 22 nm, covered with a 2-3 monolayer ZnS shell has an energy of 52 cm^{-1}. This is 20 cm^{-1} higher than expected for a bare nanorod of this diameter. The increase of the RBM frequency is somewhat larger, but of the same magnitude as for the calculated NWs. This is due to the thicker shell of the measured nanorods compared

to the shells of the calculated NWs, for which the calculational capacities were limited.

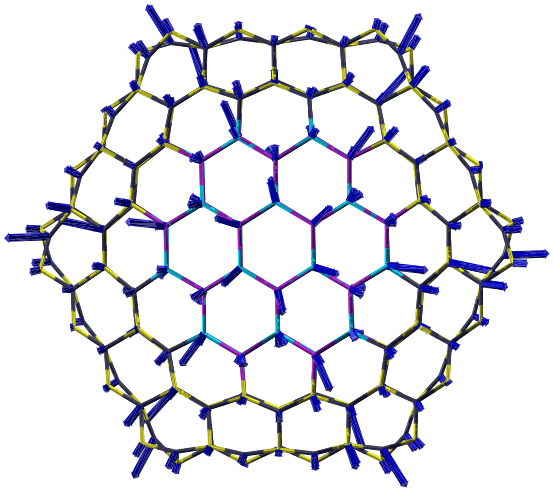

Figure 5.20.: Calculated displacement pattern of the breathing mode of a 2.6 nm diameter CdSe nanowire.

5.4.3. Electronic properties

Additionally to the changes in bond length and RBM frequency, we investigated the changes in the electronic band structure. The inability of the LDA to precisely predict excited energies leads to an underestimation of the band gaps. This is usually corrected using the scissors operator. We have refrained from using it here, as we use two different material systems, which makes it hard to decide a single value for both materials. The generalized gradient approximation (GGA) usually gives a better agreement with experimental band gaps. For wire I the authors of Ref. [181] find a band gap 2.1 eV using GGA. This is close to our LDA value of 1.97 eV.

Table 5.1.

	Wire I	Wire II	Wire III	Wire IV	Wire I (GGA)*
# of atoms	48	108	108	192	48
diameter d (Å)	14	22	21	26	14
calc. band gap (eV)	1.97	1.67	1.74	1.67	2.1

[1] Ref. 181

Figure 5.21 shows the calculated band structure and the electronic density of states of the wires I-III from Figure 5.18. The calculated values are summarized in Table 5.1. The band gap of the nanowire becomes smaller with the addition of a ZnS shell. Confinement effects alone should lead to a large band gap. This indicates that the electronic systems of the core and the shell interact. For the wire III we plot the DOS projected on the CdSe atoms, to better

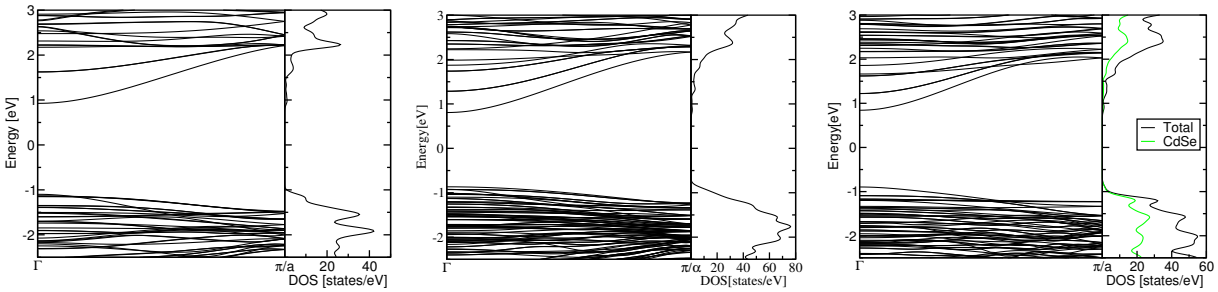

(a) Wire I **(b)** Wire II **(c)** Wire III

Figure 5.21.: Band structure and DOS (Gaussian broadening of 0.1 eV). In the DOS of wire III the projected DOS of the CdSe atoms is plotted.

visualize the effect of the ZnS-shell. This PDOS suggest that the lowest band stems from the ZnS shell. This, however, influences the type of junction that is formed by the multistructure. If the band-gap of the core is enclosed by that of the shell material, this configuration is known as type I, and the electron and hole wave functions may be confined in the core region. The classification is done *via* an analysis of the bulk band structure and the bulk work function of the corresponding materials. The band diagram we obtain within our calculations of bulk material is shown in Figure 5.22a). This is in agreement with other work that classify CdSe/ZnS heterojunction as type I [182].

A detailed analysis of the valence band maximum (VBM) and the conduction band minimum (CBM) shows that for small systems like here, the CdSe/ZnS junction turns into a type II system, where the band gaps are staggered. The squares of the wave function of the CBM and the VBM were added for 8 equidistant planes within the unit cell and plotted in Figure 5.22 b) and c). The valence band maximum is strictly confined to the core region. The conduction band minimum is strongly located on the ZnS shell. Wire IV shows the same feature. This has important consequences for applications. Core shell nanowires have been recently discovered to serve as solar cells [183]. An advantage of this core/shell architecture is that carrier separation takes place in the radial direction whereas carrier transport is done along the axial direction. And as electrons are confined in the core and the holes are confined in the shell recombination is minimized. This can explain the quantum yield increase observed when growing a ZnS shell around CdSe nanorods. [1]

During the creation of this thesis, Smith *et al.* have shown experimental evidence of this phenomenon for core/shell quantum dots of different II/VI compounds including CdSe/ZnS core-shell quantum dots [2]. They find a fluorescence quantum yield increase of 600% for 2 monolayers of ZnS see Fig. 5.23, which can be easily explained by the spatial separation of the excited charge carriers, which we suggest from our calculations.

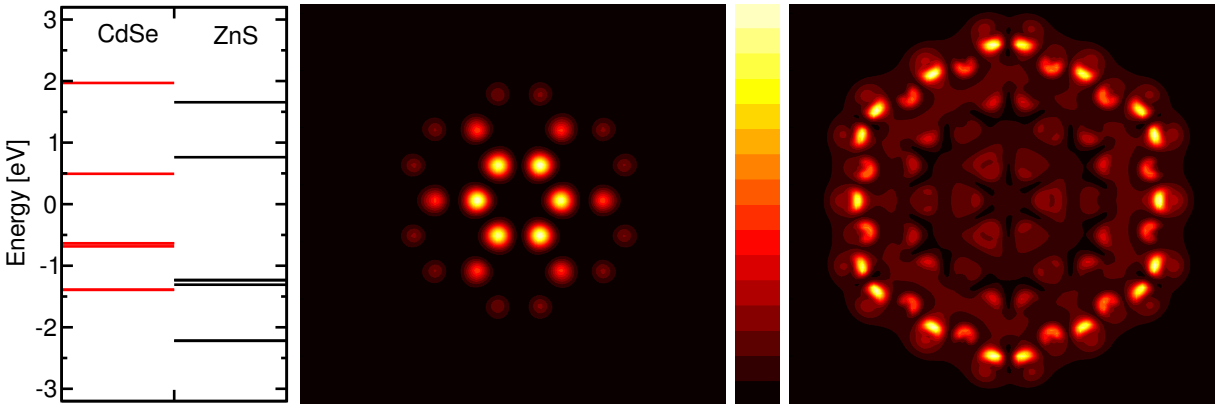

(a) Energy diagrams of bulk CdSe and ZnS from calculations

(b) Valence band maximum of wire III

(c) Conduction band minimum of wire III

Figure 5.22.: Cross-section views of the squared wave function of the CBM electron state and VBM hole state in core-shell nanowires. The atomic structure is that of wire III in Figure 5.18.

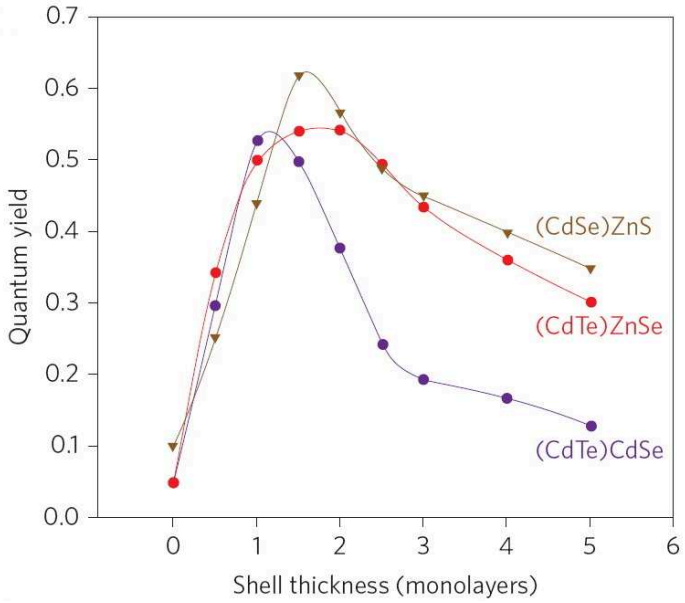

Figure 5.23.: Quantum yield over number of monolayers for different core/shell quantum dots. Taken from Ref. 2

6. Summary and outlook

In this work the electronic and vibrational properties of nanostructures made of elemental carbon and the binary compound CdSe were investigated. The investigations were performed on different geometric forms, flat layers, small stripes of layers, hollow tubes or crystalline wires. A direct observation of these structures is very difficult and requires expensive and highly sophisticated methods. Here a combination of *ab-initio* calculations and inelastic light scattering experiments was applied. Density-functional theory has several advantages. It is completely independent from experiments, and allows full quantum-mechanical studies. Every step of the calculation is performed self-consistently without further assumptions. This allows for obtaining the full phonon spectrum with little errors of only up to a few percent.

The symbiosis of theory and experiment resulted in predictions that were verified experimentally, and experimental results that required new theoretical models for being fully explained.

Using the relatively young experimental technique of inelastic X-ray, the full in-plane phonon dispersion of graphite could be determined. The overall shape of the phonon bands confirms the quality of *ab-initio* DFT calculations. By including fifth-nearest neighbor interaction, the phonon bands can be well described within a force-constants model. Previous empirical models predicted only parts of the phonon dispersion correctly, since experimental data in the $K - M$ region had been missing. The force constants can be used to calculate the phonon dispersion for any point in the Brillouin zone of graphene.

Considering the dynamical representation of distinct phonon modes at the high-symmetry points in graphene Γ, K, and M, we identified the phonon modes that can couple to the electronic systems. After calculating the electron-phonon interaction it was found that those modes related to a Kohn anomaly show a distinct behaviour that can be seen in the fermi energy shift and in the change of electronic energy.

Recently performed experiments on uniaxially strained graphene motivated the calculations of strain in graphene. The uniaxial strain lowers the hexagonal symmetry and lifts degeneracies. It was shown that graphene remains semimetallic under small strain and that the position of the Dirac cones is altered. The anisotropic compression of the Dirac cone and with that the anisotropic Fermi velocities suggest favored directions for the electronic transport, which may explain the anisotropic resistance found recently in experiments [75]. The obtained shift rates of the Raman-active G and $2D$-band strongly support certain experiments [77, 79] and indicate slipping effects in others [76].

The shift of the $2D$-band in uniaxially strained graphene led to unforeseen results. The result needed a modifcation of the established double-resonance model and shed light on the origin of the $2D$-mode. This mode is present in all sp^2 carbon structures. Depending on polarization and strain direction, different shifts of the Raman-active $2D$-band are predicted. Strain in zigzag directions leads to a larger splitting than strain in armchair directions. Our predictions are in excellent agreement with experiments on strained graphene samples. As the strain-induced shift is used to determine strain in graphene our results are relevant for the interpretation of experimental data.

The vibrational properties of graphene nanoribbons were investigated. The Γ-point phonons of graphene nanoribbons with armchair and zigzag type edges can be interpreted as six fundamental oscillations and their overtones that show a characteristic nanoribbon width dependence. We further found a family dependence for the fundamental modes of armchair nanoribbons, which is in correspondence to the known family behaviour of their band gaps [99]. The longitudinal-optical and transverse-optical modes in our calculations feature a noticeable splitting and should be experimentally measureable. The Γ-point phonon frequencies of nanoribbons can be mapped onto the phonon dispersion of graphene which corresponds to an "unfolding" of the nanoribbons' Brillouin zone onto that of graphene (in contrast to the widely used zone-folding approach).

For carbon nanotubes a detailed study of the mixing of the fully-symmetric Raman-active modes in carbon nanotubes was performed. It could be confirmed *via* an independent variational approach that the RBM has small non-radial components. They have only little influence on phonon frequency calculations but a big quantitative effect on electron-phonon coupling matrix element $\mathcal{M}_{e-ph}$. Neglecting them results in errors of up to 60 %. In the same way, the HEM is not purely axial or circumferential. Here a big influence of the mixing is found on the phonon frequency calculation but a rather small effect on the magnitude of $\mathcal{M}_{e-ph}$. These results have important implications for the determination of chiral abundances in ensembles of nanotubes, when obtained *via* Raman scattering strength of nanotubes of different chirality.

The existence of an anharmonicity of the high-energy mode in carbon nanotubes and the E_{2g}-mode in graphene was demonstrated. Its origin lies in the hexagonal geometry, and is inherent in other hexagonal systems as well.

We used an iterative relaxation process for the calculation of phonons in CdSe nanowires that reproduces the frequencies of degenerate phonon modes. The size dependence of phonon frequency compared to bulk modes was analyzed. It was found that modes that mainly vibrate along the wire axis showed a stronger size-dependence than modes with eigenvectors perpendicular to the axis.

The calculation predicted a radial breathing mode in CdSe nanowires which was confirmed by Raman spectroscopy. This was the first direct proof of the existence of such a breathing mode in nanorods. The diameter dependence of the mode can be exploited to estimate the nanowire diameter. This result can be used to characterize thin nanorods *via* Raman spectroscopy. For

related material systems like ZnO, ZnS, ZnSe, where even smaller structures exist, the existence of a RBM with similar dependencies is likely.

The shift of this mode, when the nanowire is covered with an additional shell of another material gives information on the thickness of the shell. By comparing the results of calculations with and without a shell, we analyze the effect of the shell on the structural and electronic properties. The bond lengths of the CdSe core are reduced differently depending on the orientation of the bond to the axis. Growing a wide bandgap shell around a narrow bandgap core should result in a type-I heterejunction, but if core and shell are small enough, the system can turn into a type-II heterojunction. This was a result from our calculations of the CdSe/ZnS core/shell nanowire. This naturally explains the observed higher quantum-yield in photoluminscence experiments. This opens possibilies for new applications of CdSe/ZnS core/shell nanorods.

Although some achievements could be made, there is still room for more. The use of symmetries was succesfully applied throughout the thesis. A promising improvement would be the implementation of line group symmetries into the heart of the DFT-codes. Currently only space groups are used in these methods. They do only govern the symmetry of the unit cell, which is often cubic or hexagonal for onedimensional structures. Line groups would allow a systematic study of all chiralities of nanotubes, or of nanowires with a much larger sizes.

Throughout the thesis we have used DFT calculations on the level of local, single-particle approximations. By definition, these are not able to predict excited energies correctly. This implies the failure to predict correct conduction band energies, although, in general, the trends and effective masses are in agreement with improved calculations or experiments. There exist better approximations, but require much higher computational effort. Among them are the time-dependent DFT (TDDFT) approach to calculate excited electronic states, and the use of the GW-approximation that describes self energies correctly.

A few predictions in this thesis were made that lack an experimental verification. Anharmonic modes should have different time constants, measuring the time dependent Raman spectrum of the E_{2g}-mode in graphene, for which an anharmonicity was found, could be interesting.

A lot of width-dependent properties of nanoribbons have been predicted. In addition, a similar mode to the RBM, the breathing-like-mode (BLM) is also predicted to be strongly size dependent [184]. These features could be measured by means of Raman spectroscopy, which would be an interesting task for future works. The nanoribbons are confined in space, polarized measurement of the $2D$-mode should give additional insight.

The calculations of the nanoribbons have, due to computational reasons, only been performed for zigzag or armchair edges. The extension of nanoribbons with arbitrary edges is a task for the future. Also, a complete zone-folding model that is available for carbon nanotubes and of great help in understanding CNT properties, is missing for graphene nanoribbons of arbitrary shape.

Appendix A.

Koster notation

Every group element of the space group can be represented as a 4x4 matrix

$$(R|t) = \left(\begin{array}{c|c} R & t \\ \hline 0 & 1 \end{array}\right). \tag{A.1}$$

R is a 3x3 matrix, representing symmetry operations except pure translations; t is a vector of dimension 3 and corresponds to pure translations. The fourth row is mandatory and due to multiplication reasons.

As an example a pure rotation of 180 degrees around the x-axis is considered:

$$\delta_{2x} = (\delta_{2x}|0) \left(\begin{array}{ccc|c} 1 & 0 & 0 & 0 \\ 0 & -1 & 0 & 0 \\ 0 & 0 & -1 & 0 \\ \hline 0 & 0 & 0 & 1 \end{array}\right). \tag{A.2}$$

As an example of a pure translation we consider the translation t_d along the body diagonal. Here R is the identity-matrix ϵ and the translation is taken into account in the last column:

$$T_d = (\epsilon|t_d) \left(\begin{array}{ccc|c} 1 & 0 & 0 & a/2 \\ 0 & 1 & 0 & a/2 \\ 0 & 0 & 1 & a/2 \\ \hline 0 & 0 & 0 & 1 \end{array}\right) \tag{A.3}$$

Vectors in this notation have 4 rows and in the last one there is a 1.

$$\vec{r} = (x, y, z, 1)^T \tag{A.4}$$

For combining rotations with translations simple matrix multiplication is taken:

$$(\delta_{2x}|t_d) = \delta_{2x} \cdot t_d = \left(\begin{array}{ccc|c} 1 & 0 & 0 & a/2 \\ 0 & -1 & 0 & a/2 \\ 0 & 0 & -1 & a/2 \\ \hline 0 & 0 & 0 & 1 \end{array}\right) \tag{A.5}$$

Operating a symmetry operation on an arbitrary vector $\vec{r}$ is also performed with :

$$(R|t)\vec{r} = \left(\begin{array}{c|c} R & t \\ \hline 0 & 1 \end{array}\right)\left(\begin{array}{c} \vec{r} \\ 1 \end{array}\right) = \left(\begin{array}{c} R\vec{r}+t \\ 1 \end{array}\right) \tag{A.6}$$

This notation naturally satisfies the usual multiplication rules for space groups

$$(R_2|\vec{t_2})(R_1|\vec{t_1}) = (R_2R_1|R_2\vec{t_1}+\vec{t_2}) \tag{A.7}$$

$$(R|\vec{t})^{-1} = (R^{-1}|-R^{-1}\vec{t}) \tag{A.8}$$

Operating a symmetry operation $(R|t)$ on a function $\Psi(\vec{r})$ is done by applying the inverse element $(R|\vec{t})^{-1}$ to the argument

$$\Psi' = (R|t)\Psi(\vec{r}) = \Psi((R|t)^{-1}\vec{r}) = \Psi(R^{-1}\vec{r}-R^{-1}\vec{t}). \tag{A.9}$$

Appendix B.

Derivation of Murnaghan's equation of state

The response of the system to an external hydrostatic pressure is described by the bulk modulus defined as

$$B_0 = -V_0 \left(\frac{\partial P}{\partial V}\right)_{V_0} \tag{B.1}$$

which expresses the relation between the applied pressure P and the change in volume V of the solid.

The assumption underlying Murnaghan's equation of state [185] is that the bulk modulus B of a medium under uniform pressure is linear in P:

$$B = c(1 + kP) \tag{B.2}$$

where c and k are coefficients. This definition implies

$$c = -V \left(\frac{\partial P}{\partial V}\right)_0 \equiv B_0 \tag{B.3}$$

and

$$ck = -\frac{\partial}{\partial P}\left(V\frac{\partial P}{\partial V}\right)_0 \equiv B_0' \tag{B.4}$$

By integrating Eq. B.1 we obtain Murnaghan's equation of state

$$\frac{V_0}{V} = (1 + kP)^{\frac{1}{ck}} \rightarrow \frac{\Delta V}{V_0} = 1 - (1 + kP)^{-\frac{1}{ck}} \tag{B.5}$$

where $V_0 = V(P = 0)$ and $\Delta V = V_0 - V$. The energy change induced by the application of pressure is

$$dE = -PdV \tag{B.6}$$

Now we can invert Eq. B.5 to obtain $P = P(V)$, substitute in Eq. B.6 and integrate, obtaining:

$$E - E_0 = \frac{1}{k}\int_{V_0}^{V}\left(\frac{V_0}{v}\right)^{ck} dv + \frac{1}{k}\int_{V_0}^{V} dv = \frac{V}{k(ck-1)}\left[\left(\frac{V_0}{V}\right)^{ck} + ck - 1\right] - \frac{cV_0}{ck-1}. \quad \text{(B.7)}$$

Using definitions B.3 and B.4 we obtain the expression for the energy we will use to fit the calculated data in Secs. 5.2 and 5.4.

$$E(V) = \frac{B_0 V}{B_0'}\left[\frac{(V_0/V)^{B_0'}}{B_0' - 1} + 1\right] - \frac{B_0 V_0}{B_0' - 1} + E(V_0). \quad \text{(B.8)}$$

Bibliography

[1] L. Manna, E. C. Scher, L.-S. Li, and A. P. Alivisatos, "Epitaxial growth and photochemical annealing of graded CdS/ZnS shells on colloidal CdSe nanorods", J. Am. Chem. Soc. **124**(24), 7136 – 7145 (2002).

[2] A. M. Smith, A. M. Mohs, and S. Nie, "Tuning the optical and electronic properties of colloidal nanocrystals by lattice strain", Nature nanotechnology **4**(2008), 56 (2008).

[3] P. Hohenberg and W. Kohn, "Inhomogeneous electron gas", Phys. Rev. **136**, B864 (1964).

[4] W. Kohn and L. J. Sham, "Self-consistent equations including exchange and correlation effects", Phys. Rev. **140**, A1133 (1965).

[5] M. C. Payne, M. P. Teter, D. C. Allan, T. A. Arias, and J. D. Joannopoulos, "Iterative minimization techniques for ab initio total-energy calculations: molecular dynamics and conjugate gradients", Rev. Mod. Phys. **64**, 1045 (1992).

[6] J. P. Perdew and A. Zunger, "Self-interaction correction to density-functional approximations for many-electron systems", Phys. Rev. B **23**, 5048 (1981).

[7] J. P. Perdew and Y. Wang, "Accurate and simple analytic representation of the electron-gas correlation energy", Phys. Rev. B **45**, 13 244 (1992).

[8] J. P. Perdew, K. Burke, and M. Ernzerhof, "Generalized Gradient Approximation Made Simple", Phys. Rev. Lett. **77**, 3865 – 3868 (1996).

[9] J. M. Soler, E. Artacho, J. D. Gale, A. García, J. Junquera, P. Ordejón, and D. Sánchez-Portal, "The SIESTA method for ab initio order-N materials simulation", J. Phys. Condens. Mat. **14**, 2745 (2002).

[10] G. P. Srivastava, *The physics of phonons* (Adam Hilger, Bristol, 1990).

[11] K. Kunc, I. Loa, K. Syassen, R. K. Kremer, and K. Ahn, "MgB_2 under pressure: phonon calculations, Raman spectroscopy, and optical reflectance", J. Phys.: Condens. Matter **13**(44), 9945 (2001).

[12] P. Y. Yu and M. Cardona, *Fundamentals of Semiconductors* (Springer-Verlag, Berlin and Heidelberg and New York, 1996).

[13] M. T. Yin and M. L. Cohen, "Theory of lattice-dynamical properties of solids: Application to Si and Ge", Phys. Rev. B **26**(6), 3259 (1982).

[14] M. Mohr, M. Machón, J. Maultzsch, and C. Thomsen, "Double-resonant Raman processes in germanium : Group theory and *ab initio* calculations", Phys. Rev. B **73**, 035 217 (2006).

[15] S. Baroni, S. de Gironcoli, A. D. Corso, and P. Giannozzi, "Phonons and related crystal properties from density-functional perturbation theory", Rev. Mod. Phys. **73**(2), 516 (2001).

[16] C. V. Raman, "A new radiation", Indian J. Phys. **2**, 387 (1928).

[17] C. V. Raman and K. S. Krishnan, "A new type of secondary radiation", Nature **121**, 501 (1928).

[18] F. Cerdeira, E. Anastassakis, W. Kauschke, and M. Cardona, "Stress-induced doubly resonant Raman scattering in GaAs", Phys. Rev. Lett. **57**, 3209 (1986).

[19] S. I. Gubarev, T. Ruf, and M. Cardona, "Doubly resonant Raman scattering in the semimagnetic semiconductor $Cd_{0.95}Mn_{0.05}Te$", Phys. Rev. B **43**, 1551 (1991).

[20] F. Agulló-Rueda, E. E. Mendez, and J. M. Hong, "Double resonant Raman scattering induced by an electric field", Phys. Rev. B **38**, 12 720 (1988).

[21] M. Cardona, "Resonance phenomena", in *Light Scattering in Solids II*, edited by M. Cardona and G. Güntherodt (Springer, Berlin, 1982), vol. 50 of *Topics in Applied Physics*, p. 19.

[22] R. M. Martin and L. M. Falicov, "Resonant Raman scattering", in *Light Scattering in Solids I: Introductory Concepts*, edited by M. Cardona (Springer-Verlag, Berlin, Heidelberg, New York, 1983), vol. 8 of *Topics of Applied Physics*, p. 79.

[23] S. Reich, C. Thomsen, and J. Maultzsch, *Carbon Nanotubes: Basic Concepts and Physical Properties* (Wiley-VCH, Berlin, 2004).

[24] S. Iijima, "Helical microtubules of graphitic carbon", Nature **354**, 56 – 58 (1991).

[25] C. Thomsen and S. Reich, "Raman scattering in carbon nanotubes", in *Light Scattering in Solids IX*, edited by M. Cardona and R. Merlin (Springer, Heidelberg, 2007), vol. 108 of *Topics in Applied Physics*, chap. 3.

[26] K. S. Novoselov, A. K. Geim, S. V. Morozov, D. Jiang, Y. Zhang, *et al.*, "Electric Field Effect in Atomically Thin Carbon Films", Science **306**(5696), 666 (2004).

[27] Y. Zhang, Y.-W. Tan, H. L. Stormer, and P. Kim, "Experimental observation of the quantum Hall effect and Berry's phase in graphene", Nature **438**, 201 (2005).

[28] K. S. Novoselov, A. K. Geim, S. V. Morozov, D. Jiang, M. I. Katsnelson, *et al.*, "Two-dimensional gas of massless Dirac fermions in graphene", Nature **438**(2), 197 (2005).

[29] K. S. Novoselov, Z. Jiang, Y. Zhang, S. V. Morozov, H. L. Stormer, *et al.*, "Room-Temperature Quantum Hall Effect in Graphene", Science **315**(5817), 1379 (2007).

[30] A. K. Geim and K. S. Novoselov, "The rise of graphene", Nature Materials **6**, 183 (2007).

[31] E. W. Hill, A. K. Geim, K. Novoselov, F. Schedin, and P. Blake, "Graphene spin valve devices", IEEE Trans. Magn. **42**, 2694 – 2696 (2006).

[32] L. Börnstein, *Group III Condensed Matter, Volume 41 Semiconductors, II-VI and I-VII Compounds; Semimagnetic Compounds* (Springer, 2002).

[33] A. C. Ferrari, J. C. Meyer, V. Scardaci, C. Casiraghi, M. Lazzeri, *et al.*, "Raman Spectrum of Graphene and Graphene Layers", Phys. Rev. Lett. **97**, 187 401 (2006).

[34] J.-Y. Park, S. Rosenblatt, Y. Yaish, V. Sazanova, H. Üstünel, *et al.*, "Electron-phonon scattering in metallic single-walled carbon nanotubes", Nano Lett. **4**, 517 (2004).

[35] M. Lazzeri and F. Mauri, "Phonon linewidths and electron phonon coupling in nanotubes", Phys. Rev. B **73**, 165 419 (2006).

[36] R. Nicklow, N. Wakabayashi, and H. G. Smith, "Lattice dynamics of pyrolytic Graphite", Phys. Rev. B **5**(12), 4951 (1972).

[37] C. Oshima, T. Aizawa, R. Souda, Y. Ishizawa, and Y. Sumiyoshi, "Surface phonon dispersion curves of graphite (0001) over the entire energy region", Solid State Commun. **65**(12), 1601 (1988).

[38] S. Siebentritt, R. Pues, K.-H. Rieder, and A. M. Shikin, "Surface phonon dispersion in graphite and in a lanthanum graphite intercalation compound", Phys. Rev. B **55**(12), 7297 (1997).

[39] H. Yanagisawa, T. Tanaka, Y. Ishida, M. Matsue, E. Rokuta, S. Otani, and C. Oshima, "Analysis of phonons in graphene sheets by means of hreels measurement and ab initio calculation", Surf. Interface Anal. **37**(2), 133 (2005).

[40] J. Maultzsch, S. Reich, C. Thomsen, H. Requardt, and P. Ordejón, "Phonon dispersion of graphite", Phys. Rev. Lett. **92**, 075 501 (2004).

[41] S. Piscanec, M. Lazzeri, F. Mauri, A. C. Ferrari, and J. Robertson, "Kohn Anomalies and Eletron-Phonon Iteractions in Graphite", Phys. Rev. Lett. **93**, 185 503 (2004).

[42] R. Al-Jishi and G. Dresselhaus, "Lattice-dynamical model for graphite", Phys. Rev. B **26**, 4514 (1982).

[43] L. Wirtz and A. Rubio, "The phonon dispersion of graphite revisited", Solid State Commun. **131**, 141 (2004).

[44] E. Burkel, "Phonon spectroscopy by inelastic x-ray scattering", Rep. Prog. Phys. **63**, 171 (2000).

[45] M. Krisch and F. Sette, "Inelastic X-ray scattering from phonons", in *Light Scattering in Solids IX*, edited by M. Cardona and R. Merlin (Springer, Berlin, 2007), vol. 108 of *Topics in Applied Physics*.

[46] P. Trucano and R. Chen, "Structure of graphite by neutron-diffraction", Nature **258**(5531), 136 – 137 (1975).

[47] A. K. Kirov, M. I. Aroyo, and J. M. Perez-Mato, "*NEUTRON*: a program for computing phonon extinction rules of inelastic neutron scattering and thermal diffuse scattering experiments", Journal of Applied Crystallography **36**(4), 1085–1089 (2003), see also the Bilbao crystallographic server, http://www.cryst.ehu.es.

[48] R. J. Nemanich and S. A. Solin, "First- and second-order Raman scattering from finite-size crystals of graphite", Phys. Rev. B **20**(2), 392 (1979).

[49] T. Inui, Y. Tanabe, and Y. Onodera, *Group Theory and its Application in Physics* (Springer, Berlin, 1996).

[50] S. Reich and C. Thomsen, "Raman spectroscopy of graphite", Phil. Trans. R. Soc. Lond. A **362**, 2271 (2004).

[51] P. Pavone, R. Bauer, K. Karch, O. Schütt, S. Vent, *et al.*, "Ab initio phonon calculations in solids", Physica B **219**, 439 (1996).

[52] R. J. Nemanich, G. Lucovsky, and S. A. Solin, "Infrared optical vibrations of graphite", Solid State Comm. **23**, 117 (1977).

[53] D. Sánchez-Portal, E. Artacho, J. M. Soler, A. Rubio, and P. Ordejón, "*Ab initio* structural, elastic, and vibrational properties of carbonnanotubes", Phys. Rev. B **59**, 12 678 (1999).

[54] O. Dubay and G. Kresse, "Accurate density functional calculations for the phonon dispersion relations of graphite layer and carbon nanotubes", Phys. Rev. B **67**(3), 035 401 (2003).

[55] A. Grüneis, J. Serrano, A. Bosak, M. Lazzeri, S. L. Molodtsov, *et al.*, "Phonon surface mapping of graphite: Disentangling quasi-degenerate phonon dispersions", Phys. Rev. B **80**(3), 085 423 (2009).

[56] J. Kulda, H. Kainzmaier, D. Strauch, B. Dorner, M. Lorenzen, and M. Krisch, "Overbending of the longitudinal optical phonon branch in diamond as evidenced by inelastic neutron and x-ray scattering", Phys. Rev. B **66**, 241 402(R) (2002).

[57] A. Bosak, J. Serrano, M. Krisch, K. Watanabe, T. Taniguchi, and H. Kanda, "Elasticity of hexagonal boron nitride: Inelastic x-ray scattering measurements", Phys. Rev. B **73**, 041 402 (2006).

[58] R. A. Jishi, L. Venkataraman, M. S. Dresselhaus, and G. Dresselhaus, "Phonon modes in carbon nanotubes", Chem. Phys. Lett. **209**, 77–82 (1993).

[59] M. Dražić, C. Lavor, N. Maculan, and N. Mladenović, "A continuous variable neighborhood search heuristic for finding the three-dimensional structure of a molecule", European Journal of Operational Research **185**(3), 1265 – 1273 (2008).

[60] W. Press, B. P. Flannery, S. A. Teukolsky, and W. T. Vetterling, *Numerical Recipes* (Cambridge University Press, Cambridge, 1986).

[61] E. Dobardžić, I. Milošević, B. Nikolić, T. Vuković, and M. Damnjanović, "Single-wall carbon nanotubes phonon spectra: Symmetry-based calculations", Phys. Rev. B **68**, 045 408 (2003).

[62] C. Mapelli, C. Castiglioni, G. Zerbi, and K. Müllen, "Common force field for graphite and polycyclic aromatic hydrocarbons", Phys. Rev. B **60**, 12 710 (1999).

[63] W. Kohn, "Image of the Fermi Surface in the Vibration Spectrum of a Metal", Phys. Rev. Lett. **2**, 393 – 394 (1959).

[64] I. Milošević, N. Kepčija, E. Dobardžić, M. Mohr, J. Maultzsch, C. Thomsen, and M. Damnjanoviić, "Symmetry-based analysis of the electron-phonon interaction in graphene", phys. stat. sol. (b) **246**, 2606 (2009).

[65] P. Giannozzi *et al.*, http://www.quantum-espresso.org.

[66] A. M. Rappe, K. M. Rabe, E. Kaxiras, and J. D. Joannopoulos, "Optimized pseudopotentials", Phys. Rev. B **41**, 1227 – 1230 (1990).

[67] M. Methfessel and A. T. Paxton, "High-precision sampling for Brillouin-zone integration in metals", Phys. Rev. B **40**, 3616 (1989).

[68] M. Mohr, J. Maultzsch, E. Dobardžić, S. Reich, I. Milošević, *et al.*, "Phonon dispersion of graphite by inelastic x-ray scattering: Determination of the mid-frequency range between K and M", Phys. Rev. B **76**, 035 439 (2007).

[69] O. L. Blakslee, D. G. Proctor, E. J. Seldin, G. B. Spence, and T. Weng, "Elastic Constants of Compression-Annealed Pyrolytic Graphite", J. Appl. Phys. **41**, 3373 (1970).

[70] Z. H. Ni, T. Yu, Y. H. Lu, Y. Y. Wang, Y. P. Feng, and Z. X. Shen, "Uniaxial Strain on Graphene: Raman Spectroscopy Study and Band-Gap Opening", ACS Nano **2**, 2301 – 2305 (2008).

[71] G. Gui, J. Li, and J. Zhong, "Band structure engineering of graphene by strain: First-principles calculations", Phys. Rev. B **78**, 075 435 (2008).

[72] V. M. Pereira, A. H. Castro-Neto, and N. M. R. Peres, "Tight-binding approach to uniaxial strain in graphene", Phys. Rev. B **80**, 045 401 (2009).

[73] Z. H. Ni, T. Yu, Y. H. Lu, Y. Y. Wang, Y. P. Feng, and Z. X. Shen, "Uniaxial Strain on Graphene: Raman Spectroscopy Study and Band-Gap Opening", ACS Nano **22**, 483 (2009).

[74] S.-M. Choi, S.-H. Jhi, and Y.-W. Son, "Effects of strain on electronic properties of graphene", Phys. Rev. B **81**, 081 407 – R (2010).

[75] K. S. Kim, Y. Zhao, H. Jang, S. Y. Lee, J. M. Kim, *et al.*, "Large-scale pattern growth of graphene films for stretchable transparent electrodes", Nature **457**, 706 – 710 (2009).

[76] M. Huang, H. Yan, C. Chen, D. Song, T. F. Heinz, and J. Hone, "Phonon softening and crystallographic orientation of strained graphene studied by Raman spectroscopy", PNAS **106**, 7304 (2009).

[77] T. M. G. Mohiuddin, A. Lombardo, R. R. Nair, A. Bonetti, G. Savini, *et al.*, "Uniaxial strain in graphene by Raman spectroscopy: G peak splitting, Grüneisen parameters, and sample orientation", Phys. Rev. B **79**, 205 433 (2009).

[78] F. Liu, P. Ming, and J. Li, "Ab initio calculation of ideal strength and phonon instability of graphene under tension", Phys. Rev. B **76**, 064 120 (2007).

[79] G. Tsoukleri, J. Parthenios, K. Papagelis, R. Jalil, A. C. Ferrari, *et al.*, "Subjecting a Graphene Monolayer to Tension and Compression", Small **5**(21), 2397 – 2402 (2009).

[80] C. Thomsen and S. Reich, "Double resonant Raman scattering in graphite", Phys. Rev. Lett. **85**, 5214 (2000).

[81] J. Maultzsch, S. Reich, and C. Thomsen, "Double-resonant Raman scattering in graphite: Interference effects, selection rules and phonon dispersion", Phys. Rev. B **70**, 155 403 (2004).

[82] J. Yan, Y. Zhang, P. Kim, and A. Pinczuk, "Electric Field Effect Tuning of Electron-Phonon Coupling in Graphene", Phys. Rev. Lett. **98**, 166 802 (2007).

[83] J. Kürti, V. Zolyomi, A. Grüneis, and H. Kuzmany, "Double resonant Raman phenomena enhanced by van Hove singularities in single-wall carbon nanotubes", Phys. Rev. B **65**, 165 433 (2002).

[84] R. Narula and S. Reich, "Double resonant Raman spectra in graphene and graphite: A two-dimensional explanation of the Raman amplitude", Phys. Rev. B **78**, 165 422 (2008).

[85] P. R. Wallace, "The band theory of graphite", Phys. Rev. **71**, 622 (1947).

[86] A. Grüneis, R. Saito, G. G. Samsonidze, T. Kimura, M. A. Pimenta, *et al.*, "Inhomogeneous optical absorption around the K point in graphite and carbon nanotubes", Phys. Rev. B **67**, 165 402 (2003).

[87] M. Mohr, K. Papagelis, J. Maultzsch, and C. Thomsen, "Two-dimensional electronic and vibrational band structure of uniaxially strained graphene from ab initio calculations", Phys. Rev. B **80**, 205 410 (2009).

[88] C. Thomsen, S. Reich, and P. Ordejón, "*Ab initio* determination of the phonon deformation potentials of graphene", Phys. Rev. B **65**, 073 403 (2002).

[89] M. Y. Han, B. Özyilmaz, Y. Zhang, and P. Kim, "Energy band-gap engineering of graphene nanoribbons", Physical Review Letters **98**(20), 206 805 (2007).

[90] X. Li, X. Wang, L. Zhang, S. Lee, and H. Dai, "Chemically derived, ultrasmooth graphene nanoribbon semiconductors", Science **319**, 1229–1231 (2008).

[91] D. Kosynkin, A. Higginbotham, A. Sinitskii1, J. Lomeda, A. Dimiev, B. Price, and J. Tour, "Longitudinal unzipping of carbon nanotubes to form graphene nanoribbons", Nature **458**(872-876) (2009).

[92] L. Jiao, L. Zhang, X. Wang, G. Diankov, and H. Dai, "Narrow graphene nanoribbons from carbon nanotubes", Nature **458**(877-880) (2009).

[93] A. Cano-Marquez, F. Rodriguez-Macias, J. Campos-Delgado, C. Espinosa-Gonzalez, F. Tristan-Lopez, *et al.*, "Ex-mwnts: graphene sheets and ribbons produced by lithium intercalation and exfoliation of carbon nanotubes", Nano Lett **9**(1527-33) (2009).

[94] L. Pisani, J. Chan, B. Montanari, and N. Harrison, "Electronic structure and magnetic properties of graphitic ribbons", Phys. Rev. B **75**, 064 418 (2007).

[95] L. Alvarez, A. Righi, T. Guillard, S. Rols, E. Anglaret, D. Laplaze, and J. Sauvajol, "Resonant raman study of the structure and electronic properties of single-wall carbon nanotubes", Chem. Phys. Lett. **316**, 186 (2000).

[96] A. Jorio, M. Pimenta, A. Souza, R. Saito, G. Dresselhaus, and M. Dresselhaus, "Characterizing carbon nanotube samples with resonance Raman scattering", New Journal of Physics **5**, 139 (2003).

[97] H. Telg, J. Maultzsch, S. Reich, F. Hennrich, and C. Thomsen, "Chirality distribution and transition energies of carbon nanotubes", Phys. Rev. Lett. **93**, 177 401 (2004).

[98] M. Fujita, K. Wakabayashi, K. Nakada, and K. Kusakabe, "Peculiar localized state at zigzag graphite edge", J. Phys. Soc. Jpn. **65**, 1920–1923 (1996).

[99] Y.-W. Son, M. L. Cohen, and S. G. Louie, "Energy gaps in graphene nanoribbons", Phys. Rev. Lett. **97**(21), 216 803 (2006).

[100] T. Wassmann, A. P. Seitsonen, A. M. Saitta, M. Lazzeri, and F. Mauri, "Structure, Stability, Edge States, and Aromaticity of Graphene Ribbons", Phys. Rev. Lett. **101**, 096 402 (2008).

[101] N. Troullier and J. L. Martins, "Efficient pseudopotentials for plane-wave calculations", Phys. Rev. B **43**, 1993 (1991).

[102] P. Ordejón, E. Artacho, and J. M. Soler, "Self-consistent order-N density-functional calculations for very large systems", Phys. Rev. B **53**, R10 441 (1996).

[103] M. Ezawa, "Peculiar width dependence of the electronic properties of carbon nanoribbons", J. Phys. Soc. Jpn. **73**, 045 432 (2006).

[104] V. Barone, O. Hod, and G. Scuseria, "Electronic structure and stability of semiconducting graphene nanoribbons", Nano Lett. **6**, 2748 (2006).

[105] K. Nakada, M. Fujita, G. Dresselhaus, and M. S. Dresselhaus, "Edge state in graphene ribbons: Nanometer size effect and edge shape dependence", Phys. Rev. B **54**(24), 17 954 (1996).

[106] O. Dubay, G. Kresse, and H. Kuzmany, "Phonon Softening in Metallic Nanotubes by a Peierls-like Mechanism", Phys. Rev. Lett. **88**(23), 235 506 (2002).

[107] S. Piscanec, M. Lazzeri, J. Robertson, A. C. Ferrari, and F. Mauri, "Optical phonons in carbon nanotubes: Kohn anomalies, peierls distortions, and dynamic effects", Phys. Rev. B **75**, 035 427 (2007).

[108] R. Saito, G. Dresselhaus, and M. S. Dresselhaus, *Physical Properties of Carbon Nanotubes* (Imperial College Press, London, 1998).

[109] J.-C. Charlier, X. Blase, and S. Roche, "Electronic and transport properties of nanotubes", Rev. Mod. Phys. **79**, 677 – 732 (2007).

[110] M. Vujičić, "Construction of the symmetry groups of polymer molecules", J. Phys. A: Math. Gen. **10**, 1271 – 1279 (1977).

[111] M. Damnjanović, I. Milošević, T. Vuković, and R. Sredanović, "Full symmetry, optical activity, and potentials of single-wall and multiwall nanotubes", Phys. Rev. B **60**(4), 2728 (1999).

[112] C. Thomsen and S. Reich, "Raman scattering in carbon nanotubes", in *Light Scattering in Solids IX*, edited by M. Cardona and R. Merlin, Topics in Applied Physics (Springer, Heidelberg, 2005).

[113] S. M. Bachilo, M. S. Strano, C. Kittrel, R. H. Hauge, R. E. Smalley, and R. B. Weisman, "Structure-assigned optical spectra of single-walled carbon nanotubes", Science **298**, 2361 (2002).

[114] H. M. Lawler, D. Areshkin, J. W. Mintmire, and C. T. White, "Radial-breathing mode frequencies for single-walled carbon nanotubes of arbitrary chirality: First-principles calculations", Phys. Rev. B **72**, 233 403 (2005).

[115] S. V. Goupalov, "Chirality dependence of the Raman cross section of carbon nanotubes", Phys. Rev. B **71**, 153 404 (2005).

[116] J. Kürti, V. Zólyomi, M. Kertesz, and G. Sun, "The geometry and the radial breathing mode of carbon nanotubes: beyond the ideal behaviour", New Journal of Physics **5**, 125 (2003).

[117] I. Milošević, E. Dobardžić, and M. Damnjanović, "Phonons in narrow carbon nanotubes", Phys. Rev. B **72**, 085 426 (2005).

[118] M. Machón, S. Reich, H. Telg, J. Maultzsch, P. Ordejón, and C. Thomsen, "Strength of radial-breathing mode in single-walled carbon nanotubes", Phys. Rev. B **71**, 035 416 (2005).

[119] M. Damnjanović, E. Dobardžić, and I. Milošević, "Chirality dependence of the radial breathing mode: a simple model", J. Phys.: Condens. Matter **16**, L505 (2004).

[120] G. Sun, J. Kürti, P. Rajczy, M. Kertesz, J. Hafner, and G. Kresse, "Performance of the vienna ab initio simulation package (vasp) in chemical applications", J. Mol. Struct. (Theochem) **624**, 37 (2003).

[121] H. J. Monkhorst and J. D. Pack, "Special points for Brillouin-zone integrations", Phys. Rev. B **13**, 5188 (1976).

[122] J. Maultzsch, R. Pomraenke, S. Reich, E. Chang, D. Prezzi, *et al.*, "Exciton binding energies in carbon nanotubes from two-photon photoluminescence", Phys. Rev. B **72**, 241 402(R) (2005).

[123] V. N. Popov and P. Lambin, "Radius and chirality dependence of the radial breathing mode and the g-band phonon modes of single-walled carbon nanotubes", Phys. Rev. B **73**, 085 407 (2006).

[124] M. Machón, S. Reich, and C. Thomsen, "Strong electron-phonon coupling of the high-energy modes of carbon nanotubes", Phys. Rev. B **74**, 205 423 (2006).

[125] J. Kürti, V. Zólyomi, M. Kertesz, G. Sun, R. H. Baughman, and H. Kuzmany, "Individualities and average behavior in the physical properties of small diameter single-walled carbon nanotubes", Carbon **42**, 971 – 978 (2004).

[126] Z. Luo, F. Papadimitrakopoulos, and S. K. Doorn, "Electron-phonon interaction and its influence on reconstruction of single-walled carbon nanotube radial breathing mode spectra", Appl. Phys. Lett. **88**(2006), 073 110 (2006).

[127] H. Telg, J. Maultzsch, S. Reich, and C. Thomsen, "Resonant-Raman intensities and transition energies of the e11 transition in carbon", Phys. Rev. B **74**, 115 415 (2006).

[128] M. Machón, *Electron-phonon coupling, vibration, and optical properties of carbon nanotubes and picotubes*, Ph.D. thesis, Berlin Institute of Technology (2005).

[129] F. Wang, G. Dukovic, L. E. Brus, and T. F. Heinz, "The optical resonances in carbon nanotubes arise from excitons", Science **308**(5723), 838 – 841 (2005).

[130] M. Machón, S. Reich, and C. Thomsen, "Electron-phonon coupling in carbon nanotubes", phys. stat. sol. (b) **243**(13), 3166 (2006).

[131] L. s. Li, J. Hu, W. Yang, and A. P. Alivisatos, "Band gap variation of size- and shape-controlled colloidal CdSe quantum rods", Nano Lett. **1**(7), 349–351 (2001).

[132] X. Peng, L. Manna, W. Yang, J. Wickham, E. Scher, A. Kadavanich, and A. Alivisatos, "Shape control of CdSe nanocrystals", Nature **404**, 59 (2000).

[133] S. Thoma, A. Sanchez, P. Provencio, B. Abrams, and J. Wilcoxon, "Synthesis, optical properties, and growth mechanism of blue-emitting cdse nanorods", J. Am. Chem. Soc. **127**, 7611 (2005).

[134] L. Manna, E. Scher, and A. Alivisatos, "Synthesis of soluble and processable rod-, arrow-, teardrop-, and tetrapod-shaped CdSe nanocrystals", J. Am. Chem. Soc. **122**, 12 700 (2000).

[135] H. Yu, J. B. Li, R. A. Loomis, P. C. Gibbons, L. W. Wang, and W. E. Buhro, "Cadmium selenide quantum wires and the transition from 3d to 2d confinement", J. Amer. Chem. Soc. **125**, 16 168 (2003).

[136] S. Tavenner-Kruger, Y. Park, M. Lonergan, U. Woggon, , and H. Wang, "Zero-phonon linewidth in CdSe/ZnS core/shell nanorods", Nano Lett. **6**, 2154 (2006).

[137] T. Sadowski and R. Ramprasad, "Stability and electronic structure of CdSe nanorods from first principles", Phys. Rev. B **76**(2007), 235 310 (2007).

[138] X. Chen, A. Nazzal, D. Goorskey, M. Xiao, Z. Peng, and X. Peng, "Polarization spectroscopy of single CdSe quantum rods", Phys. Rev. B **64**, 245 304 – 245 301 (2001).

[139] H. Lange, M. Mohr, M. Artemyev, U. Woggon, and C. Thomsen, "Direct Observation of the Radial Breathing Mode in CdSe Nanorods", Nano Lett. **8**(12), 4614 (2008).

[140] F. Widulle, S. Kramp, N. M. Pyka, A. Göbel, T. Ruf, *et al.*, "The phonon dispersion of wurtzite CdSe", Physica B **263**, 448 (1999).

[141] A. Barker, J. Merz, and A. Gossard, "Study of zone-folding effects on phonons in alternating monolayers of GaAs-AlAs", Phys. Rev. B **17**, 3181 – 3196 (1978).

[142] K. P. O'Donnell, P. J. Parbrook, F. Yang, X. Chen, D. J. Irvine, *et al.*, "The optical properties of wide bandgap binary II-VI superlattices", J. Cryst. Growth **117**(1 - 4), 497 – 500 (1992).

[143] "Landolt-Börnstein", (Springer, Berlin, Heidelberg, 1994), vol. 24b of *Series III*.

[144] C. Hartwigsen, S. Goedecker, and J. Hutter, "Relativistic separable dual-space Gaussian pseudopotentials from H to Rn", Phys. Rev. B **58**, 3641 (1998).

[145] B. Bonello and B. Fernandez, "Elastic constants of CdSe at low temperature", J. Phys. Chem. Solids **54**(2), 209 – 212 (1993).

[146] S. Ninomiya and S. Adachi, "Optical properties of cubic and hexagonal CdSe", J. Appl. Phys. **78**, 4681 (1995).

[147] N. E. Christensen, "Electronic structure of GaAs under strain", Phys. Rev. B **30**, 5753 – 5765 (1984).

[148] X. Gonze, J. M. Beuken, R. Caracas, F. Detraux, M. Fuchs, *et al.*, "First-principles computation of material properties : the ABINIT software project.", Computational Materials Science **25**, 478 – 492 (2002).

[149] X. Gonze, G.-M. Rignanese, M. Verstraete, J.-M. Beuken, Y. Pouillon, *et al.*, "A brief introduction to the ABINIT software package.", Zeit. Kristallogr. **220**, 558 – 562 (2005).

[150] W. Cochran and R. A. Cowley, "Dielectric constants and lattice vibrations", J. Phys. Chem. Solids **23**, 447 (1962).

[151] P. Giannozzi, S. de Gironcoli, P. Pavone, and S. Baroni, "Ab initio calclation of phonon dispersions in semiconductors", Phys. Rev. B **43**, 7231 (1991).

[152] T. Ruf, J. Serrano, M. Cardona, P. Pavone, M. Pabst, *et al.*, "Phonon dispersion curves in wurtzite-structure gan determined by inelastic x-ray scattering", Phys. Rev. Lett. **86**(5), 906 – 909 (2001).

[153] J. Serrano, A. H. Romero, F. J. Manjon, R. Lauck, M. Cardona, and A. Rubio, "Pressure dependence of the lattice dynamics of ZnO: An ab initio approach", Phys. Rev. B **69**, 094 306 (2004).

[154] H. Richter, Z. P. Wang, and L. Ley, "The one phonon Raman spectrum in microcrystalline silicon", Solid State Commun. **39**(5), 625 – 629 (1981).

[155] H. Lange, M. Artemyev, U. Woggon, and C. Thomsen, "Geometry dependence of the phonon modes in CdSe nanorods", Nanotechnology **20**, 045 705 (2009).

[156] C. Q. Sun, "Size dependence of nanostructures: Impact of bond order deficiency", Prog. Solid State Chem. **35**(1), 1 – 159 (2007).

[157] H. W. Verleur and A. S. Barker Jr., "Phonons in mixed crystals of $CdSe_yS_{1-y}$", Phys. Rev. **155**, 750 (1967).

[158] D. Fernández-Torre, R. Escribano, T. Archer, J. M. Pruneda, and E. Artacho, "First-principles infrared spectrum of nitric acid and nitric acid monohydrate crystals", J. Phys. Chem. A **108**(123), 10 535 – 10 541 (2004).

[159] D. M. Aruguete, M. A. Marcus, L. S. Li, A. Williamson, S. Fakra, *et al.*, "Surface structure of CdSe nanorods revealed by combined x-ray absorption fine", J. Phys. Chem. C **111**, 75 – 79 (2007).

[160] M. Mohr and C. Thomsen, "Effects of a ZnS-shell on the structural and electronic properties of CdSe-nanorods", physica status solidi (b) **245**, 2111 (2008).

[161] M. Yamamoto, C. T. Chan, K. M. Ho, M. Kurahashi, and S. Naito, "First-principles calculation of the longitudinal phonon in the surface-normal direction of a zirconium(0001) slab: Localization mode at the subsurface", Phys. Rev. B **53**, 13 772 (1996).

[162] R. Fuchs and K. L. Kliewer, "Optical modes of vibration in an ionic crystal slab", Phys. Rev. **140**(6), A2076 – A2088 (1965).

[163] L. Yang, *First-principles Calculations on the Electronic, vibrational, and optical properties of semiconductor nanowires*, Ph.D. thesis, Georgia Institute of Technology (2006).

[164] M. Born and K. Huang, *Dynamical Theory of Crystal Lattices* (Oxford University Press, 1954).

[165] H. Lange, M. Machón, M. Artemyev, U. Woggon, and C. Thomsen, "Effect of ZnS shell on the Raman spectra from CdSe nanorods", phys. stat. sol. (RRL) **1**, 274 (2007).

[166] H. Lange (priv. comm. (2008)).

[167] J. Maultzsch, H. Telg, S. Reich, and C. Thomsen, "Radial breathing mode of single-walled carbon nanotubes: Optical transition energies and chiral-index assignment", Phys. Rev. B **72**, 205 438 (2005).

[168] M. Hu, X. Wang, G. V. Hartland, P. Mulvaney, J. P. Juste, and J. E. Sader, "Vibrational response of nanorods to ultrafast laser induced heating: Theoretical and experimental analysis", J. Am. Chem. Soc. **125**, 14 925 (2003).

[169] T. Thonhauser and G. D. Mahan, "Predicted Raman spectra of si[111] nanowires", Phys. Rev. B **71**, 081 307(R) (2005).

[170] C. F. Cline, H. L. Dunegan, and G. W. Henderson, "Elastic constants of hexagonal BeO, ZnS, and CdSe", J. Appl. Phys. **38**, 1944 (1967).

[171] A. Panda, S. Acharya, and A. Efrima, "Ultranarrow ZnSe nanorods and nanowires: Structure, spectroscopy, and one-dimensional properties", Adv. Mater. **17**, 2471 (2005).

[172] N. Pradhan and S. Efrima, "Supererystals of uniform nanorods and nanowires, and the nanorod-to-nanowire oriented transition", J. Phys. Chem. B **108**, 11 964 (2004).

[173] D. Gerion, F. Pinaud, S. Williams, W. Parak, D. Zanchet, S. Weiss, and A. Alivisatos, "Synthesis and properties of biocompatible water-soluble silica-coated CdSe/ZnS semiconductor quantum dots", J. Phys. Chem. B **105**, 8861 (2001).

[174] A. Aharoni, D. Oron, U. Banin, E. Rabani, and J. Jortner, "Long-range electronic-to-vibrational energy transfer from nanocrystals to their surrounding matrix environment", Phys. Rev. Lett. **100**, 057 404 (2008).

[175] G. Chilla, T. Kipp, T. Menke, D. Heitmann, M. Nikolic, *et al.*, "Direct observation of confined acoustic phonons in the photoluminescence spectra of a single CdSe-CdS-ZnS core-shell-shell nanocrystal", Phys. Rev. Lett. **100**, 057 403 (2008).

[176] H. Lange, M. Artemyev, U. Woggon, T. Niermann, and C. Thomsen, "Experimental investigation of exciton-LO-phonon couplings in CdSe/ZnS core/shell nanorods", Phys. Rev. B **77**, 193 393 (2008).

[177] L. Li, J. Walda, L. Manna, and A. Alivisatos, "Semiconductor nanorod liquid crystals", Nano Lett. **3**, 961 (2002).

[178] W. Huynh, J. Dittmer, and A. Alivisatos, "Hybrid nanorod-polymer solar cells", Science **259**, 2425 (2002).

[179] E. Chang and G. R. Barsch, "Pressure dependence of single crystal elastic constants and anharmonic properties of wurtzite", J. Phys. Chem. Solids **34**(9), 1543 – 1563 (1973).

[180] Y.-J. Lee, T.-G. Kim, and Y.-M. Sung, "Lattice distortion and luminescence of CdSe/ZnSe nanocrystals", Nanotechnology **17**, 3539 (2006).

[181] S.-P. Huang, W.-D. Cheng, D.-S. Wu, J.-M. Hu, J. Shen, *et al.*, "Density functional theoretical determinations of electronic and optical properties of nanowires and bulks for CdS and CdSe", Appl. Phys. Lett. **90**, 031 904 (2007).

[182] H. Mattoussi, L. H. Radzilowski, B. O. Dabbousi, E. L. Thomas, M. G. Bawendi, and M. F. Rubner, "Electroluminescence from heterostructures of poly(phenylene vinylene) and inorganic CdSe nanocrystals", J. Appl. Phys. **83**(12), 7965 – 7974 (1998).

[183] B. Tian, X. Zheng, T. J. Kempa, Y. Fang, N. Yu, *et al.*, "Coaxial silicon nanowires as solar cells and nanoelectronic power sources", Nature **449**, 885 – 889 (2007).

[184] R. Gillen, M. Mohr, and J. Maultzsch, "Symmetry properties of vibrational modes in graphene nanoribbons", Phys. Rev. B **81**, 205 426 (2010).

[185] F. D. Murnaghan, "The compresibility of media under extreme pressures", Proc. Natl. Acad. Sci. USA **30**, 244 (1944).

Acknowledgments

This work would not have been possible without the help of many people. I would like to thank specially...

Christian Thomsen for being the supervisor of my thesis, for giving me the great opportunity to work in his nice group, for his interest in and support of my work, for his encouragement, and for the granted freedom in doing research.

Milan Damnjanović for reviewing this thesis, for travelling the long way to the defence by car, for the nice private lessons about group theory and POLSym, and for the kind invitations to his group.

Michael Lehmann for being the chairman of my thesis comitee.

Janina Maultzsch for the discussions, answering my questions even in her busiest hour, for being an excellent proof reader, and for the infinite supply of chocolate and cookies.

Konstantinos Papagelis for waking my interest into uniaxial strain in graphene. His large interest in physics and discussions about - are very inspiring.

Mariá Machón for teaching me SIESTA during my undergraduate studies. Thank you for proof-reading my first papers, which was not an easy task, and, last but not least, for convincing me of using the great editor vi.

Harald Scheel for the help with laboratories, the about computer-clusters, the attitude that everything is possible and then can be improved...

Michael Krisch and Alexei Bossak (ESRF Grenoble), without their help we would not not have been able to do the inelastic x-ray experiments on graphite

Holger Lange for the discussions about CdSe nanorods and proofing experimentally the existence of the RBM in CdSe nanorods. Also for proof-reading parts of this work, and sharing the same hobbies.

Roland Gillen for being my *Diplomand*. It was an impressive experience seeing a steep understanding curve after a short period of introduction. Good luck in Cambridge, UK.

Marianne Heinold(†) and Mandy Neumann for their help in surviving the bureaucracy a university implicates.

Mikel Mayer, Bernd Schöler and Heiner Perls for their instantaneous help and the relaxing talks about non-physics topics.

All the colleagues in the groups of Thomsen, Maultzsch, and Hoffmann for the great time, discussions about physics and all the rest. For being helpful at every time of the day, literally.

Dorith, Michael and my parents

Eidesstattliche Versicherung

Hiermit erkläre ich an Eides statt, dass ich die vorliegende Dissertation "*Electronic and vibrational properties of carbon and CdSe nanostructures*" selbständig verfasst sowie die benutzten Quellen und Hilfsmittel vollständig angegeben habe. Teile der Dissertation wurden schon veröffentlicht.

Berlin, October 20, 2010

Marcel Mohr
Gubener Strasse 29
10243 Berlin